



Norwegian University of
Science and Technology

Preliminary Benchmarking of the HYB (Hybrid Metal Extrusion & Bonding) Process for Butt Welding of AA6082-T6 Plates Against FSW and GMAW

Lise Sandnes

Master of Science in Mechanical Engineering

Submission date: July 2017

Supervisor: Torgeir Welo, MTP

Norwegian University of Science and Technology
Department of Mechanical and Industrial Engineering

Abstract

The patented Hybrid Metal Extrusion & Bonding (HYB) process enables joining of aluminium components with filler metal addition in the solid state. The mechanical properties of a 4 mm AA6082-T6 butt joint made using this technique have been determined. The experimental programme included transverse hardness testing, tensile testing and Charpy V-notch testing, sampling different regions of the weldment. In addition, both optical microstructure analysis of the weld and scanning electron microscope examination of selected fracture surfaces have been carried out. The resulting mechanical integrity of the joint is then compared with that typically achieved using conventional GMAW and FSW.

The preliminary benchmarking of the HYB process shows that the mechanical properties of the joint, i.e. strength, ductility, impact toughness and load-bearing capacity, are slightly better than the values reported for a comparable GMA weld. Still, they do not fully match those of a sound FS weld. Therefore, there is a potential for further optimization of the HYB process in order to bring the method to the forefront of aluminium welding technology. This work is now in progress.

Sammendrag

Hybrid Metal Extrusion & Bonding (HYB) er en patentert sveiseprosess for aluminium som, ved bruk av et tilsettmateriale og plastisk deformasjon, produserer sveiseforbindelser i fast fase. I denne rapporten har de mekaniske egenskapene til en HYB buttsveis av typen 4 mm AA6082-T6 blitt dokumentert. De eksperimentelle forsøkene har inkludert tverrgående hardhetstesting, strekkprøving og Charpy V-skår testing, hvor prøvestykkene er blitt tatt fra ulike områder i sammenføyningen. I tillegg, så er sveisens mikrostruktur blitt undersøkt i optisk mikroskop mens utvalgte bruddflater er undersøkt i skanning elektronmikroskop. De mekaniske egenskapene til HYB sveisen har deretter blitt sammenlignet med tilsvarende verdier rapportert for GMAW og FSW.

Sammenligning viser at de mekaniske egenskapene til HYB sveisen som styrke, duktilitet, slagseighet og lastbærende kapasitet er noe bedre enn det som normalt oppnås ved GMA-sveising. Samtidig ligger disse verdiene noe lavere enn de som er rapportert for FS-sveising. HYB prosessen må dermed igjennom en ytterligere videreutvikling og optimalisering for å nå målet om å bli fremtidens sveiseprosess for aluminium. Dette arbeidet har nå startet.

Preface and Acknowledgements

The present report is written during the spring semester 2017 in partial fulfilment of the requirement for the MSc degree at the Department of Mechanical and Industrial Engineering (MTP) at the Norwegian University of Science and Technology (NTNU) in Trondheim, Norway. The project work is linked up with the NTNU Aluminium Product Innovation Center (NAPIC) and the company HyBond AS. Supervisor for this project has been Professor Torgeir Welo.

In particular, I would like to thank Professor Øystein Grong for his guidance and all information provided regarding the HYB technology. This has been of great value for understanding the technology and the writing of the report. In addition, I would like to thank all the other individuals who have assisted me during the course of the work.

Trondheim, Sunday July 16, 2017

Lise Sandnes

Table of Contents

Abstract	i
Sammendrag	iii
Preface and Acknowledgements	v
List of Figures	x
List of Tables.....	xiv
List of Abbreviations.....	xv
1 Introduction	1
1.1 Background	1
1.2 Objectives.....	2
1.3 Scope	2
2 Theory	3
2.1 Al-Mg-Si Alloys.....	3
2.1.1 Main alloying elements	3
2.1.2 Process chain	4
2.1.3 Precipitation Hardening.....	5
2.1.4 Effect of dissolved atoms and precipitates	7
2.1.5 Grain structure and texture	8
2.1.6 Fracture mechanisms	9
2.2 Fusion welding of Al-Mg-Si alloys.....	9
2.2.1 Defects related to fusion welding	9
2.2.2 Microstructure and strength	11
2.2.3 Mechanical properties of GMAW AA6082-T6 joints	13
2.3 Solid state joining.....	16
2.3.1 Metallic bonding	16
2.3.2 Solid state processes	16
2.4 Friction Stir Welding (FSW).....	18
2.4.1 The Process	18
2.4.2 Microstructure and strength	19
2.4.3 Mechanical properties of friction stir welded AA6082-T6 joints	21

2.5	Hybrid Metal Extrusion & Bonding (HYB).....	23
2.5.1	Principles behind the technology	23
2.5.2	The Process	24
2.5.3	Bonding	26
2.6	Load-bearing capacity of welded components.....	27
3	Experimental.....	29
3.1	Materials.....	29
3.1.1	Base material	29
3.1.2	Filler material	29
3.2	Joining conditions	30
3.3	Sample preparation and metallographic examination	31
3.3.1	Sample sectioning	31
3.3.2	Sample preparation.....	31
3.3.3	Optical microscopy	32
3.3.4	Hardness testing	33
3.4	Tensile testing	33
3.5	Impact testing	35
3.6	Fracture surface analysis in the Scanning Electron Microscope (SEM).....	36
4	Results	37
4.1	Microstructure examination	37
4.1.1	Base material	37
4.1.2	HYB joint	38
4.2	Hardness profiles.....	39
4.3	Tensile test results	42
4.4	Fractography of tensile specimens	46
4.5	Charpy V-notch test results	48
4.6	Fractography of Charpy V-notch specimens.....	49
5	Discussion.....	53
5.1	Introductory remarks	53
5.2	Effect of base material chemical composition and processing conditions.....	53
5.3	Summary of assembled flow curves.....	54

5.4	Comparison of mechanical properties of the different GMA, FS and HYB weldments.....	54
5.4.1	Mechanical strength	54
5.4.2	Ductility.....	57
5.4.3	Impact toughness.....	59
5.4.4	Overall mechanical performance	60
5.5	Comparison of hardness profiles.....	62
5.6	Relationship between hardness profile and yield strength.....	62
5.7	Load-bearing capacity of the GMA, FS and HYB weldments	66
5.7.1	General	66
5.7.2	Loading perpendicular to the joint	66
5.7.3	Loading parallel to the joint	66
5.7.4	Summary of calculated joint loading capacities.....	68
6	Conclusions	70
7	References	72
	Appendix	76

List of Figures

Figure 2.1	Equilibrium binary solid solubility of Mg and Si in aluminium as a function of temperature	3
Figure 2.2	Variation of main alloying elements in some commercial Al-Mg-Si alloys.	4
Figure 2.3	Illustration of the main process steps in production of Al-Mg-Si extrusions.	4
Figure 2.4	Quasi-binary section through the aluminium-rich corner of the ternary Al-Mg-Si phase diagram.	6
Figure 2.5	Strength evolution during artificial and natural aging of Al-Mg-Si alloys.	7
Figure 2.6	Contribution from dissolved alloying elements in solid solution (A) and precipitation hardening (B, C).	8
Figure 2.7	Recrystallized and non-recrystallized grain structures.	9
Figure 2.8	Illustration of some common defects caused by fusion welding of aluminium.	10
Figure 2.9	Solidification crack formation in the fusion zone in GMA AA6005-T4 weld.	10
Figure 2.10	Hydrogen solubility in pure aluminium as a function of temperature.	11
Figure 2.11	Sketch of the different zones which may form in a welded component.	11
Figure 2.12	Optical micrograph showing the fusion zone of an aluminium alloy welded using a AA5183 filler wire.	12
Figure 2.13	Schematic diagram showing the microstructure evolution during thermal processing of Al-Mg-Si alloys involving heat treatment and welding.	12
Figure 2.14	Relation between peak temperature and hardness distribution in an AA6082-T6 weld.	13
Figure 2.15	Transverse hardness profile of the AA6082-T6 GMA joint being examined by Breivik [38].	14
Figure 2.16	Dimensions of tensile specimens used by Breivik [38].	14
Figure 2.17	Measured stress-strain curves for selected tensile specimens, sampling different zones in the AA6082-T6 GMA joint being examined by Breivik [38].	15
Figure 2.18	Dimensions of Charpy V-notch specimens used by Breivik [38].	15
Figure 2.19	The absorbed energy of selected GMAW Charpy V-notch specimens sampling the base material and HAZ. Data from Breivik [38].	16
Figure 2.20	Illustration of metallic bonding.	16
Figure 2.21	Rotary friction welding.	17
Figure 2.22	Schematic illustration of steps in CPW.	18
Figure 2.23	Illustration of FSW process used for butt joining of plates.	19

Figure 2.24	Classifications of various regions in a friction stir weld of the AA6061-T6 type.	20
Figure 2.25	Schematic illustration of the typical hardness distribution of a FS joint.	20
Figure 2.26	Transverse hardness profile of the AA6082-T6 FS joint being examined by Breivik [38].	21
Figure 2.27	Measured stress-strain curves for selected tensile specimens, sampling different regions within the FS AA6082-T6 joint being examined by Breivik [38].	22
Figure 2.28	Absorbed energy of selected FSW Charpy V-notch specimens, sampling the base material and the HAZ/TMAZ. Data from Breivik [38].	22
Figure 2.29	Schematic illustration of different types of extrusion.	23
Figure 2.30	Illustration of moving and stationary parts in continuous extrusion.	24
Figure 2.31	Solid Works drawing of the conical pin used for HYB butt joining of plates.	24
Figure 2.32	Illustration of main components in the HYB PinPoint Extruder head	25
Figure 2.33	Illustration of the rotating pin and its location in the groove during HYB butt welding of plates.	25
Figure 2.34	Illustration of material flow pattern during HYB butt welding of plates	26
Figure 2.35	The two idealized loading conditions being examined. (a) Loading perpendicular to weld. (b) Loading parallel to weld.	27
Figure 2.36	Sketch showing how the equivalent half width of the reduced strength zone y_{red}^{eq} of minimum strength σ_{min} is related to an assumed yield strength profile across the weld.	28
Figure 3.1	Schematic drawing of the plate material used in HYB joining trials. Note that the welding direction is parallel with the plate rolling direction.	30
Figure 3.2	Photograph of the butt welded plates received from HyBond AS. Shown is also the welding/rolling direction and the retreating/advancing side.	31
Figure 3.3	Schematic illustration of sample sectioning and numbering of specimens.	31
Figure 3.4	Photograph of the specimen used for micrographic examination and hardness testing.	32
Figure 3.5	Schematic illustration of the different sections that have been examined in the optical microscope.	32
Figure 3.6	Photograph of sample used for hardness testing, indicating the location of the different series of measurements.	33
Figure 3.7	Schematic illustration of the location of the different tensile specimens.	34
Figure 3.8	Dimensions of the flush-machined subsize specimen used for tensile testing. All values are given in millimetres.	34
Figure 3.9	Schematic illustration of Charpy V-notch specimens sampling different zones within the HYB joint.	35
Figure 3.10	Dimensions of subsize Charpy V-notch specimens used for impact testing. All values are given in millimetres.	36

Figure 4.1	Optical micrographs showing the microstructure of the rolled AA6082-T6 base material at low magnification (5x).	37
Figure 4.2	Optical micrograph of the AA6082-T6 base metal microstructure parallel to the plate rolling direction at high magnification (20x).....	37
Figure 4.3	Optical micrograph showing the macrostructure of the HYB joint.....	38
Figure 4.4	Optical micrograph showing changes in microstructure across the bond line between the base material and the filler material in the HYB joint (10x).....	38
Figure 4.5	Photograph of the hardness indentations taken along the specimen mid-sections in the third test series.	39
Figure 4.6	Measured hardness profile along the horizontal mid-section of the HYB joint.....	39
Figure 4.7	Measured hardness profile along the vertical mid-section of the HYB joint.	40
Figure 4.8	Photograph showing the hardness indentations from the second test series.	40
Figure 4.9	Displaced horizontal hardness profiles for the HYB joint.	41
Figure 4.10	Displaced vertical hardness profiles for the HYB joint.....	41
Figure 4.11	Examples of macro-images of tested tensile specimens showing the fracture point in each of the zones.....	42
Figure 4.12	Example of measured stress-strain curves during tensile testing sampling different zones within the HYB joint.	42
Figure 4.13	Measured stress at offset yield for selected tensile specimens sampling different zones within the HYB joint.	43
Figure 4.14	Measured tensile strength for selected tensile test specimens sampling different zones within the HYB joint.	44
Figure 4.15	Measured strain at fracture for selected tensile specimens sampling different zones within the HYB joint.	44
Figure 4.16	Sketch showing the initial cross-sectional area A_0 prior testing and the reduced cross-sectional area A_f at the point of fracture.	45
Figure 4.17	Calculated RA-values for selected tensile specimens sampling different zones within the HYB joint.	45
Figure 4.18	SEM micrographs showing the fracture surface appearance of the base material.	46
Figure 4.19	SEM micrographs showing the fracture surface appearance of the extrusion zone.....	47
Figure 4.20	SEM micrographs showing the HAZ fracture surface appearance.	47
Figure 4.21	Macro-images of broken Charpy V-notch specimens sampling different zones within the HYB joint.	48
Figure 4.22	Measured energy absorption for selected Charpy V-notch specimens sampling different zones within the HYB joint.....	49

Figure 4.23	SEM micrographs of the fracture surface appearance of broken Charpy V-notch specimens sampling different zones within the HYB joint at low magnification.	50
Figure 4.24	SEM micrographs at high magnification, showing the fracture surface appearance close to the Charpy V-notch at different locations within the HYB joint.	51
Figure 4.25	SEM micrographs at high magnification, showing the fracture surface appearance in the center the Charpy-V notch specimens at different locations within the HYB joint.	52
Figure 5.1	Difference in the main alloying elements (i.e. Mg and Si) between the two base materials used for GMA, FS and HYB joining.	53
Figure 5.2	Comparison of measured stress-strain curves for selected GMAW, FSW and HYB tensile specimens.	54
Figure 5.3	Comparison of the average offset yield strengths for the GMAW, FSW and HYB tensile specimens.	55
Figure 5.4	Comparison of the average tensile strengths for the GMAW, FSW and HYB tensile specimens.	56
Figure 5.5	Calculated strain-hardening potential for different zones in the GMA, FS and HYB weldments.	56
Figure 5.6	Comparison of the percentage reduction in the fracture strain relative to the base material for the GMAW, FSW and HYB tensile specimens.	57
Figure 5.7	Comparison of the average reduction in area for the GMAW, FSW and HYB tensile specimens.	58
Figure 5.8	Calculated change in the cross-sectional area reduction relative the base material for the same set of tensile specimens included in Figure 5.7.	58
Figure 5.9	Definition of the initial cross-sectional area of a Charpy V-notch specimen used to calculate the normalized energy absorption.	59
Figure 5.10	Comparison of the average energy absorption per unit area for the GMAW, FSW and HYB Charpy V-notch specimens, sampling different zones in the weldments.	59
Figure 5.11	Calculated change in energy absorption relative to the base material for the GMAW, FSW and HYB Charpy V-notch specimens included in Figure 5.10.	60
Figure 5.12	Comparison of measured hardness profiles for the GMA, FS and HYB joints.	62
Figure 5.13	Macro-image of a HYB tensile specimen showing the location of the fracture on the advancing side relative to the joint center.	63
Figure 5.14	Calculated yield strength profiles based on Equation (2.3) and the measured GMAW, FSW and HYB hardness profiles.	64
Figure 5.15	Determination of the equivalent half width of the reduced strength zone y_{red}^{eq} , of minimum strength σ_{min} based on the calculated yield stress profiles for the GMA, FS and HYB joints.	67

List of Tables

Table 3.1 Chemical composition of AA6082 used as base metal. 29

Table 3.2 Chemical composition of the AA6082 DC cast billets used in the HYB filler wire manufacturing. 29

Table 3.3 Homogenization conditions pertaining to the AA6082 DC cast billets being used in the HYB filler wire manufacturing. 30

Table 3.4 Summary of welding parameters used in the HYB joining trials of the 4 mm AA6082-T6 plates. 30

Table 3.5 Total number of tensile test specimens tested. 35

Table 3.6 Total number of Charpy V-notch specimens tested. 36

Table 5.1 Summary of the reduction/increase in mechanical properties of the different weld samples included in the analysis. 61

Table 5.2 Summary of key yield strength data for the GMA, FS and HYB joints..... 65

Table 5.3 Summary of calculated and measured strength reductions based on hardness and tensile testing, respectively. 65

Table 5.4 Summary of input data used to calculate the relative increase in the cross-sectional area $\Delta A/A$ from Equation (5.2). 68

Table 5.5 Summary of all results from the load-bearing capacity calculations..... 68

List of Abbreviations

AS	Advancing Side
BL	Bond Line
BM	Base Material or Metal
β	Equilibrium phase (Mg_2Si)
β'	Hardening precipitate in Al-Mg-Si alloys (semi-coherent rods)
β''	Hardening precipitate in Al-Mg-Si alloys (coherent needles)
CPW	Cold Pressure Welding
EZ	Extrusion Zone
FM	Filler Material or Metal
FSW	Friction Stir Welding
FZ	Fusion Zone
GMAW	Gas Metal Arc Welding
HAZ	Heat Affected Zone
HYB	Hybrid Metal Extrusion & Bonding
HV	Hardness Vickers
HV ₁	Hardness Vickers – 1 kg load
MAZ	Mechanically Affected Zone
RA	Reduction in Area
RS	Retreating Side
SEM	Scanning Electron Microscope
SSSS	Super Saturated Solid Solution

SZ	Stir Zone
T4	Naturally aged condition
T6	Peak-aged condition
TMAZ	Thermomechanically Affected Zone

1 Introduction

1.1 Background

Globally, there is an increased focus on reducing the humanly created CO₂-emission, which mainly comes from burning of fossil fuels related to transportation and industrial activity [1]. Traditionally, steel has been the material of choice for transport applications. However, an increased use of lightweight materials, such as aluminium, may contribute to reduce the vehicle mass and thereby reducing the fuel consumption and CO₂-emission [2, 3]. Despite lower tensile properties and higher costs compared to steel, aluminium alloys are to an increasing extent used as structural components due to their high specific strength (strength-to-density ratio) and good resistance against general corrosion [4]. Today, there is a diversity of aluminium alloys available for commercial use, where their mechanical and physical properties depend on the additional alloying elements, the extent of mechanical work hardening and/or the applied heat treatment schedule [5]. For instance, the Al-Mg-Si alloys (6xxx series) exhibit good formability, machinability as well as the ability to be fusion welded. They are commonly used in the peak-aged condition as extrusions or rolled plates, and are suitable for a wide range of structural applications as well as components in lightweight vehicles [2, 5].

Many aluminium products involve the use of welding as a fabrication method, such as autobody sheets and space frames for automobiles, architectural panels and components for marine applications [5, 6]. The most common welding technique for aluminium alloys, is gas-metal arc welding (GMAW), which offers advantages of high quality welds, high welding speeds and the possibility to be robotized [7, 8]. However, several problems are associated with fusion welding of the peak-aged Al-Mg-Si alloys. In the fusion zone, the microstructure goes back to the “as-cast state”, and the excessive heat gives rise to the formation of a soft heat affected zone (HAZ) close to the joint [9]. In addition, problems related to oxidation, hydrogen pick-up in the weld region, solidification cracking and hot cracking reduces the mechanical properties of the welded components [4, 10].

For joining of aluminium alloys, solid state processes offer several advantages over traditional fusion welding. Since there is no melting involved, the fusion zone with its “as-cast” microstructure is eliminated and, as in friction stir welding (FSW), replaced by a thermomechanically affected zone (TMAZ) with superior ductility and toughness [11, 12]. In addition, the joints are usually free from defects like porosity, slag inclusions and hot cracks

[13, 14]. However, due to the frictional heat generated during the FSW process, HAZ softening is still present and of major concern [15]. Avoiding problems related to the HAZ requires joining processes operating below the softening temperature of the material [9]. The novel Hybrid Metal Extrusion and Bonding (HYB) process enables joining of aluminium at lower temperatures and produces sound joints with improved strength, less cracking and corrosion problems. The technology has evolved through almost 20 years, and several concepts have been tried out. This has contributed to elimination of poor design solution and resulted in the today's solution, the HYB PinPoint extruder. By the use of a filler material and plastic deformation the process produces solid state joints. It is believed that the HYB process has the potential to compete with conventional joining processes such as FSW and GMAW in the future when it has been further optimized.

1.2 Objectives

At present, there is very little published information about the HYB joint properties. The aim of the present report is to determine the mechanical properties of AA6082-T6 subsequent to HYB joining and evaluate the mechanical integrity compared to GMAW and FSW.

1.3 Scope

Thus, a more extensive analysis, covering both hardness, tensile and Charpy V-notch testing, will be carried out. The tensile and Charpy V-notch tests are carried out at different locations relative to the weld center-line. In addition, specific microstructural features of the joint are studied by optical microscopy. Furthermore, the fracture surfaces of the tested tensile and Charpy V-notch specimens are analysed in a scanning electron microscope (SEM). All mechanical testing is carried out at room temperature. A more detailed task description for the thesis work is given in the beginning of the Appendix.

2 Theory

2.1 Al-Mg-Si Alloys

2.1.1 Main alloying elements

The unique physical and mechanical properties of the Al-Mg-Si alloys make them attractive for a wide range of structural applications, where a high specific strength (strength-to-density ratio) is required [9]. The strength of Al-Mg-Si alloys is due to the main alloying elements, magnesium (Mg) and silicon (Si). These alloying elements have significant solid solubility in aluminium, which increases with increasing temperatures, as illustrated in Figure 2.1 [5]. The Al-Mg-Si alloys make use of this solubility to form various hardening phases of Mg and Si during heat treatment to achieve the desired base metal mechanical properties [16].

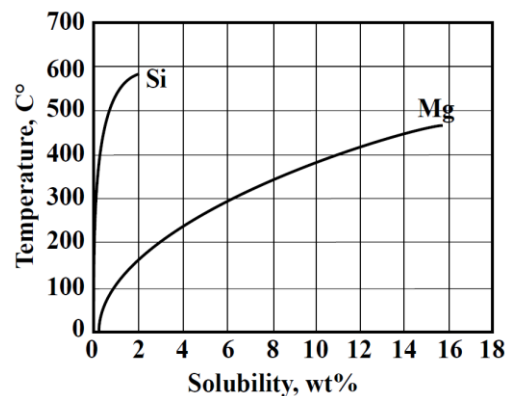


Figure 2.1 Equilibrium binary solid solubility of Mg and Si in aluminium as a function of temperature. Copied from [5].

The ratio between the amount of Mg and Si for some common alloys is shown in Figure 2.2, where the black line indicates the stoichiometric ratio needed to form Mg_2Si . Above this line there is an excess of silicon over that required to form Mg_2Si , which contributes significantly to solid solution hardening [17]. The high solubility of the main alloying elements in Al-Mg-Si alloys is fully utilized during solution heat treatment, which is incorporated in the extrusion process [18]. The age hardened aluminium alloys, such as the Al-Mg-Si alloys, obtain their high strength during subsequent artificial ageing [19].

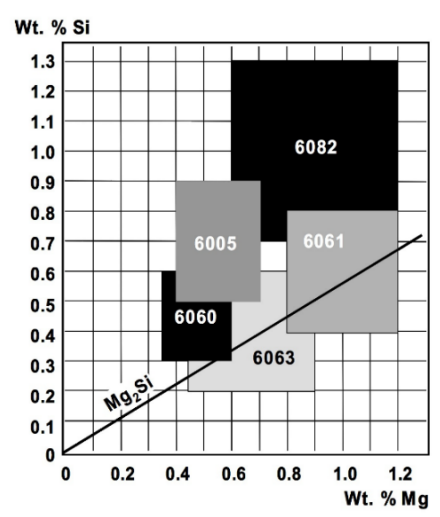


Figure 2.2 Variation of main alloying elements in some commercial Al-Mg-Si alloys. Copied from [20].

2.1.2 Process chain

Al-Mg-Si alloys are commonly used in extrusions, and their strength depends on the chemical composition as well as the processing conditions through the whole process chain. All the steps in the process chain, which are illustrated in Figure 2.3, have an influence on the microstructure of the alloy (such as constituent particles, dispersoids, amount of elements in solid solution, age hardening precipitates, grain size and texture) and thus the resulting mechanical properties [21, 22].

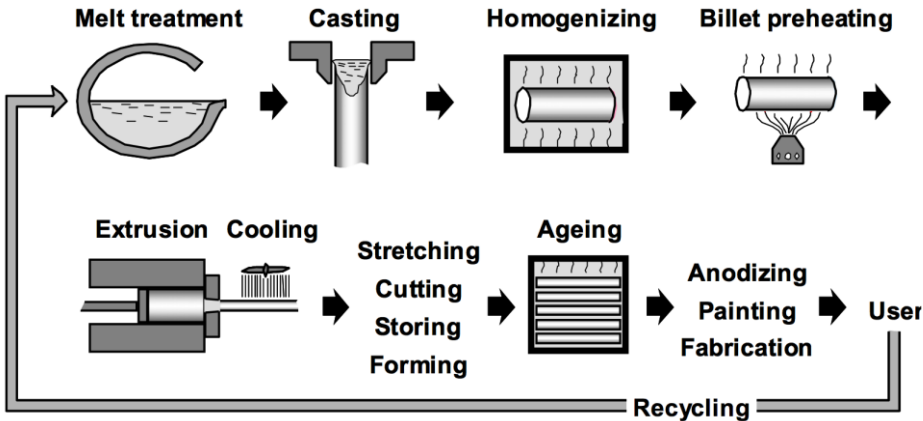


Figure 2.3 Illustration of the main process steps in production of Al-Mg-Si extrusions. Copied from [22].

The first step in the process chain is melt treatment. Here Mg and Si are added in the melt together with other desirable alloying elements that control the properties of the alloy. The main alloying elements are partly dissolved in solid solution in the primary α -Al matrix, and partly present in the form of intermetallic phases [17, 23]. The ratio between the main alloying

elements strongly influence the amount of Mg_2Si formed during solidification (as illustrated earlier in Figure 2.2).

In all commercial alloys iron (Fe) is present as an impurity, and forms a variety of intermetallic phases during solidification, such as Al-Fe and Al-Fe-Si. At a later stage in the solidification process, any Si that is not incorporated in the α -Al matrix or the Al-Fe-Si intermetallic phase, will combine with Mg and form Mg_2Si [17, 23].

After casting, the microstructure of the billet is quite heterogeneous with a cored dendritic structure and relative low ductility [16]. Therefore, the as-cast billet requires homogenization treatment to make the material suitable for hot working. During the homogenization treatment, both transformation of unfavourable intermetallics as well as dissolution of β - Mg_2Si particles occurs that will improve the ductility of the alloy [24]. Therefore, the homogenization treatment gives a maximum precipitation hardening potential for the extruded product [25].

The billet is then loaded into the extrusion chamber and extruded through a die, before it is rapidly cooled to room temperature [21]. All the steps mentioned will influence the nature of the intermetallic particle population, where both type, size, morphology and distribution of the intermetallic phases are important in determining the subsequent mechanical properties of the alloy [17, 23]. The final step in the production chain involves aging of the extrusion at moderate temperatures for several hours to precipitate coherent and semi-coherent strengthening Mg-Si phases [21]. For the Al-Mg-Si alloys, the resulting mechanical properties at room temperature are directly linked to the number density and size distribution of the hardening precipitates that form during artificial aging [26].

2.1.3 Precipitation Hardening

Precipitation hardening is commonly employed to Al-Mg-Si alloys to improve their mechanical properties, either as part of the extrusion process or as a separate process. Precipitation hardening occurs as a result of solution treatment of the alloy, where most of the Mg and Si are in solid solution at elevated temperature but precipitates upon quenching and aging at a lower temperature [27]. The precipitation process is both time and temperature dependent and, as indicated in Figure 2.4, consists of the following steps [9, 16]:

1. *Solution heat treatment.* The alloy is heated to a prescribed elevated temperature (T_1) and held there for a certain period of time.
2. *Quenching.* The alloy is rapidly cooled down to room temperature (RT) to retain the microstructure developed following solution heat treatment.

3. *Artificial aging.* The alloy is held at a lower temperature (T_2) for a certain period of time.

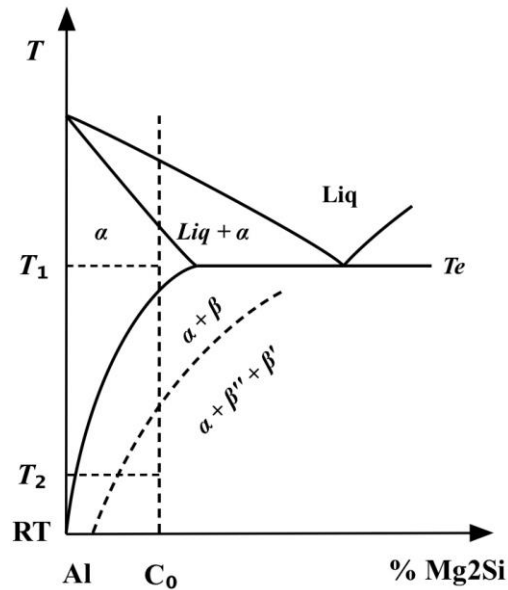
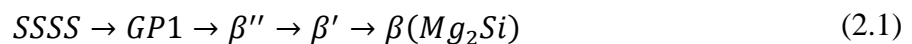


Figure 2.4 Quasi-binary section through the aluminium-rich corner of the ternary Al-Mg-Si phase diagram. Copied from [9].

The purpose of the solution heat treatment is to ensure that most of the Mg and Si are in solid solution in the aluminium matrix. The temperature must therefore be above the solvus boundary of the equilibrium Mg_2Si phase, as shown in Figure 2.4. Then the alloy is rapidly cooled (quenched), to preserve the solid solution formed at T_1 [16]. The alloying elements are now present in solid solution or in the form of small clusters distributed through the matrix, and is said to be in a supersaturated solid solution (SSSS). For a balanced alloy, containing Mg and Si in a stoichiometric ratio ($Mg/Si = 1.73$), the precipitation sequence may be written as followed [28]:



The fine, needle-shaped β'' -precipitates are the dominant hardening phase, and during aging a high number density of these particles is formed uniformly in the matrix [26]. The maximal hardness is obtained when the microstructure consists of both β'' -particles and coarser, rod-shaped β' -particles [29].

During aging the properties constantly evolve with aging time and aging temperature. The strength and hardness increase with time until the peak value is reached, which is referred to as the peak-aged (T6) condition. Beyond this value, both strength and hardness decrease with increased aging time, as illustrated in Figure 2.5. This decrease in strength and hardness are

referred to as overaging [30]. Note that the solution heat treated Al-Mg-Si alloys have also the ability to naturally age by storage at room temperature. This is illustrated by the dotted line in the below figure, and is referred to as T4 condition [9].

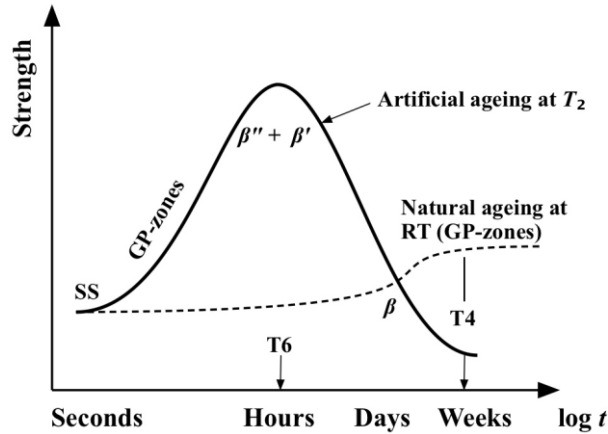


Figure 2.5 Strength evolution during artificial and natural aging of Al-Mg-Si alloys. Copied from [9].

After precipitation hardening, the microstructure consists of grains with a high density of fine hardening precipitates formed homogeneously in the material during artificial aging [19]. In the peak-aged condition the fine precipitates are mainly coherent, which means that the lattice is still continuous but distorted causing an increase in strength [18]. The strength loss in the overaged condition is related to the change in precipitate size and number density along with a loss of matrix coherency during heat treatment. This makes it easier for the dislocations to bypass the precipitates through Orowan looping [31].

2.1.4 Effect of dissolved atoms and precipitates

In the precipitation hardened Al-Mg-Si alloys, the overall hardness (and thereby the yield strength) is due to the contribution of several hardening mechanisms. On a macroscopic level, the yield strength is the sum of three contributions, as seen from Equation (2.2).

$$\sigma_{ys} = \sigma_i + \sigma_{ss} + \sigma_p \quad (2.2)$$

Here σ_i is the intrinsic yield strength of pure aluminium, σ_{ss} is the contribution from alloying elements in solid solution and σ_p is the contribution from precipitation hardening [26, 31, 32]. Figure 2.6 illustrates how the contribution from dissolved alloying elements in solid solution and hardening particles influence the strength of the alloy. The effect from dissolved elements is due to the distortion of the space lattice, that sets-up a strain field around them, which

increases the tensile strength of the material. In Al-Mg-Si alloys, elements as Mg, Si and Cu give rise to considerable solid solution hardening [18, 32].

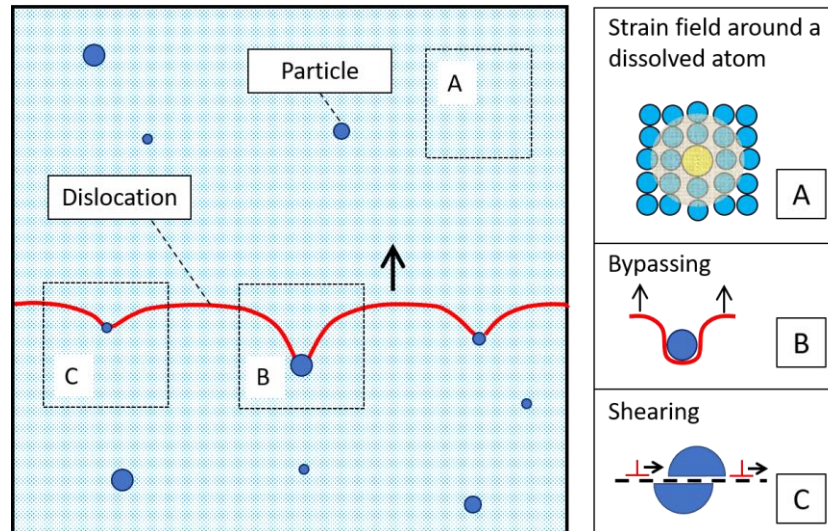


Figure 2.6 Contribution from dissolved alloying elements in solid solution (A) and precipitation hardening (B, C). Dislocations may move either due to bypassing through Orowan looping (B) of large particles or by shearing in the case of smaller particles (C). Copied from [27, 33].

The strength contribution from precipitation hardening is due to shearing and bypassing of particles by dislocations. The smallest particles are usually coherent with the matrix so that dislocations can cut them, but only at stress levels much above those required to move the dislocation through the matrix. For larger particles the dislocation move by bypassing through a mechanism known as Orowan looping [27]. By this means, both shearing and bypassing of the hardening particles by dislocations contribute to the total increase in strength [26, 31, 32].

2.1.5 Grain structure and texture

The grain structure and the crystallographic texture of aluminium alloys influence the mechanical properties. Different crystallographic textures can be obtained depending on the processing method, chemical composition and heat treatment schedule of the specific alloy. For instance, a fibrous grain structure can be retained by adding alloying elements that prevent recrystallization by the formation of dispersoids. For the Al-Mg-Si alloys, such as AA6082, coarse dispersoids are obtained by adding manganese (Mn) and/or chromium (Cr), which will prevent recrystallization during hot working processes like extrusion and hot rolling [19, 34].

The grain structure of the Al-Mg-Si alloys may be recrystallized, partly recrystallized or fibrous (non-recrystallized). Recrystallized alloys such as AA6063 have a cube texture, while the non-recrystallized alloys such as AA6082 have a fibrous texture, as illustrated in Figure 2.7 [19]. The fibrous texture found in AA6082 gives higher strength compared to the recrystallized

texture found in AA6063, which contains less or no Mn. However, the recrystallized material tends to have higher formability [34]. Both the grain structure and the crystallographic texture can cause variations in the mechanical properties [19].

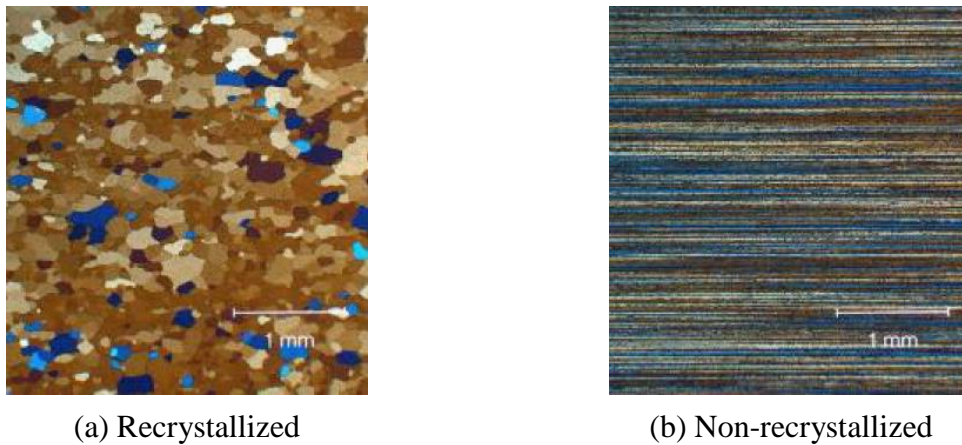


Figure 2.7 Recrystallized and non-recrystallized grain structures. (a) AA6063 and (b) AA6082. (Extrusion direction is horizontal and thickness direction is vertical). Copied from [19].

2.1.6 Fracture mechanisms

In general, aluminium alloys are characterized by a dimple type of fracture which occurs from inclusions or second phase particles. In addition, intergranular, local shear and delamination type of fracture are sometimes observed [35]. In the precipitation hardened Al-Mg-Si alloy, a diversity of fracture mechanism can occur due to the complexity of the microstructure [19]. Both the grain structure and the crystallographic texture can cause variations in the mechanical properties. The intermetallic constituent particles, dispersoids, precipitates and precipitation-free zones will cause an inhomogeneous strain field and preferential fracture initiation and crack growth [19].

2.2 Fusion welding of Al-Mg-Si alloys

2.2.1 Defects related to fusion welding

Although fusion welding, such as gas metal arc welding (GMAW), is commonly used to join Al-Mg-Si alloys, a diversity of defects can occur. Some of these are illustrated in Figure 2.8. These defects are mainly rooted in the physical properties of aluminium, such as its thermal characteristics, its oxide characteristics and the solubility of hydrogen in molten aluminium, which will affect the weld [5]. The impact of these properties will be explained in the following.

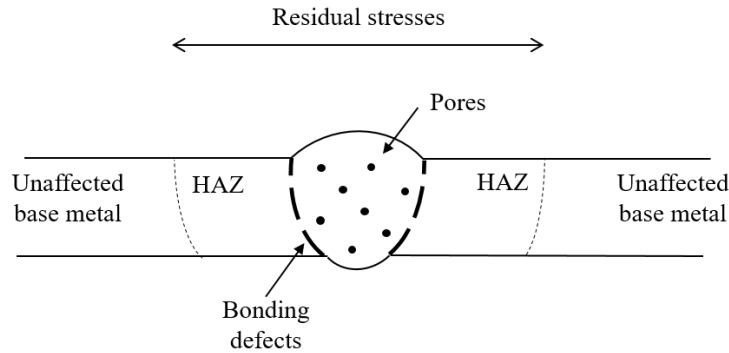


Figure 2.8 Illustration of some common defects caused by fusion welding of aluminium. Copied from [20].

The high thermal conductivity of aluminium causes most of the energy supplied to locally heat the base metal. In contrast, only a small amount contributes to melting and thereby to coalescence and bonding [4, 5]. The local heating contributes to the formation of a soft heat affected zone (HAZ) around the weld, causing a strength reduction in this region. Another consequence of the excessive heating related to fusion welding is the residual stresses that are built-up in the weld region. This may also lead to global deformation and distortions [4].

Furthermore, aluminium is characterized by a high coefficient of thermal expansion and solidification shrinkage. This, combined with a relative wide solidification temperature range, makes the Al-Mg-Si alloys susceptible to solidification cracking and hot cracking [4, 5]. The result of solidification shrinkage in a AA6005-T4 alloy subsequent to GMAW is seen in Figure 2.9, leading to a center-line crack formation.

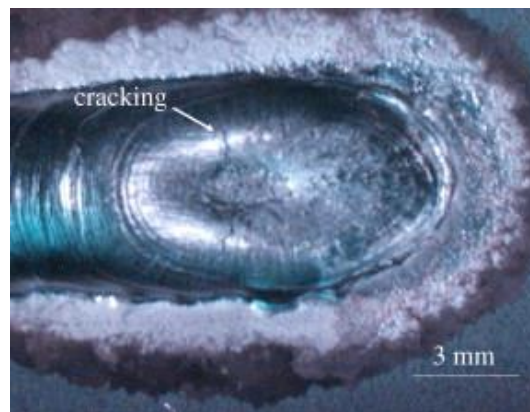


Figure 2.9 Solidification crack formation in the fusion zone in GMA AA6005-T4 weld. Copied from [36].

Problems related to bonding defects are associated with the oxide layer. Since aluminium has a strong chemical affinity to oxygen, it will oxidize immediately when exposed to air. For bonding to take place, the oxide layer needs to be removed or displaced, otherwise, it will result

in incomplete fusion. In addition, the aluminium oxide has a melting temperature approximately three times greater than the base material, which is a challenge [5].

Pore formation is a considerable issue in fusion welding of aluminium alloys due to the presence of hydrogen in form of grease, oxides, dirt and contaminated shielding gas. The solubility of hydrogen is much higher in liquid aluminium compared to in the solid state, as seen from Figure 2.10. The rapid solidification “traps” the hydrogen inside the weld, which triggers the pore formation and may causes a porous material [18].

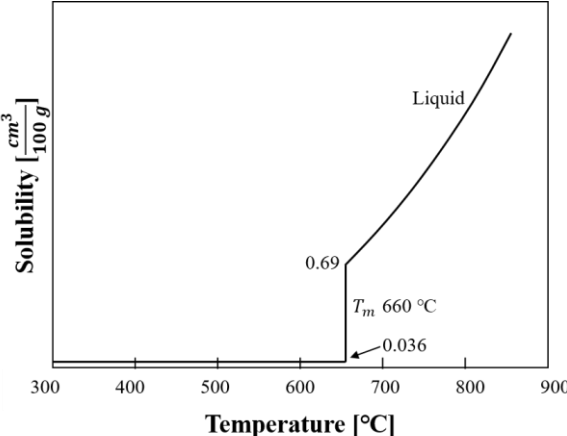


Figure 2.10 Hydrogen solubility in pure aluminium as a function of temperature. Copied from [5].

2.2.2 Microstructure and strength

All fusion welds exhibit distinctly different microstructural regions, which depend upon the temperature the region is exposed to [2]. Different zones can be identified as a result of local changes in alloy composition and/or peak temperature during welding. This is illustrated in Figure 2.11. These zones can vary considerably, depending on the applied heat input and the geometry of the joint [37].

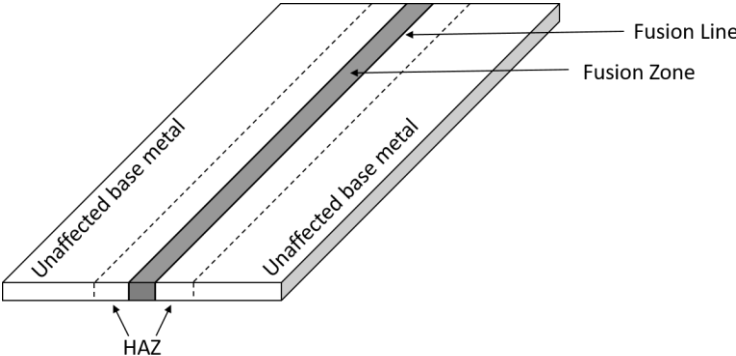


Figure 2.11 Sketch of the different zones which may form in a welded component.

During fusion welding the microstructure of the fusion zone (FZ) goes back to the as-cast state, as seen in Figure 2.12. This causes a “memory loss” of all the past processing steps aimed to increase the strength of the alloy.

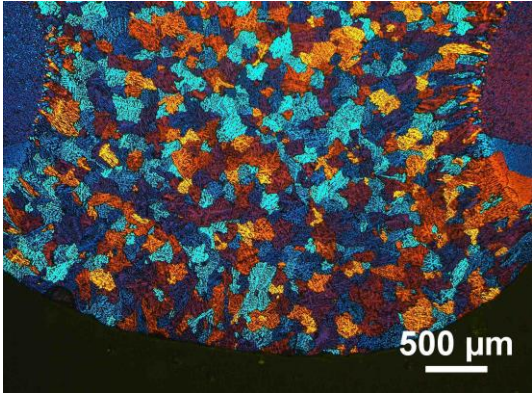


Figure 2.12 Optical micrograph showing the fusion zone of an aluminium alloy welded using a AA5183 filler wire. Copied from [38].

During artificial aging, a high density of fine needle shaped β'' particles is formed uniformly in the matrix. However, these particles are thermodynamically unstable in a welding situation. The smallest β'' -precipitates will start to dissolve in parts of the HAZ where the peak temperature has been above 250°C, while the largest ones will continue to grow. Close to the fusion line full reversion of the β'' -particles is achieved. At the same time, coarser rod-shaped β' -precipitates may form in the intermediate peak temperature range between 250 and 450 °C [26]. The effect of welding on the HAZ precipitate evolution is illustrated in Figure 2.13.

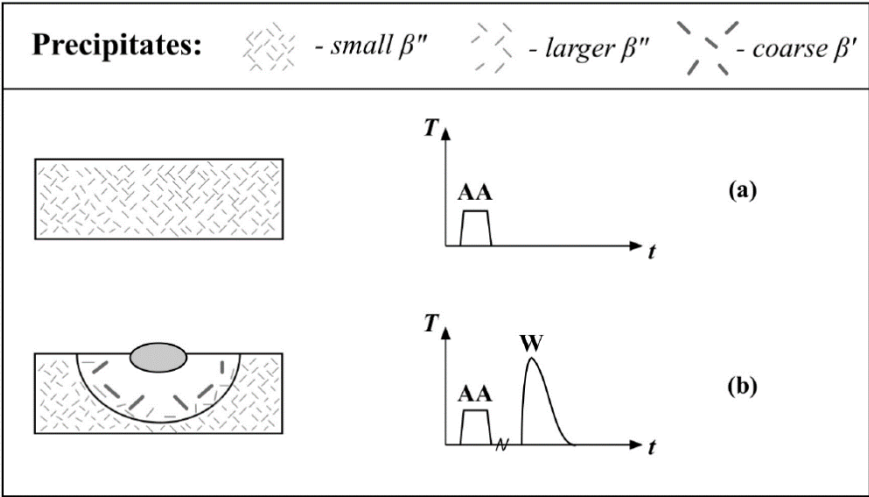


Figure 2.13 Schematic diagram showing the microstructure evolution during thermal processing of Al-Mg-Si alloys involving heat treatment and welding. Copied from [26].

Close to the fusion line, a large fraction of alloying elements will remain in solid solution at the end of the weld thermal cycle, giving conditions for extensive age-hardening over a period of

5-7 days [4]. This will contribute to some recovery in strength close to the fusion zone, as seen from Figure 2.14. From the same figure, it can be seen that the HAZ represents the weakest part of the weld. This is because the local yield strength and hardness distributions correlate well with each other particularly in Al-Mg-Si weldments [27].

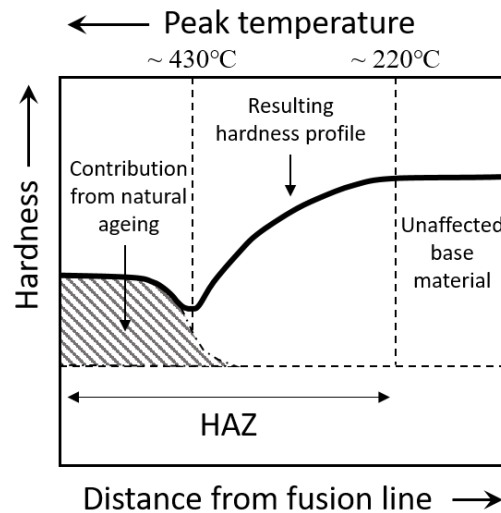


Figure 2.14 Relation between peak temperature and hardness distribution in an AA6082-T6 weld. Copied from [4].

2.2.3 Mechanical properties of GMAW AA6082-T6 joints

The mechanical properties of GMA AA6082-T6 joints have, among others, been determined by Breivik [38]. In the following, the main results from her hardness measurements, tensile testing and Charpy V-notch testing, carried out in the transverse direction of the 3 mm thick profiles, will be presented.

The hardness data are presented in Figure 2.15, showing the hardness profile (on both sides) in the transverse direction of the weld. The minimum hardness is found in the HAZ approximately 9 mm from the weld center-line on both sides, where the minimum HAZ hardness is found to be 62 HV and 57 HV, respectively. Full recovery of the base material hardness is observed approximately 19 mm from the weld center-line.

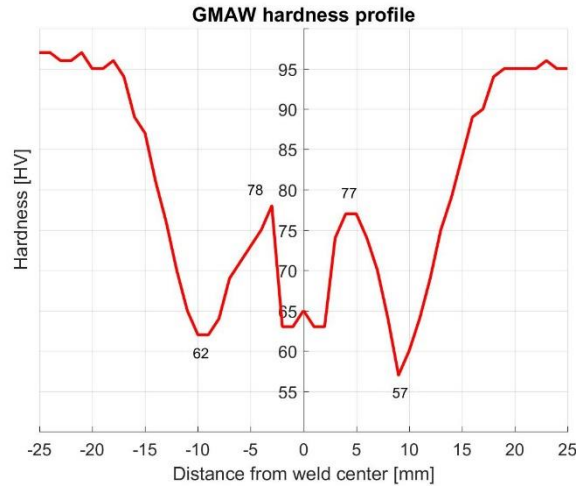


Figure 2.15 Transverse hardness profile of the AA6082-T6 GMA joint being examined by Breivik [38].

The tensile properties of the weldment were determined by tensile testing of the different weld zones, including the base material (BM), the fusion zone (FZ) and the HAZ. The dimensions of the tensile specimens used are shown in Figure 2.16.

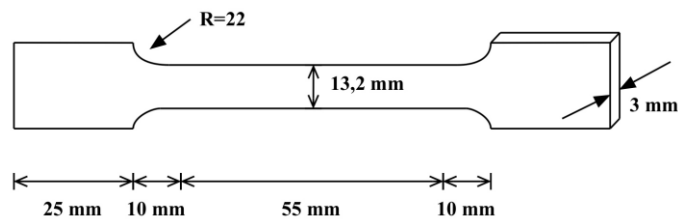


Figure 2.16 Dimensions of tensile specimens used by Breivik [38].

The tensile properties of the different regions are presented by the stress-strain curves in Figure 2.17. The offset yield stress of the base material is approximately 250 MPa, which is much higher compared to the FZ and the HAZ. The same is also true for the tensile strength, where the base material displays a much higher value compared to the FZ and the HAZ. In the latter cases, fracture occurs close to the fusion zone, which probably corresponds to the weakest part of the HAZ [38].

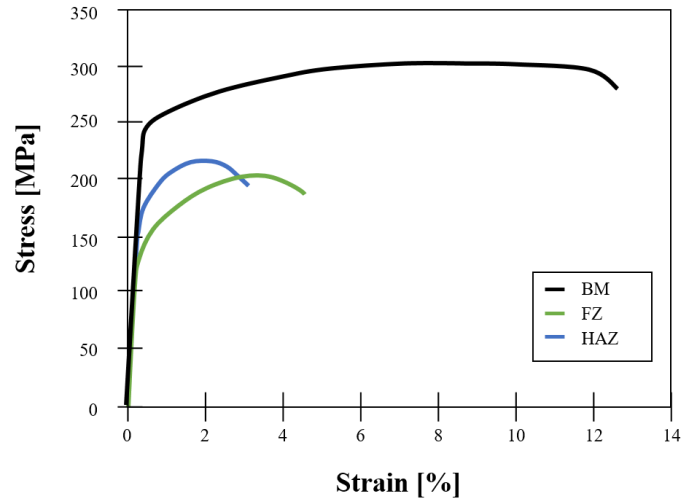


Figure 2.17 Measured stress-strain curves for selected tensile specimens, sampling different zones in the AA6082-T6 GMA joint being examined by Breivik [38].

Charpy V-notch testing was carried out both in the base material and the HAZ. The dimensions used for the Charpy specimens are shown in Figure 2.18.

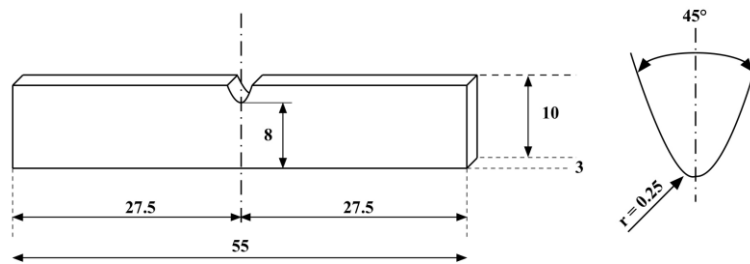


Figure 2.18 Dimensions of Charpy V-notch specimens used by Breivik [38].

The absorbed energy for the different zones is presented in Figure 2.19. It can be seen that the base material absorbs significantly more energy than the HAZ. This shows that the HAZ is also critical when it comes to impact toughness, and not only strength.

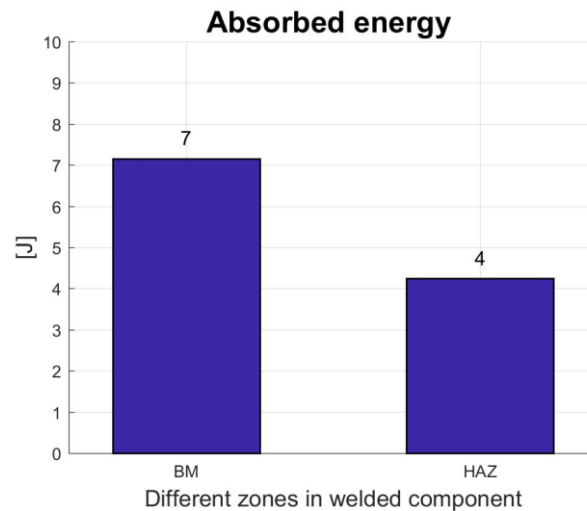


Figure 2.19 The absorbed energy of selected GMAW Charpy V-notch specimens sampling the base material and HAZ. Data from Breivik [38].

2.3 Solid state joining

2.3.1 Metallic bonding

To obtain sound joints in the solid state, metallic bonding needs to be achieved. Metallic bonding can be understood by imagining a cloud of free negatively charged valence electrons that are enveloping the ionized positive charged atoms, as illustrated in Figure 2.20. To obtain metallic bonding between two interfaces they need to be brought together at an atomic scale, so that attractive forces between the positively charged atoms and the electron cloud are established [14].

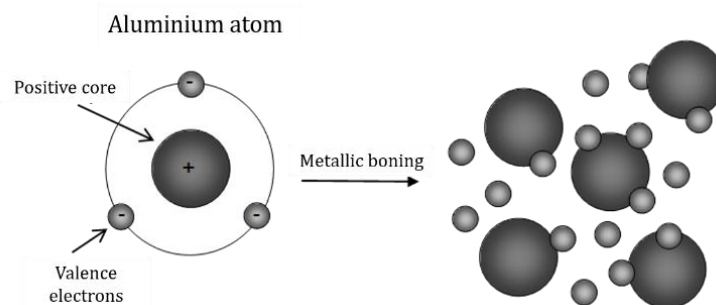


Figure 2.20 Illustration of metallic bonding. Copied from [14].

2.3.2 Solid state processes

Solid state joining processes produce sound joints at a temperature below the melting temperature of the parent material. Bonding between the components is obtained using extreme deformation and diffusion under the action of mechanical, electrical or thermal energy. There

is a diversity of solid state joining processes available for commercial use. For instance, forge welding, ultrasonic welding, cut welding, explosion welding, cold pressure welding, friction welding and friction stir welding. The process of choice is dependent on the final product to be joined [13, 14]. In the following, only friction welding and cold pressure welding will be explained more in detail.

Friction welding processes use the relative motion between two surfaces to achieve frictional heating and bonding, where one part is moving while the other one is kept stationary during the process. Some of the material is removed from the weld as flash, due to the combined action of applied stress and part movement [39]. There are several variants of this process, for instance, rotary, orbital, linear and angular friction welding. The rotary friction welding process is of certain interest since it has formed the basis for friction stir welding [40].

In rotary friction welding, the moving part is rotated relative to the other, as seen in Figure 2.21. With continuous drive, the cold parts are initially subjected to dry friction and will eventually reach a stage of plastic deformation. When plastic deformation is obtained, the rotation is stopped and axial pressure is applied to consolidate the weld [41]. However, HAZ softening is still present due to the extensive frictional heat generated through the process.

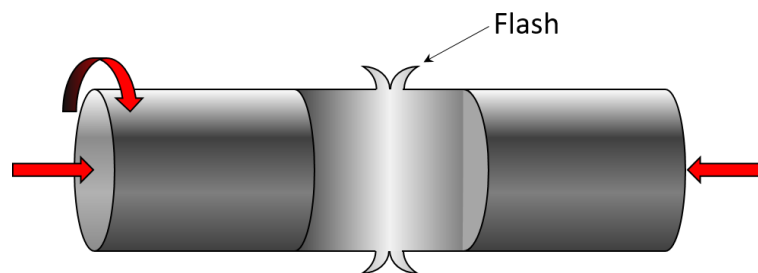


Figure 2.21 Rotary friction welding. Copied from [40].

Cold pressure welding (CPW) is carried out at room temperature without the addition of heat. The two workpieces are joined by the use of external pressure, causing a substantial plastic deformation of the material [2]. The plastic deformation occurring breaks up the oxide layer on the surface and subsequently metallic bonding is achieved, as illustrated in Figure 2.22.

From Figure 2.22(a) it can be seen that the surrounding oxide layer prevents contact between the virgin metal. However, when the external pressure is applied in the longitudinal direction, the workpieces are forced together causing an expansion of the contact surface. This expansion causes the oxide layer to break-up. Some of the oxide is also removed together with the flash, as seen from Figure 2.22(b). Metallic bonding is then achieved at the interface when contact is reached at an atomic level [9, 42].

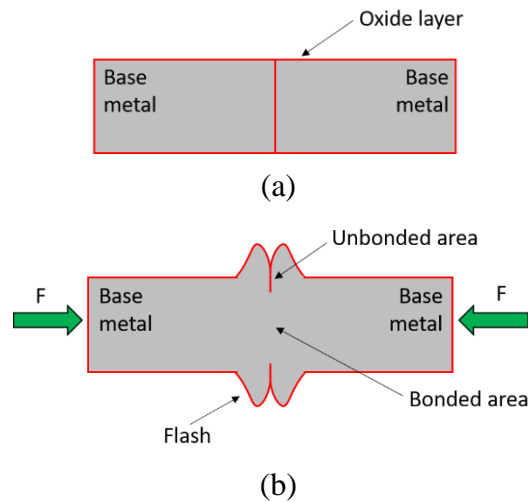


Figure 2.22 Schematic illustration of steps in CPW. (a) The two aluminium workpieces which shall be welded are surrounded by an oxide layer. (b) When the external force is applied, the workpieces are forced together and metallic bonding is achieved across the center-line. Copied from [9].

While there is no formation of a HAZ, the CPW process produces a mechanically affected zone (MAZ) adjacent to the bond region, where the material has been subjected to strain hardening imposed by the plastic deformation [2]. The tensile strength of CPW of a commercial pure aluminium alloy has shown that the bond is actually stronger than the base material. Hence, failure occurs away from the bond line in the unaffected base material [43]. This is a considerably advantage from a mechanical design point of view. Thus, CPW represents the ideal joining situation for aluminium [9, 37]. However, the use of CPW is limited to certain simple geometries e.g. joining of electrical cables and wires in aluminium and copper.

2.4 Friction Stir Welding (FSW)

2.4.1 The Process

The FSW process uses a rotating tool that is firmly pressed against the contacting surfaces of two abutting or overlapping plates. From the base of the tool (the shoulder) a probe (pin), with length marginally shorter than the plate thickness, protrudes. The rotating pin generates frictional heat between the two base metal plates. This causes the material to “soften” and deform plastically [12, 44, 45]. While the tool traverses along the joint line, the material is swept around the pin. The deformed material is constrained by the tool shoulder which is in contact with the top surface of the workpiece, avoiding the softened material to expel [12, 45]. An illustration of the FSW process used for butt joining of plates is shown in Figure 2.23.

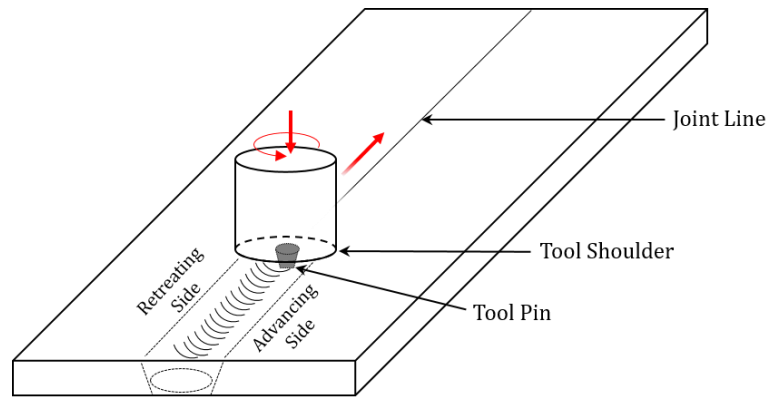


Figure 2.23 Illustration of FSW process used for butt joining of plates. Copied from [12].

The side of the weld where the tool rotation is the same as the welding direction, is referred to as the advancing side. The opposite side of the weld is then referred to as the retreating side. The local motion of the retreating side opposes the forward motion and extrudes the plasticized material behind the tool. During processing, the workpieces must be clamped onto a steel backing plate and secured against the vertical, longitudinal and lateral forces, which will try to lift and push the aluminium plates apart. [45]. FSW is an asymmetric process which generates very high strains and strain rates compared to other solid state metalworking processes, such as extrusion, rolling and forging. In general, the maximum temperature reached stays below 500 to 550 °C [12].

2.4.2 Microstructure and strength

In FSW of aluminium alloys, three effective zones with differing material flow patterns and associated temperature changes can be identified. These are the weld nugget, the thermomechanically-affected zone (TMAZ) and the heat affected-zone (HAZ), respectively, as seen from Figure 2.24. The material flow and temperature in these zones have an impact on the microstructure and strength of the joined section.

The weld nugget is found in the center of the weld, where the material is swept by the tool pin as it rotates and traverses along the weld seam. In this region, the temperature is relatively high, due to the frictional heat generated through the process. During welding, the metal is heavily deformed and thus grain refinement takes place, causing the formation of a fine grained microstructure [12, 13]. Strength recovery is commonly observed in the weld nugget due to natural aging [12, 46].

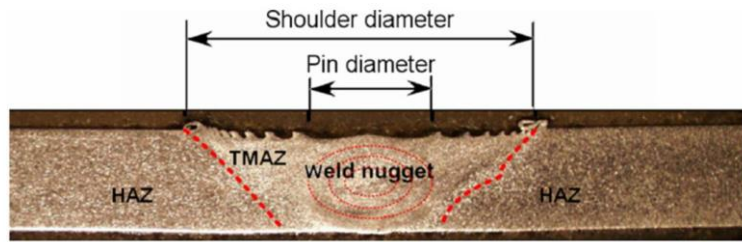


Figure 2.24 Classifications of various regions in a friction stir weld of the AA6061-T6 type. Copied from [47].

The TMAZ is located outside the weld nugget. In this region, the material is both heated and deformed causing the microstructure to consist of elongated and deformed grain. However, the deformation is not large enough to recrystallize the material. The microstructure of the TMAZ evolves mainly through dissolution and coarsening of the hardening phases [46].

At the outer border of the TMAZ, the HAZ is found. Here there is no obvious change in the microstructure. However, the thermal heat generated through the process is efficient enough to modify the state of precipitation [12, 46]. Usually, a significant drop in hardness is observed at the TMAZ/HAZ interface, as seen from Figure 2.25. This is associated with the low or moderate strain hardening capacity of the weaker HAZ compared to the TMAZ, causing an acceleration of the plastic localization process [46].

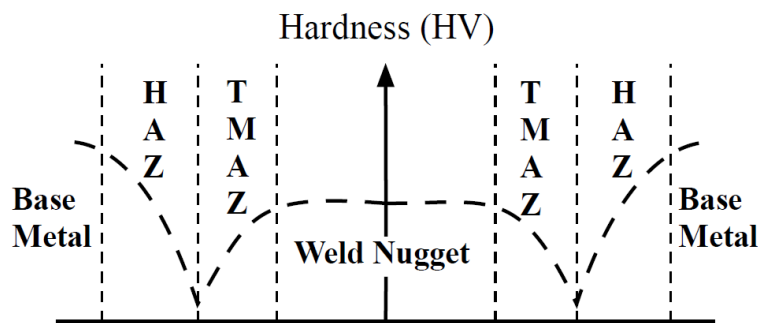


Figure 2.25 Schematic illustration of the typical hardness distribution of a FS joint. Copied from [46]

One of the greatest advantages of FSW is the elimination of the fusion zone with its as-cast microstructure. Instead the presence of a TMAZ with superior mechanical properties is introduced [9, 12]. In addition, the high welding speed tends to lead to a narrower HAZ, and the nugget hardness is also often higher compared to the fusion zone of a GMA weld due to the reduced deformation temperature and increased strain rate that this process offers. However, a soft HAZ is still present in the FSW joint, and this may be a concern [12].

2.4.3 Mechanical properties of friction stir welded AA6082-T6 joints

The mechanical properties of friction stir AA6082-T6 joints have, among others, been determined by Breivik [38], using the same procedure as described earlier for the GMA AA6082-T6 joints. In the following, results from her hardness measurements, tensile testing and Charpy V-notch testing, carried out in the transverse direction of the 3 mm thick profiles, will be presented.

The measured hardness profile in Figure 2.26 reveals a small difference in hardness between the advancing side (AS) and the retreating side (RS). The minimum hardness is found approximately 5 mm from the weld center-line on both sides, and yielding values of 70 HV and 72 HV, respectively. In contrast, the measured hardness in the base material (BM) is approximately 100 HV.

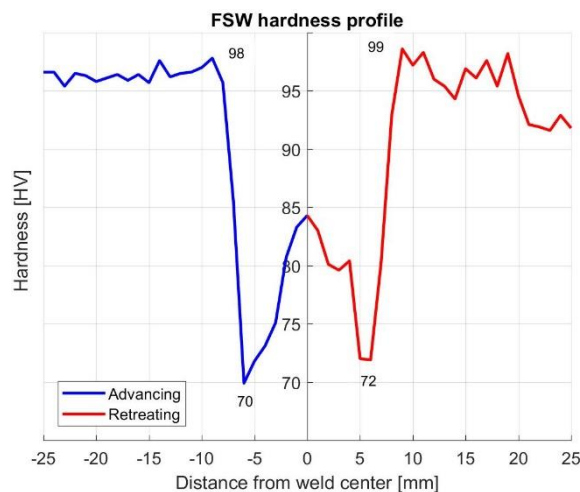


Figure 2.26 Transverse hardness profile of the AA6082-T6 FS joint being examined by Breivik [38].

The tensile properties of selected FSW tensile specimens, sampling different weld regions, are presented in Figure 2.27. Here, the weld nugget is referred to as the stir zone (SZ). The offset yield stress of the BM reaches approximately 250 MPa, while the yield strength of the SZ is approximately 160 MPa. The HAZ/TMAZ also reveals significantly lower yield strengths compared to the base material. Furthermore, the base material tensile strength is seen to approach 300 MPa, whereas the tensile strength of SZ and HAZ/TMAZ is close to 215 MPa.

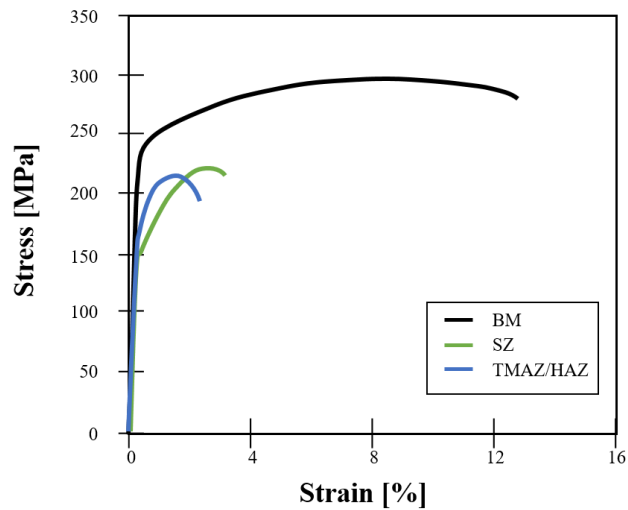


Figure 2.27 Measured stress-strain curves for selected tensile specimens, sampling different regions within the FS AA6082-T6 joint being examined by Breivik [38].

The FS joint's response to impact is presented in Figure 2.28, showing the energy absorption of selected specimens sampling the BM and the HAZ/TMAZ. As can be seen from the figure, the energy absorption is approximately the same for the BM as for the HAZ/TMAZ. However, the HAZ/TMAZ seems to have a slightly higher impact toughness compared to the base material.

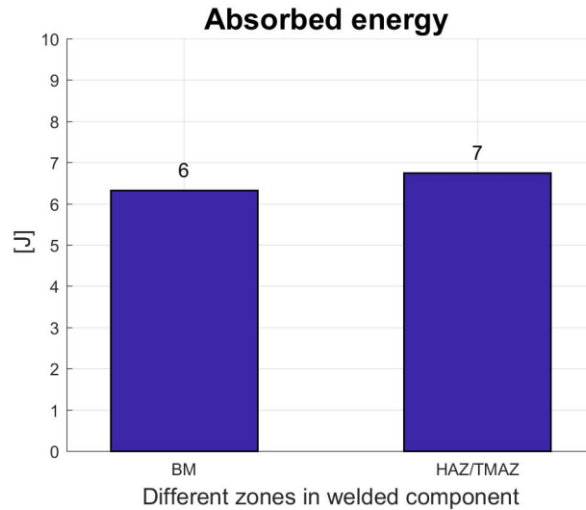


Figure 2.28 Absorbed energy of selected FSW Charpy V-notch specimens, sampling the base material and the HAZ/TMAZ. Data from Breivik [38].

2.5 Hybrid Metal Extrusion & Bonding (HYB)

2.5.1 Principles behind the technology

The Hybrid Metal Extrusion & Bonding (HYB) process is based on the principles of continuous extrusion. In the following, these principles will be explained more in detail.

Extrusion is the process where the cross section of a metal billet is reduced by forcing it to flow plastically through a die under high pressure. Due to the high pressure needed in extrusion processes, most metals are extruded under hot conditions, which reduces the deformation resistance. However, cold extrusion is possible for many metals. The two main types of extrusion are *direct extrusion* and *indirect extrusion*, as illustrated in Figure 2.29(a) and Figure 2.29(b), respectively. In the case of indirect direct extrusion there is no relative motion between the container and the billet. Thus, the friction force is lower compared to direct extrusion. Hence, this process requires less power compared to direct extrusion [27].

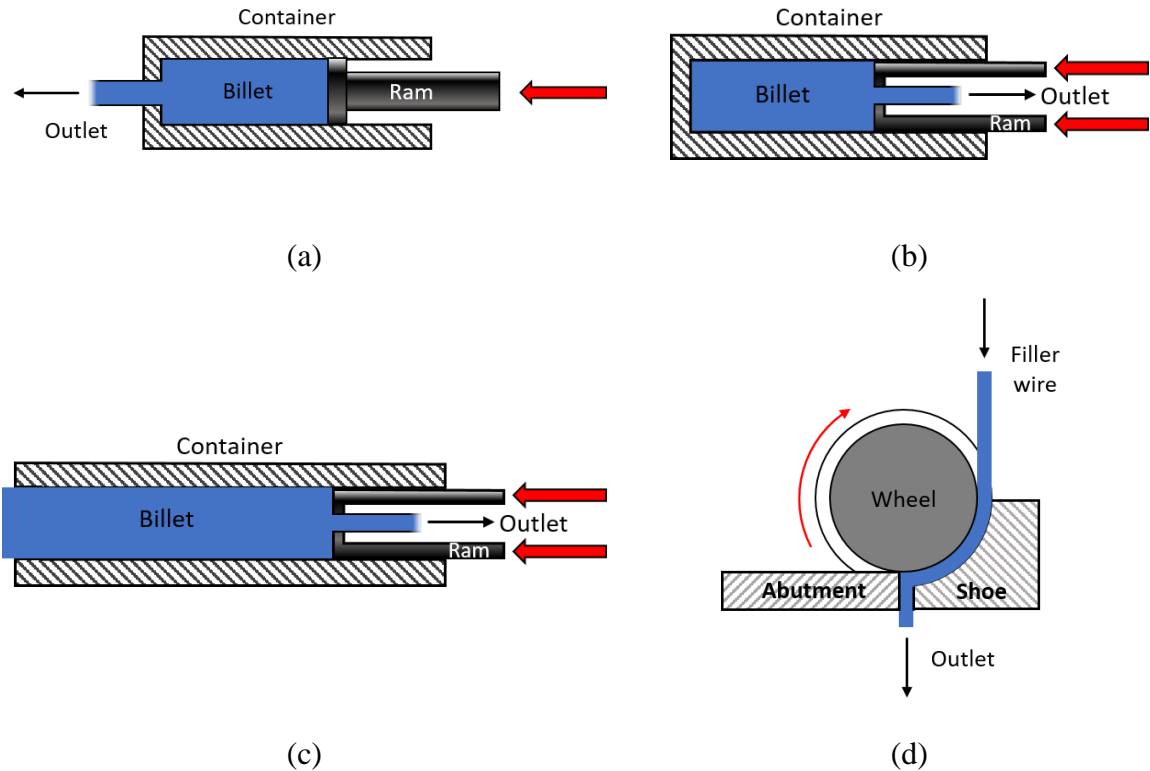


Figure 2.29 Schematic illustration of different types of extrusion. (a) Direct extrusion, (b) indirect extrusion, (c) indirect extrusion where the bottom plate is removed and (d) continuous extrusion. Copied from [48].

Continuous extrusion (also referred to as the Conform process in literature) has some similarities to indirect extrusion, where the die is pushed into the billet in a closed container. Now, imagine the billet to be very long and the container to have equivalently large dimensions. As long as the frictional force between the walls and the billet is greater than those required to

push the billet through the die, the bottom plate can be removed and extrusion is still possible [48]. Thus, the friction force along the walls will keep the billet in place, as illustrated in Figure 2.29(c).

Obviously, continuous extrusion has similarities with the case outlined in Figure 2.29(c). In continuous extrusion, the moving die is replaced by a rotating extrusion wheel, where the wheel is provided with a slot for metal feeding, a stationary shoe with an abutment and a die. This is illustrated in Figure 2.29(d). Since the slot is moving, while the shoe is kept stationary, there will be a net frictional force setup on two of the four contacting sides, as illustrated in Figure 2.30 [49]. To obtain extrusion in this case, a stationary abutment fixed to the shoe punctures the slot. This leads to pressure build-up ahead of the abutment and eventually forces the material to flow plastically out of the die.

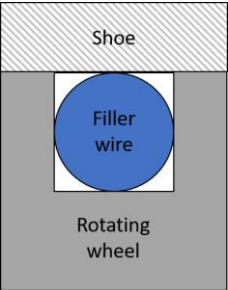


Figure 2.30 Illustration of moving and stationary parts in continuous extrusion.

2.5.2 The Process

The HYB PinPoint extruder is built around the rotating drive pin which is provided with open dies at the lower conical end, as illustrated in Figure 2.31. The pin design is customized to the specific joining situation, depending both on the base plate and the groove geometries. In the drawing shown below the pin is designed for butt joining of plates.



Figure 2.31 Solid Works drawing of the conical pin used for HYB butt joining of plates. (Ø. Grong, Personal Communication, 2017).

A schematic illustration of the main components in the HYB PinPoint extruder is shown in Figure 2.32. The pin, together with the spindle tip (Figure 2.32 (3)) forms a slot, where the filler material (aluminium wire) is feed into the slot from the outside. The aluminium wire is set in motion by the frictional grip imposed by the slot walls and kept in place by a stationary steel housing sealing-off the lower end of the pin (Figure 2.32 (2)). The aluminium wire is then forced to flow against the abutment (Figure 2.32 (4)) blocking the slot and subsequently, due to the pressure built up, continuously extruded through the die openings in the lower end of the pin.

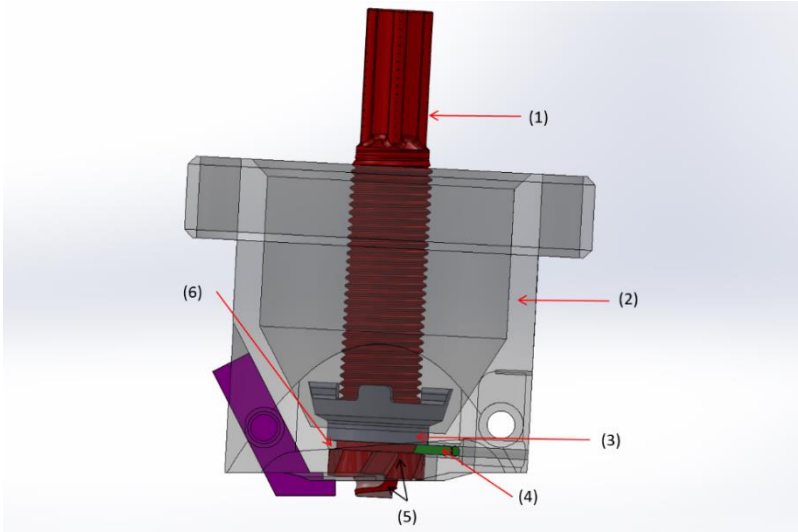


Figure 2.32 Illustration of main components in the HYB PinPoint Extruder head: (1) Pin, (2) Steel housing, (3) Spindle tip, (4) Abutment, (5) Dies and (6) Extrusion chamber. (Ø. Grong, Personal Communication, 2017).

In a real joining situation, the extruder head is clamped against the two aluminium plates to be joined. The plates are separated from each other, so they form a groove. When the extruder head is clamped to the base metal plates, the pin will enter the groove. The pin is slightly larger than the groove, which causes contact between the sidewalls of the groove and the pin, as illustrated in Figure 2.33.

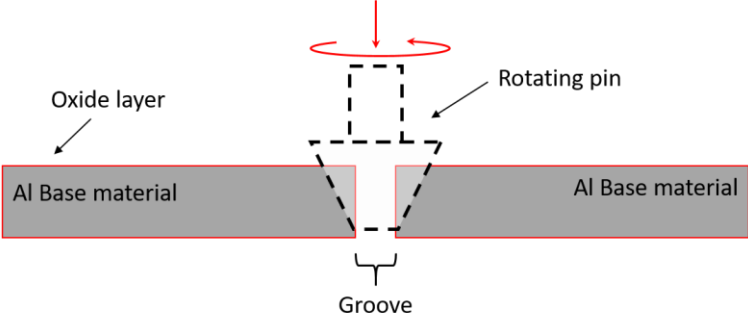


Figure 2.33 Illustration of the rotating pin and its location in the groove during HYB butt welding of plates.

During joining the extruder head moves along the joint line at a constant speed. The wire feed rate is adjusted such that the entire cross-sectional area of the groove can be filled with solid aluminium. The side of the joint, where the tool rotation is the same as the joining, is referred to as the advancing side. The opposite side of the joint is referred to as the retreating side.

At present, the process is standardized for extrusion of $\text{Ø}1.2\text{mm}$ filler wire. The pin diameter is $\text{Ø}10\text{ mm}$. For butt joining of 4 mm aluminium plates, the pin rotates typically at 400 RPM at a welding speed of 6 mm/s. The peak temperature typically lies between 300 °C and 400 °C (Ø. Grong, Personal Communication, 2017).

2.5.3 Bonding

As the pin rotates and travels along the joint line, the oxide layer on the sidewalls (together with some of the base material) will be dragged around by the motion and mixed with the filler metal. Metallic bonding between the sidewalls and filler metal is mainly obtained by the combined action of oxide dispersion and shear deformation, while bonding in the bottom region mainly occurs as a result of surface expansion and pressure (Ø. Grong, Personal Communication, 2017). A cross sectional view of the material flow pattern during HYB butt welding of plates is shown in Figure 2.34.

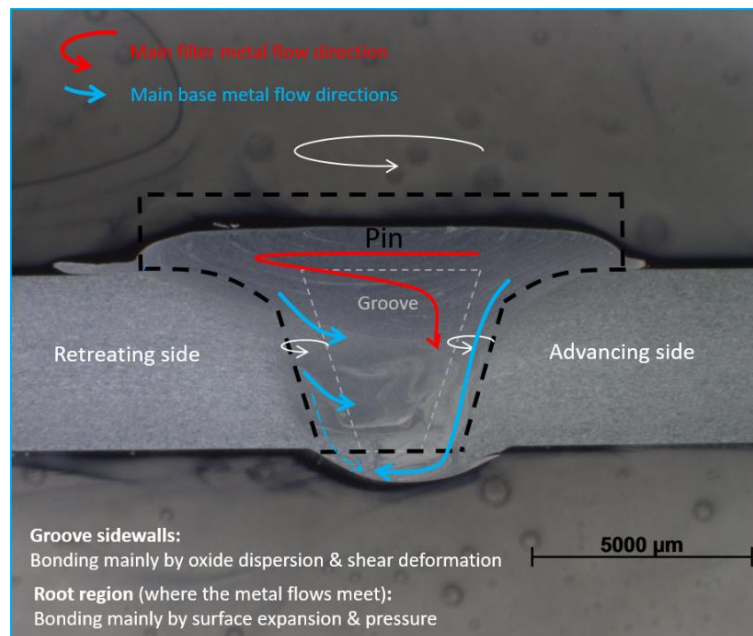


Figure 2.34 Illustration of material flow pattern during HYB butt welding of plates (Ø. Grong, Personal Communication, 2017).

2.6 Load-bearing capacity of welded components

In welding of precipitation hardened aluminium alloys, such as the Al-Mg-Si alloys, HAZ softening is of particular concern. The load bearing capacity of such joints depends both on the width of the HAZ as well as the minimum strength level in this region. Hence, both factors must be taken into consideration in engineering design [50]. In the following, two idealized loading conditions, as illustrated in Figure 2.35, will be examined more in detail.

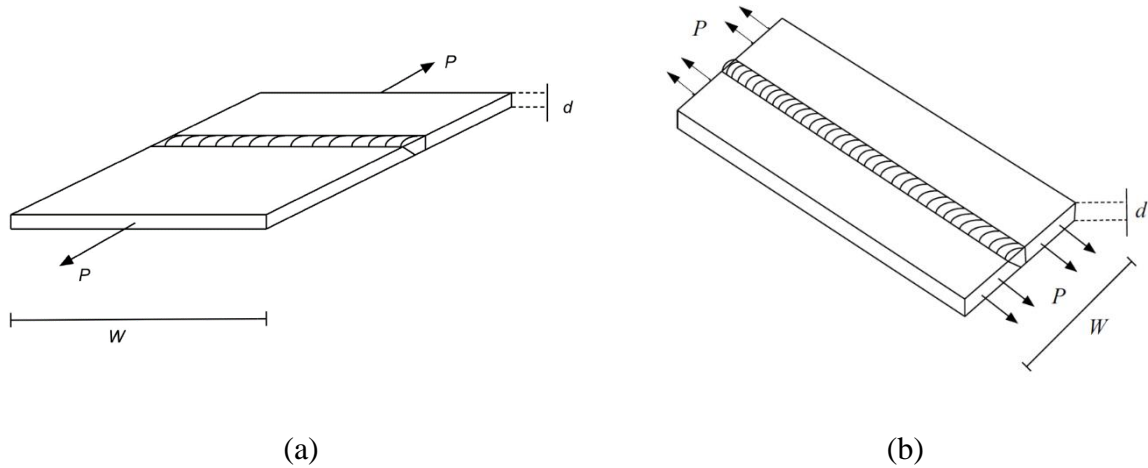


Figure 2.35 The two idealized loading conditions being examined. (a) Loading perpendicular to weld. (b) Loading parallel to weld. Copied from [50].

The yield strength of the HAZ may be calculated on the basis of the measured HAZ hardness profile, using the following relationship [4].

$$\sigma_y [MPa] = 3.0 HV - 48.1 \quad (2.3)$$

By inserting the minimum value from the HAZ hardness profile in Equation (2.3), the corresponding minimum HAZ yield strength σ_{min} can be found. In the case of a perpendicular loading condition (Figure 2.35 (a)), the load bearing capacity P can be calculated as followed.

$$\sigma_{\perp, min} = \frac{P}{d \cdot w} \quad (2.4)$$

where P is then the maximum tensile (or compressive) force that can be applied to the weld, while d and w are the plate thickness and width of the component, respectively [50].

If the load is parallel to the welded section, as shown in Figure 2.35 (b), the design stress can be calculated based on the so-called reduced cross-sectional area, A_{red} . The reduced area approach takes into account that the mechanical properties gradually decreases near to the weld

and reaches a minimum at the center of the weld. The reduced cross-sectional area can be expressed by the following equation [37, 50].

$$A_{red} = A - 2y_{red}^{eq}d(1 - \beta) \quad (2.5)$$

Here, A is the total cross-section area of the joint, including the weld reinforcement and d is the thickness of the plate. Moreover, y_{red}^{eq} is the equivalent half width of the reduced strength zone (including the weld metal) of strength σ_{min} , while β represents a metallurgical efficient factor that considers the degree of softening occurring due to welding ($\beta \leq 1$). As yield is not permitted during service, β is equal to the ratio between the minimum HAZ yield strength (σ_{min}) and the base metal yield strength (σ_b):

$$\beta = \frac{\sigma_{min}}{\sigma_b} \quad (2.6)$$

In a real welding situation, the equivalent half width of the reduced strength zone y_{red}^{eq} of strength σ_{min} can be calculated by considering the idealized strength profile shown in Figure 2.36 and solving the integral:

$$y_{red}^{eq} = \frac{\int_0^{\infty} (\sigma_b - \sigma) dy}{(\sigma_b - \sigma_{min})} \quad (2.7)$$

Then, the load-bearing capacity can be found on the basis of the reduced cross-section area A_{red} , using Equations (2.5) to (2.7).

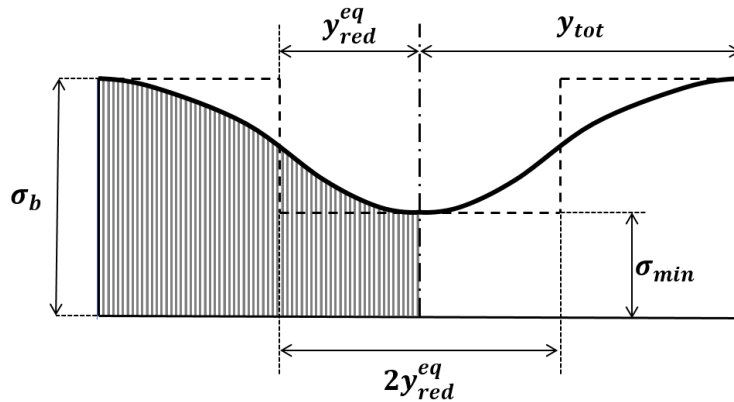


Figure 2.36 Sketch showing how the equivalent half width of the reduced strength zone y_{red}^{eq} of minimum strength σ_{min} is related to an assumed yield strength profile across the weld. Copied from [50].

3 Experimental

3.1 Materials

3.1.1 Base material

In the present welding trials, 4 mm rolled plates of aluminium alloy 6082, received in the T6 tempered condition, were used. The chemical composition of the base metal is shown in Table 3.1. The base material certificate can be found in Figure A 1 in the Appendix. The plates were bought from an external supplier. Therefore, no detailed information about the applied BM homogenization and heat treatment schedules are available.

Table 3.1 Chemical composition of AA6082 used as base metal.

Alloying element (wt.%)									
Si	Fe	Cu	Mn	Mg	Cr	Zn	Ti	Others	Al
0.9	0.45	0.06	0.42	0.8	0.02	0.05	0.02	0.03	Balance

3.1.2 Filler material

The filler material used for joining was a 1.2 mm diameter wire of the AA6082-T4 type, with chemical composition as shown in Table 3.2. This wire is produced by HyBond AS. The material certificate can be found in Figure A 2 in the Appendix. The wire was made from a DC cast billet provided by Hydro Aluminium, which then was homogenized, hot extruded, cold drawn and shaved down to the final dimension. The applied homogenization conditions are shown in Table 3.3.

Table 3.2 Chemical composition of the AA6082 DC cast billets used in the HYB filler wire manufacturing.

Alloying element (wt%)										
Si	Mg	Cu	Mn	Fe	Cr	Zr	Ti	B	Others	Al
1.11	0.61	0.002	0.51	0.20	0.14	0.13	0.043	0.006	0.029	Balance

Table 3.3 Homogenization conditions pertaining to the AA6082 DC cast billets being used in the HYB filler wire manufacturing.

Heat rate (°C/h)	Holding temp. (°C)	Holding time (h)	Cooling rate (°C/h)
200	540	2.25	300

3.2 Joining conditions

The base plates dimensions used in the HYB joining trials were 4mm x 240mm x 60mm. A schematic drawing of the plates is shown in Figure 3.1.

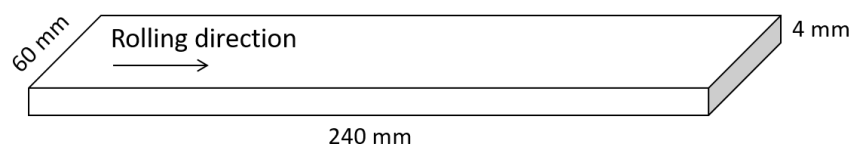


Figure 3.1 Schematic drawing of the plate material used in HYB joining trials. Note that the welding direction is parallel with the plate rolling direction.

Single-pass butt joining of the plates was carried out by HyBond AS, using an I-groove with 3 mm root opening and the filler wire described previously in Section 3.1.2. CO₂-gass was used for cooling. The main welding parameters used are summarized in Table 3.4. The gross heat input (following cooling) was approximately 0.51 kJ/mm .

Table 3.4 Summary of welding parameters used in the HYB joining trials of the 4 mm AA6082-T6 plates.

Welding parameters			
Pin rotation (RPM)	Travel speed (mm/s)	CO ₂ gas flow rate (g/min)	Wire feed rate (mm/s)
400	6	160	142

A photograph of the welded plates received from HyBond AS is shown in Figure 3.2, indicating the welding direction as well as the retreating side (RS) and the advancing side (AS) of the joint.

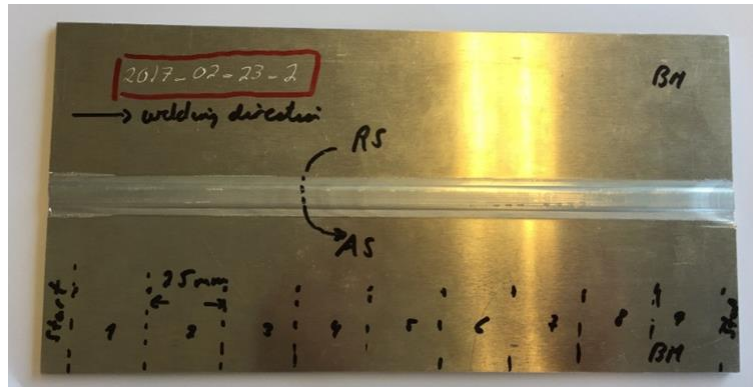


Figure 3.2 Photograph of the butt welded plates received from HyBond AS. Shown is also the welding/rolling direction and the retreating/advancing side.

3.3 Sample preparation and metallographic examination

3.3.1 Sample sectioning

Samples were cut transverse to the welding/rolling direction and numbered, as illustrated in Figure 3.3. The specimens used for the subsequent microstructural investigation and hardness testing are highlighted in yellow in the same figure.

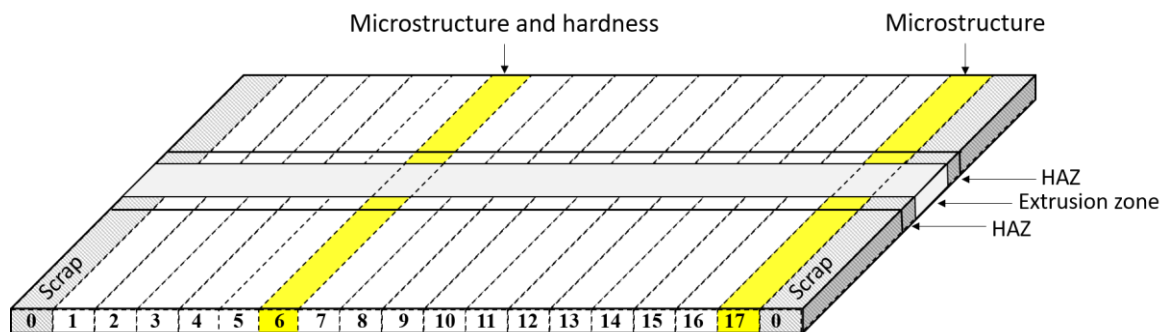


Figure 3.3 Schematic illustration of sample sectioning and numbering of specimens. Specimens used for metallographic examination and hardness testing are highlighted in yellow.

3.3.2 Sample preparation

The samples used for the microstructural investigation and hardness testing were prepared in the following series of steps. First, the samples were cut into sections of approximately 36mm, covering both the AS and RS of the joint, as shown in Figure 3.4. This to ensure that the complete HAZ degradation and material flow pattern could be revealed.



Figure 3.4 Photograph of the specimen used for micrographic examination and hardness testing.

After cutting the samples were cold mounted in a ClaroCit acryl resin. The mounted samples were then ground by the use of SiC grinding paper of increasing fineness (P120, P220, P500, P1000, P2000 and P4000). Water was used as lubricant. In between each grinding step, the samples were rinsed in ethanol.

Grinding was followed by polishing of the samples by the use of 3 μm and 1 μm polishing disks and diamond paste suspensions. DP-Lubricant Blue was used as lubricant. After polishing, the samples were cleaned using an ultrasonic ethanol bath.

The ground and polished samples used for the microstructural examination were immersed in an alkaline sodium hydroxide solution (1g NaOH + 100ml H₂O). The holding time was 3 to 4 min. Then the samples were ready for examination in the optical microscope.

3.3.3 Optical microscopy

The analysis in the optical microscope was done using a Leica DMLB light microscope and an Alicons Confocal Microscope. Figure 3.5 shows the location of the different sections that have been examined. Most of the structures in the weld zone and base material could be revealed at a magnification of 5x.

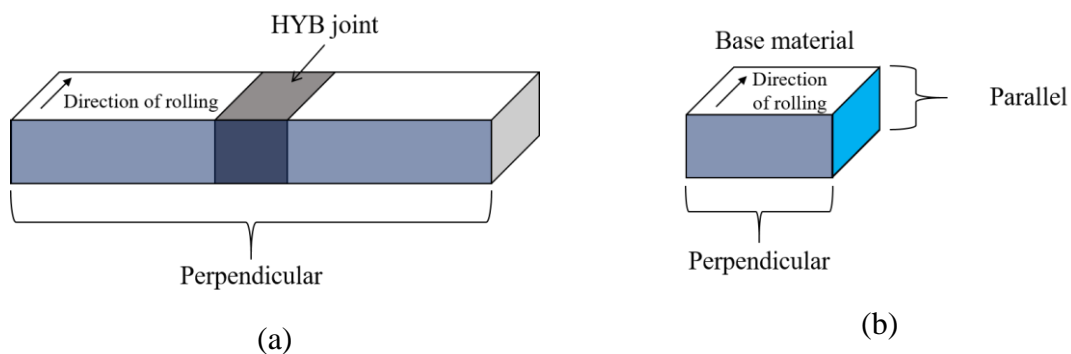


Figure 3.5 Schematic illustration of the different sections that have been examined in the optical microscope. (a) HYB joint and (b) base material.

3.3.4 Hardness testing

The Vickers hardness (HV) was measured on one sample. A total of three different test series were conducted. In-between each test series, the sample was ground and polished before the next one was conducted, employing the same procedure as described earlier in Section 3.3.2. The hardness was measured both in the vertical and the horizontal sample direction, as shown by the black dotted-lines in Figure 3.6. Also, different sets of displaced hardness measurements were performed on both sides of the joint, as indicated by the red dotted-lines in the same figure. The location of the hardness measurements in the different test series can be found in Table A 1 in the Appendix. In addition, the base metal hardness was established from ten individual measurements being randomly taken on a specimen of the unaffected base material.

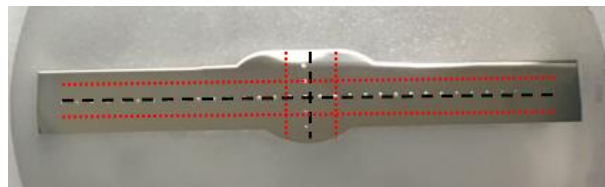


Figure 3.6 Photograph of sample used for hardness testing, indicating the location of the different series of measurements.

The hardness measurements were made using a Mitutoyo Micro Vickers Hardness Testing Machine (HM-200 Series) and a load of 1 kg (HV_1). The distance between each indentation was 0.45 mm, and the full test force was applied for 10 seconds. The displaced hardness measurements were shifted 0.9 mm relative to the specimen mid-section. Note that all these hardness measurements are in accordance with the *ASTM E92-16* standard [51].

3.4 Tensile testing

The samples used for tensile testing were taken from different zones of the weldment, as illustrated in Figure 3.7. These are the extrusion zone (EZ) and the HAZ, respectively. The additional specimens used for tensile testing of the unaffected base metal (BM) were prepared from a separate BM plate supplied by HyBond AS.

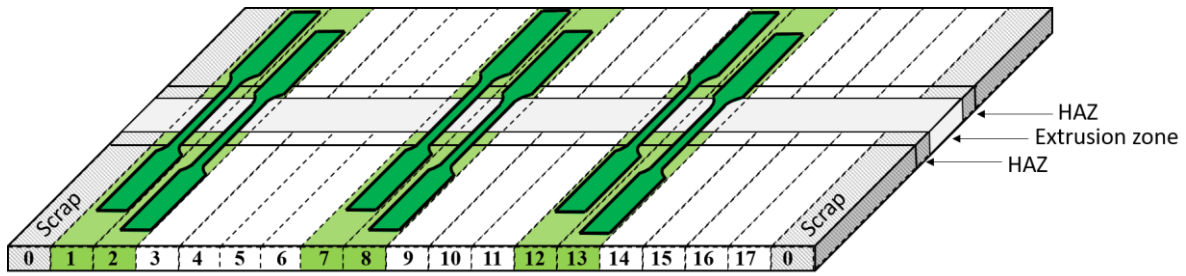


Figure 3.7 Schematic illustration of the location of the different tensile specimens.

The dimensions of the tensile specimens used are shown in Figure 3.8. Limitations in the plate size imposed the use of subsize specimens with dimensions in accordance with the *ASTM E8/E8M* standard [52]. Only flush-machined specimens were used in order to eliminate the potentially strength contribution from the weld reinforcement. This, in turn, makes it possible to compare the tensile test results with those reported previously for GMAW and FSW by Breivik [38].

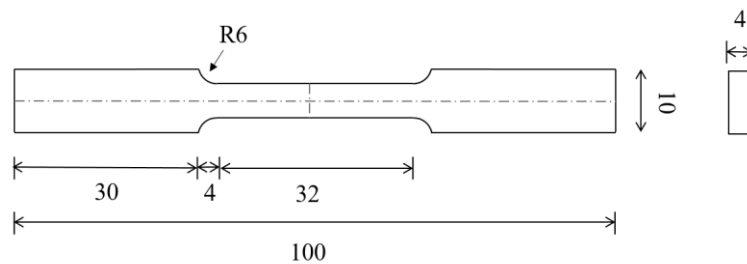


Figure 3.8 Dimensions of the flush-machined subsize specimen used for tensile testing. All values are given in millimetres.

Tensile tests were carried out employing an Instron hydraulic test machine (load cell of 50 kN) at room temperature. The cross-head speed was fixed to $v = 1.5 \text{ mm/min}$, which corresponds to a strain rate of $\dot{\epsilon}_{nom} = 10^{-3} \text{ s}^{-1}$. The axial displacement was measured using an extensometer and a gauge length of 25 mm. The total axial elongation after testing was measured with the aid of a probe being embedded in the hydraulic cylinder of the test machine. The total number of tensile specimens being tested are listed in Table 3.5.

Table 3.5 Total number of tensile test specimens tested.

Location	Number of specimens
Base material	4
EZ	3
HAZ	3
Total	10

3.5 Impact testing

The impact tests were performed to reveal details of the weld energy absorption at very high strain rates ($> 10^3 \text{ s}^{-1}$). The samples used for Charpy V-notch testing were located in different regions on the weld, as shown in Figure 3.9, sampling both the extrusion zone (EZ), the bond line (BL) and the HAZ. The specimens used for sampling of the unaffected base material (BM) impact toughness were prepared from a separate plate of the base material provided by HyBond AS.

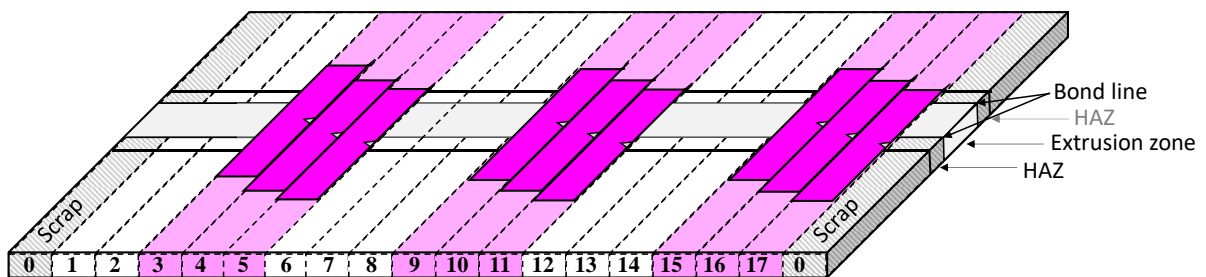


Figure 3.9 Schematic illustration of Charpy V-notch specimens sampling different zones within the HYB joint.

Subsize Charpy V-notch specimens, based on the *ASTM E23-16b* standard, were used in these trials [53]. According to the standard, a specimen thickness of 3 mm should be used. However, due to the risk of residual stresses and heat generation during milling, the thickness was left at 4 mm. Note that all excess material in the extrusion zone was removed prior to testing by milling to fit the standard. The dimensions of specimens used for the Charpy V-notch testing are illustrated in Figure 3.10.

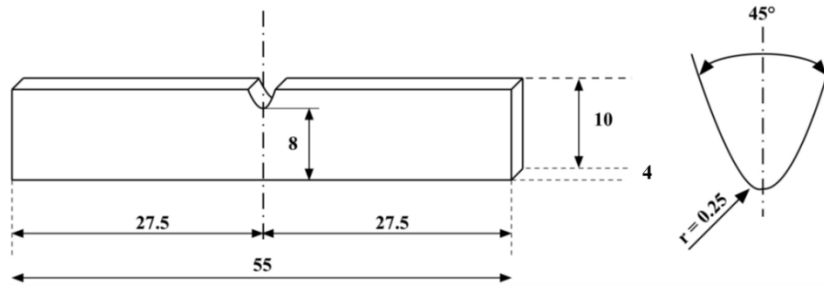


Figure 3.10 Dimensions of subsized Charpy V-notch specimens used for impact testing. All values are given in millimetres.

The total number of specimens tested are listed in Table 3.6. In the table “location” refers to the location of the V-notch.

Table 3.6 Total number of Charpy V-notch specimens tested.

Location	Number of specimens
Base material	3
EZ	3
BL	3
HAZ	3
Total	12

The Charpy V-notch tests were carried out in a Zwick impact testing machine at room temperature, using an impact energy of 450 J. The absorbed energy was measured for each sample. The tests were carried out at SINTEF in Trondheim, Department of Materials Testing.

3.6 Fracture surface analysis in the Scanning Electron Microscope (SEM)

The fracture surface of the broken tensile test and Charpy V-notch specimens were examined in a scanning electron microscope (SEM). The type of the microscope is Quanta FEG 450. The fracture surface examination was performed at an acceleration voltage of 20 kV, while the working distance was set to approximately 10 mm.

4 Results

4.1 Microstructure examination

4.1.1 Base material

The microstructure of the rolled AA6082-T6 base material, both perpendicular and parallel to the rolling direction, are shown in Figure 4.1. Some variations in microstructure in the through-thickness direction can be observed.

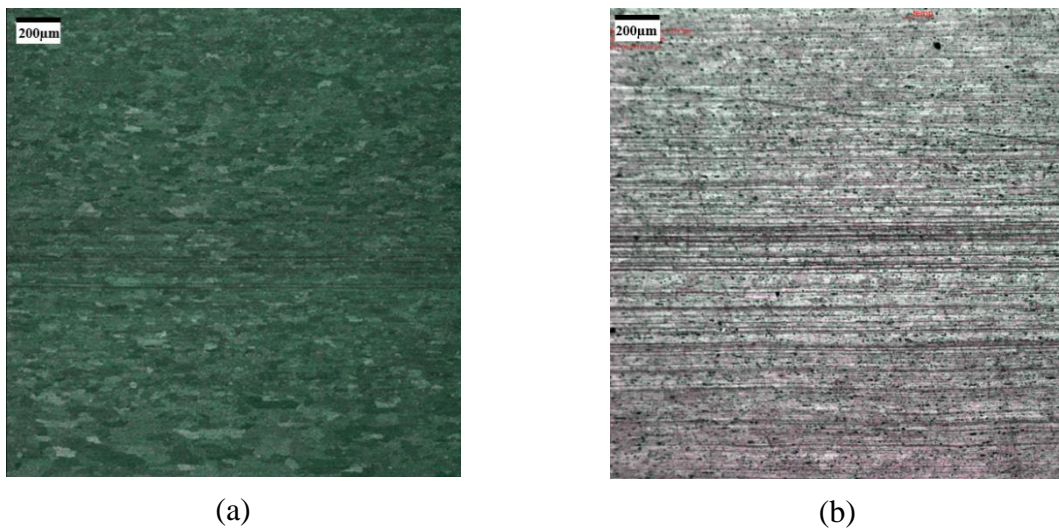


Figure 4.1 Optical micrographs showing the microstructure of the rolled AA6082-T6 base material at low magnification (5x). (a) Section perpendicular to the plate rolling direction and (b) section parallel to the plate rolling direction. (The scale bar in the upper left corner is 200 μm).

A micrograph of the base material parallel to the rolling direction at high magnification is shown in Figure 4.2. Apparently, both recrystallized grains (shaded green areas) and non-recrystallized grain fragments (dark bands) can be observed.



Figure 4.2 Optical micrograph of the AA6082-T6 base metal microstructure parallel to the plate rolling direction at high magnification (20x). (The scale bar in the upper left corner is 50 μm).

4.1.2 HYB joint

An overview of the HYB weld cross-section is shown in Figure 4.3, indicating the RS and AS of the joint. The extent of the plasticized material and the material flow pattern is clearly visible, where the dark region in the center is the flow pattern of the filler material (FM) surrounded by the plastically deformed base material (BM). However, the material flow pattern is not symmetrical, as the FM is mainly located on the top of the weld and on the AS, whereas the BM dominates on the RS.

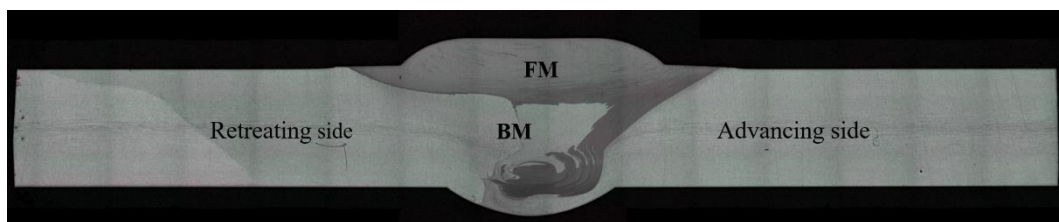


Figure 4.3 Optical micrograph showing the macrostructure of the HYB joint.

A micrograph of the bond line between the filler material and the base metal is shown in Figure 4.4. As can be seen from the figure, the filler material reveals much finer grains compared to the HAZ. Close to the bond line, strongly elongated and heavily deformed grains are visible.

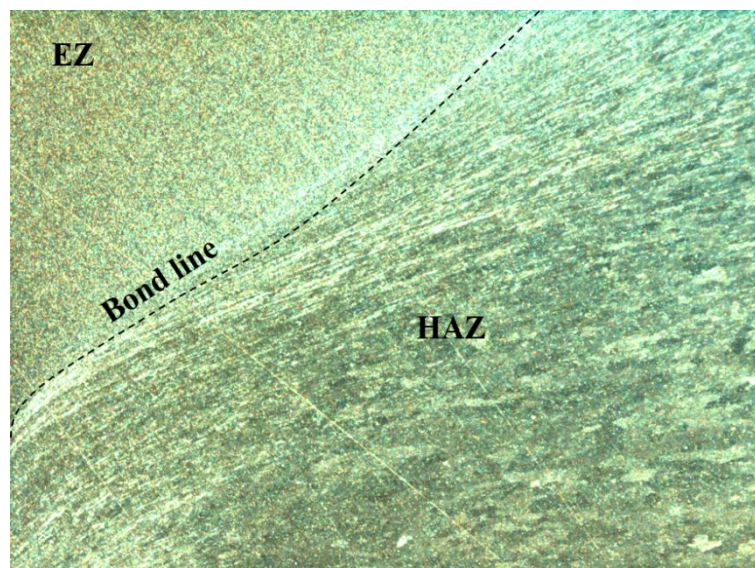


Figure 4.4 Optical micrograph showing changes in microstructure across the bond line between the base material and the filler material in the HYB joint (10x).

4.2 Hardness profiles

The hardness measurements for the base material gave a mean value of 111 HV, with a standard deviation of 2.2. The individual hardness values can be found in Table A 2 in the Appendix.

In the following, hardness measurements carried out in the horizontal and vertical mid-sections of the joint, as shown in Figure 4.5, are presented. In the graphical representations, each hardness point represents the arithmetic means of all three test series carried out in the same section. The individual hardness measurements for all test series can be found in Table A 3 to Table A 6 in the Appendix.

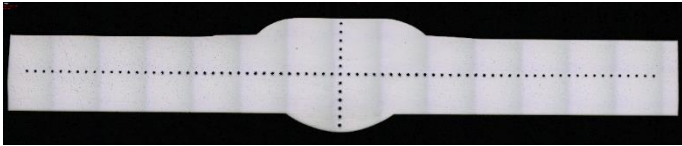


Figure 4.5 Photograph of the hardness indentations taken along the specimen mid-sections in the third test series.

Figure 4.6 shows the resulting hardness profile along the horizontal mid-section of the joint, where the unaffected base material hardness also is indicated. As can be seen from the figure, the hardness profile is relatively smooth and symmetrical, but occurs to be somewhat uneven in the lower part on the AS. The minimum is hardness found on the AS, and yields a value of 66 HV approximately 3 mm from the joint center. On the retreating side, a minimum value of 69 HV is found approximately 5 mm from the center. In contrast, the base metal reaches a maximum hardness of about 115 HV on both sides. The total width of the HAZ is estimated to be approximately 12 mm on both sides.

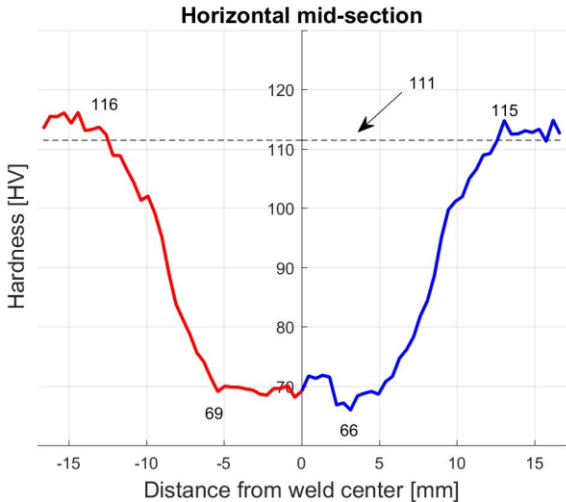


Figure 4.6 Measured hardness profile along the horizontal mid-section of the HYB joint.

The resulting hardness profile measured along the vertical mid-section of the joint is shown in Figure 4.7. From the figure, it is evident that the hardness is higher in the upper region, whereas it decreases towards the bottom of the weld. The maximum and minimum hardness measured are 94 and 59 HV, respectively. However, a small hardness increase can be observed in the lower region at the weld toe, reaching a value of 71 HV.

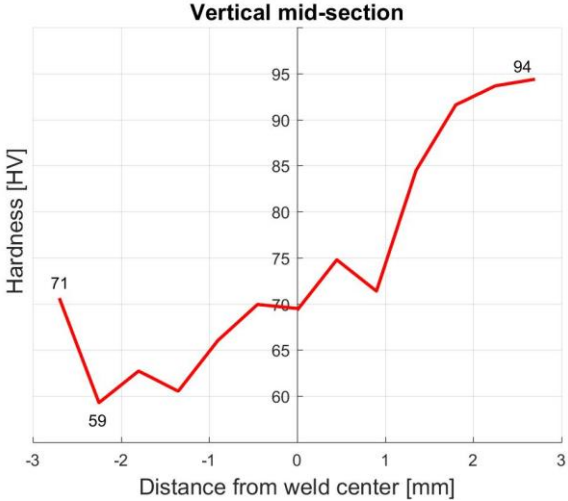


Figure 4.7 Measured hardness profile along the vertical mid-section of the HYB joint.

The measured hardness indentations from the second test series are shown in Figure 4.8.

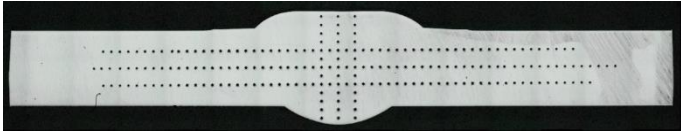


Figure 4.8 Photograph showing the hardness indentations from the second test series.

Figure 4.9 shows the resulting hardness profiles pertaining to the displaced horizontal mid-sections of the joint. The hardness values measured above the mid-section are shown in Figure 4.9(a). As can be seen from the figure, the profile appears to be symmetrical, displaying a minimum hardness of approximately 66 HV and a maximum hardness of 117 HV on both sides of the joint. The total width of the HAZ on the AS and RS is estimated to 12 and 11 mm, respectively.

Figure 4.9(b) reveals the hardness values measured below the horizontal mid-section of the joint. Also in this case, the profile appears to be relatively symmetrical. An exception is the lower part of the profile, which tends to dip more on the advancing side. The measurements display a minimum hardness of 66 HV on the AS, which is similar to that found in Figure 4.6. In this case, the minimum hardness is located 4.5 mm from the joint center-line. On the RS, the minimum hardness is found to be 71 HV, located approximately 6 mm from the joint center-

line. Moreover, the total width of the HAZ is estimated to be about 10 mm on both sides of the joint.

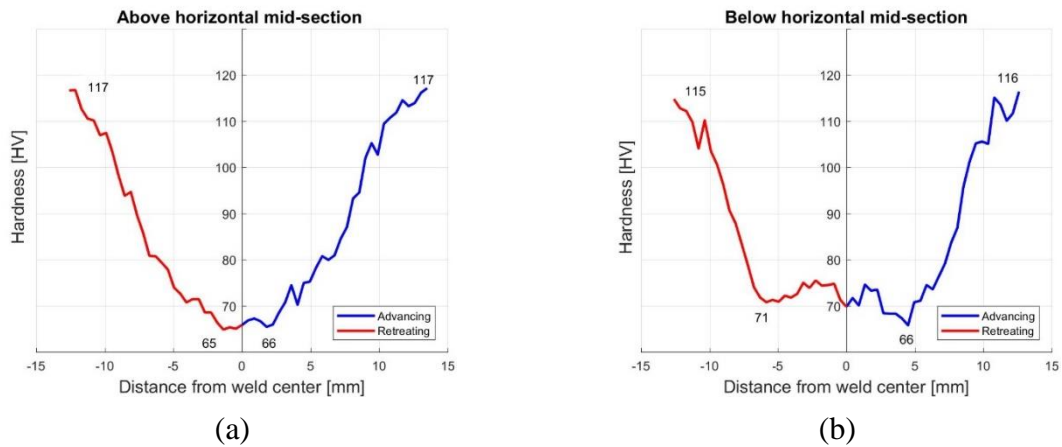


Figure 4.9 Displaced horizontal hardness profiles for the HYB joint. (a) Above mid-section and (b) below mid-section.

The resulting hardness profiles pertaining to the displaced vertical mid-section of the joint are shown in Figure 4.10. Measurements located on the RS of the joint are shown in Figure 4.10(a). The resulting hardness profile shows a similar pattern as the one in Figure 4.7. However, there is no significant hardness increase in the bottom region. The maximum and minimum hardness measured is 94 and 60 HV, respectively.

Figure 4.10(b) shows the corresponding hardness profile measured on the AS of the joint. Also in this case the profile reveals a pattern similar to that found in Figure 4.7. The maximum hardness value is 94 HV, while the minimum value is 61 HV. But in contrast to the situation in Figure 4.10(a), the root region displays a significant hardness increase, yielding a value of 80 HV.

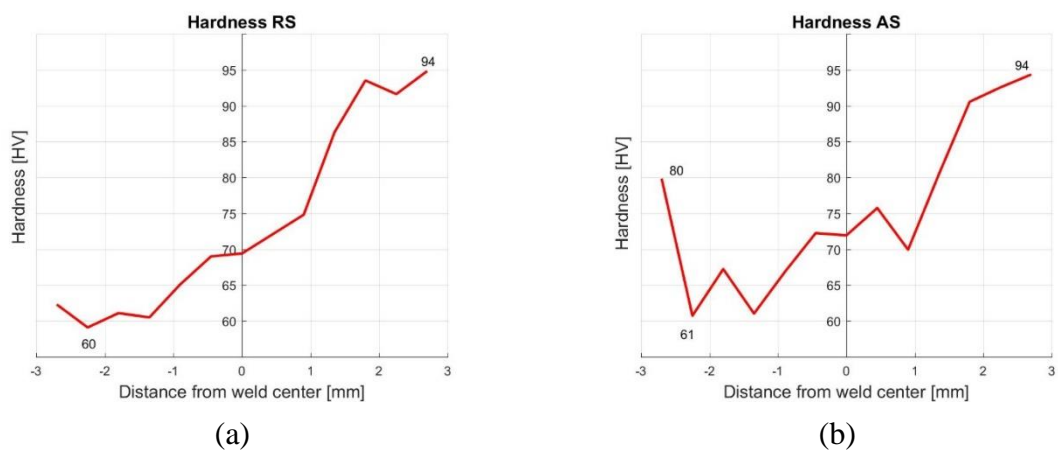


Figure 4.10 Displaced vertical hardness profiles for the HYB joint. (a) Displaced to the left (i.e. on the RS) and (b) displaced to the right (i.e. on the AS).

4.3 Tensile test results

As already explained in Section 3, the tensile specimens were taken from different locations in the welded plate, sampling both the base metal (BM), the extrusion zone (EZ) and the heat affected zone (HAZ). Macro-images of tested tensile specimens are presented in Figure 4.11, showing the fracture point in each of these zones.



Figure 4.11 Examples of macro-images of tested tensile specimens showing the fracture point in each of the zones.

A small reduction in thickness can be observed for all these specimens, but the thickness reduction is more evident for the EZ and HAZ tensile specimens. In the two latter cases, the fracture occurred a certain distance from the weld center-line, probably in the weakest part of the HAZ.

For all tensile specimens tested, fracture always occurred on the advancing side of the joint, regardless of the location of the HAZ (i.e. whether it is located on the AS or not). Additional macro-images of the fracture location are contained in Figure A 10 in the Appendix.

The measured stress-strain curves for the same tensile specimens are given in Figure 4.12. Additional stress-strain curves for all tensile specimens tested, including macro images of the specimens, can be found in Figure A 3 to Figure A 5 in the Appendix.

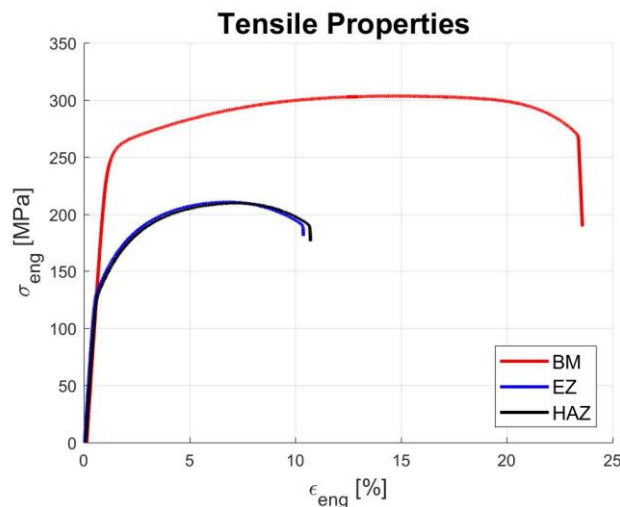


Figure 4.12 Example of measured stress-strain curves during tensile testing sampling different zones within the HYB joint.

As can be seen from Figure 4.12, there is a significant difference in the yield and work-hardening behaviour of the BM compared to the EZ and HAZ. Obviously, the extent of softening occurring during welding leads to large reduction in the local yield and tensile strengths of the joint as well as to extensive strain localization. This is similar to that observed in conventional GMA and FS welds.

Based on the stress-strain curves, the module of elasticity and the 0.2 % offset yield stress have been calculated. From these readings, the average module of elasticity was found to be approximately 68 GPa, which is close to the general accepted value of 70 GPa for aluminium. Calculated module of elasticity for all specimens can be found in Figure A 6 and Table A 7 in the Appendix.

The resulting offset yield stress for the same specimens are presented by the bar charts in Figure 4.13. Additional yield strength values for all tensile specimens tested can be found in Table A 8 in the Appendix.

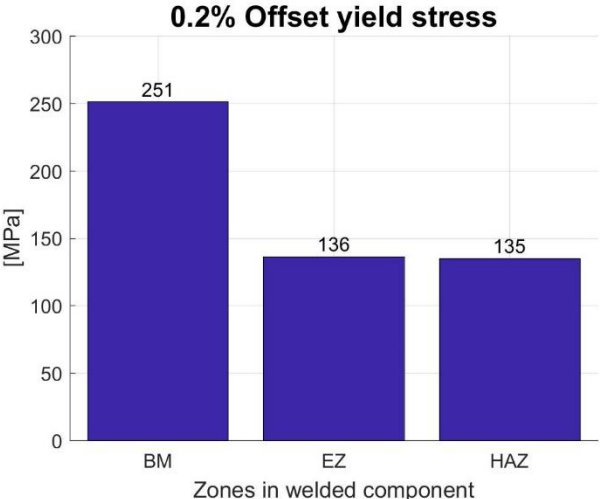


Figure 4.13 Measured stress at offset yield for selected tensile specimens sampling different zones within the HYB joint.

As can be seen from Figure 4.13, the BM starts to yield at approximately 250 MPa. This value is much higher compared to the EZ and the HAZ, where yielding starts at 136 and 135 MPa, respectively. Hence, there is apparently no difference in the yield stress between the EZ and the HAZ.

The corresponding data for the tensile strength are presented in Figure 4.14. Additional tensile strength values for all tensile specimens tested can be found in Table A 8 in the Appendix.

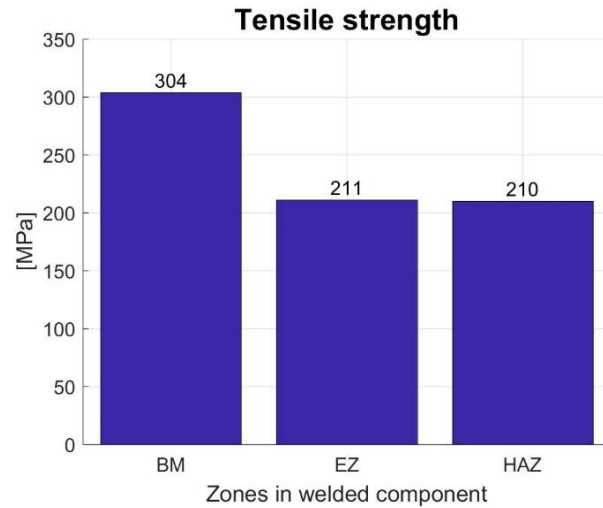


Figure 4.14 Measured tensile strength for selected tensile test specimens sampling different zones within the HYB joint.

As can be seen from the bar charts, the BM reaches a tensile strength of 304 MPa before fracture occurs. In contrast, the EZ and the HAZ display significantly lower values i.e. 211 and 210 MPa, respectively.

The measured strain at fracture for the same tensile specimens as before are presented in Figure 4.15. Additional values for the fracture strain for all tensile specimens tested can be found in Table A 9 in the Appendix.

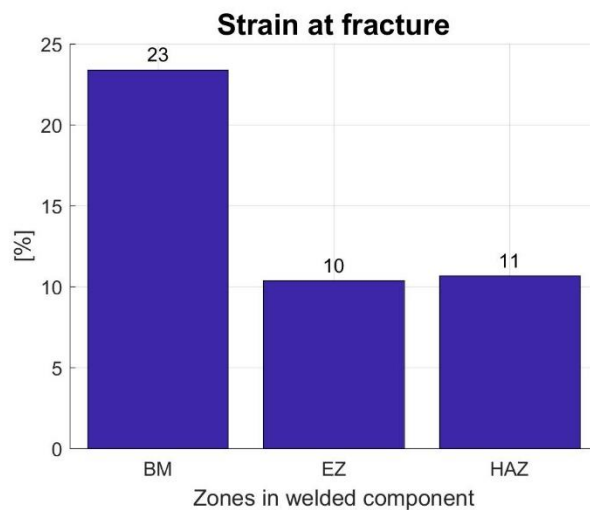


Figure 4.15 Measured strain at fracture for selected tensile specimens sampling different zones within the HYB joint.

It is evident from the above figure that the BM reaches a much higher fracture strain compared to the EZ and the HAZ. The difference is typically a factor of 2.

Also, the reduction in area (RA) after fracture has been calculated, based on the following relationship [27]:

$$\%RA = \frac{A_0 - A_f}{A_0} \cdot 100 \quad (4.1)$$

where A_0 is the initial cross-sectional area and A_f is the corresponding cross-sectional area at fracture, as defined in Figure 4.16. All calculated RA values can be found in Table A 10 in the Appendix.

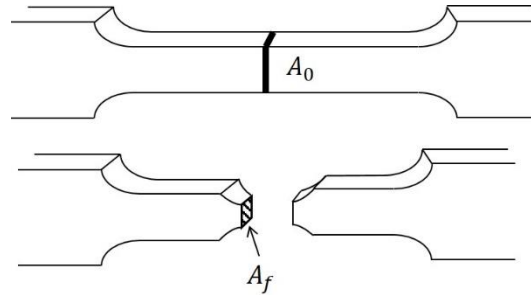


Figure 4.16 Sketch showing the initial cross-sectional area A_0 prior testing and the reduced cross-sectional area A_f at the point of fracture.

Figure 4.17 shows a graphical representation of the calculated reduction in area for the same tensile specimens as before. As expected, the total reduction in cross-sectional area is seen to be higher for the BM compared to the EZ and HAZ specimens. This observation is consistent with that shown previously in Figure 4.15, indicating that the base metal has a higher ductility compared to the HYB joint.

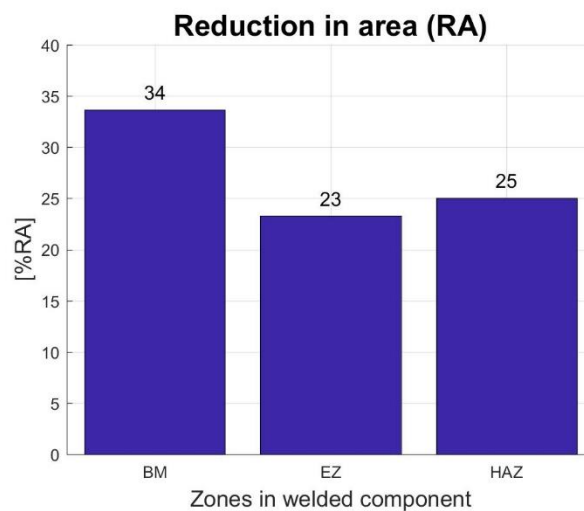


Figure 4.17 Calculated RA-values for selected tensile specimens sampling different zones within the HYB joint.

4.4 Fractography of tensile specimens

In the following, the main results from the fractographic examination of selected tensile specimens will be presented. In this overview, only one side of the fracture surface will be viewed. Additional SEM images of the opposite fracture surfaces can be found in Figure A 7 to Figure A 9 in the Appendix.

Micrographs of the base material fracture surface at low and high magnification are shown in Figure 4.18. At low magnification, the fracture surface is fairly rough with a noticeable topography, as seen from Figure 4.18(a). At high magnification, large dimples are observed (5 to 10 μm in diameter), with smaller ones ($<5 \mu\text{m}$) in-between, as shown in Figure 4.18(b). This is typically of a ductile fracture.

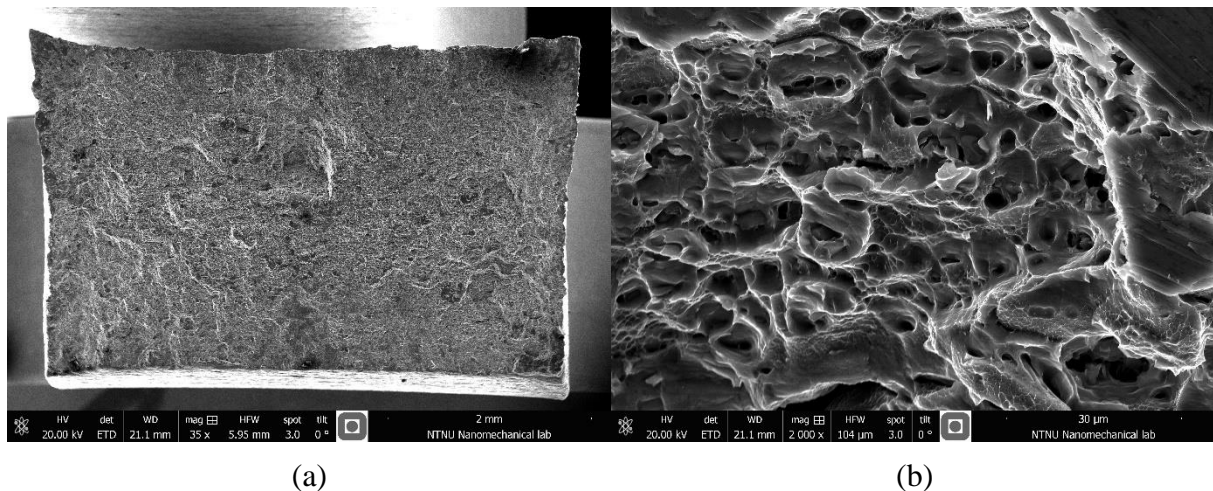
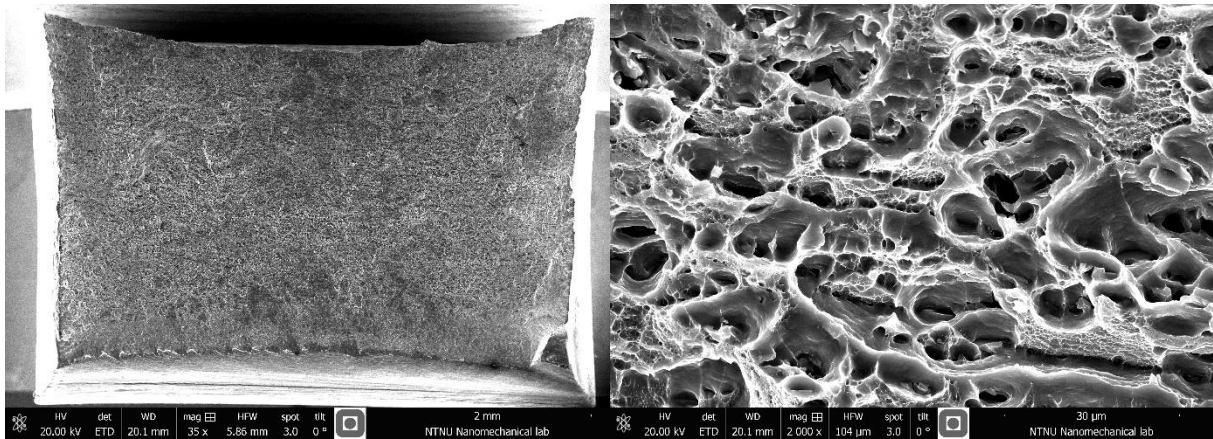


Figure 4.18 SEM micrographs showing the fracture surface appearance of the base material. (a) Overview at low magnification and (b) close-up of the center at high magnification.

Figure 4.19 shows micrographs of the EZ fracture surface at low and high magnification, respectively. At low magnification, Figure 4.19(a), the fracture surface appears to be quite smooth compared to the base material. At higher magnification, it is evident that the fracture surface is covered by a high density of different sized dimples. Most prominent are the large dimples, but smaller dimples ($<5 \mu\text{m}$) are also present in-between (Figure 4.19b). In addition, some areas with shallow cup formed voids can be observed.

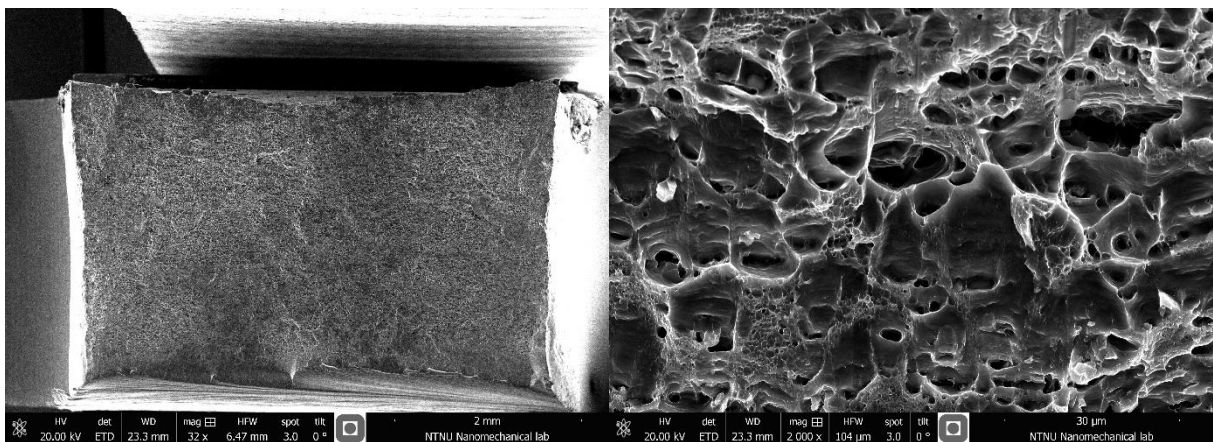


(a)

(b)

Figure 4.19 SEM micrographs showing the fracture surface appearance of the extrusion zone. (a) Overview at low magnification and (b) close-up of the center at high magnification.

Finally, micrographs of the HAZ fracture surface at low and high magnification are shown in Figure 4.20. At low magnification, Figure 4.20(a), the fracture surface looks fairly similar to that of the EZ. But at higher magnification, Figure 4.20(b), more elongated dimples can also be observed in the lower part of the image. In general, the number density of dimples appears to be smaller compared to that of the BM and EZ fracture surfaces.



(a)

(b)

Figure 4.20 SEM micrographs showing the HAZ fracture surface appearance. (a) Overview at low magnification and (b) close-up of the center at high magnification.

Based on the fracture surface observations it may be concluded that all tensile test specimens fail because of a ductile development and not owing to “lack of bonding” due to possible “kissing” bond formation. This is reassuring.

4.5 Charpy V-notch test results

Macro-images of broken Charpy V-notch specimens are shown in Figure 4.21. They sample different regions of the joint, i.e. the base material (BM), the extrusion zone (EZ), the bond line (BL) and the HAZ.

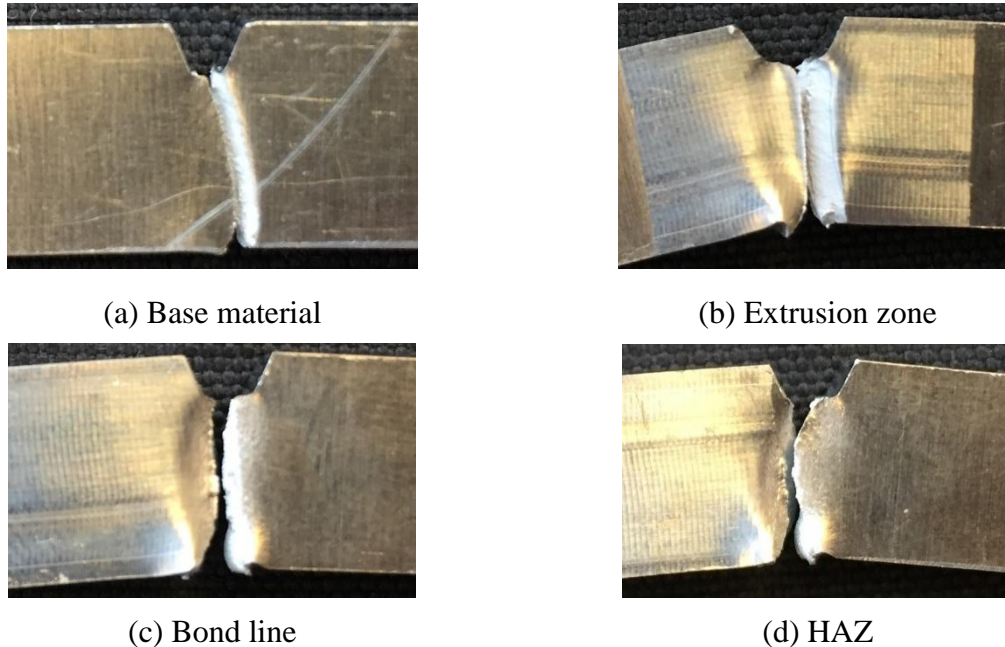


Figure 4.21 Macro-images of broken Charpy V-notch specimens sampling different zones within the HYB joint.

On a macro-scale level, all Charpy V-notch specimens show a similar fracture behaviour in that they reveal a cup-and-coin type of fracture. Still, there are some individual differences in the fracture mode. The fracture of the BM follows a slightly curved path, with little evidence of plastic deformation, as seen from Figure 4.21(a).

In contrast, the EZ reveals a more ductile type of fracture with extensive plastic deformation, particularly in the lower region of the specimen. The fracture path follows a relatively straight line from the edge of the notch, as seen from Figure 4.21(b). Also, the BL and HAZ specimens reveal a ductile fracture behaviour with extensive plastic deformation, as shown in Figure 4.21(c) and Figure 4.21(d).

The measured energy absorption of the same Charpy V-notch specimens are graphically presented in Figure 4.22. Additional values for the measured energy absorption for all Charpy V-notch specimens tested can be found in Table A 11 in the Appendix.

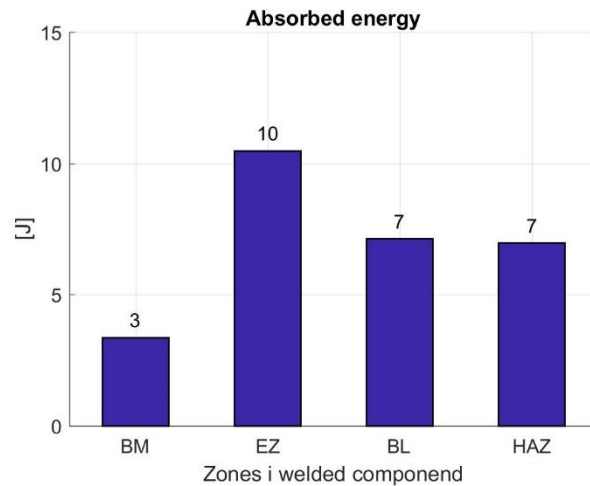


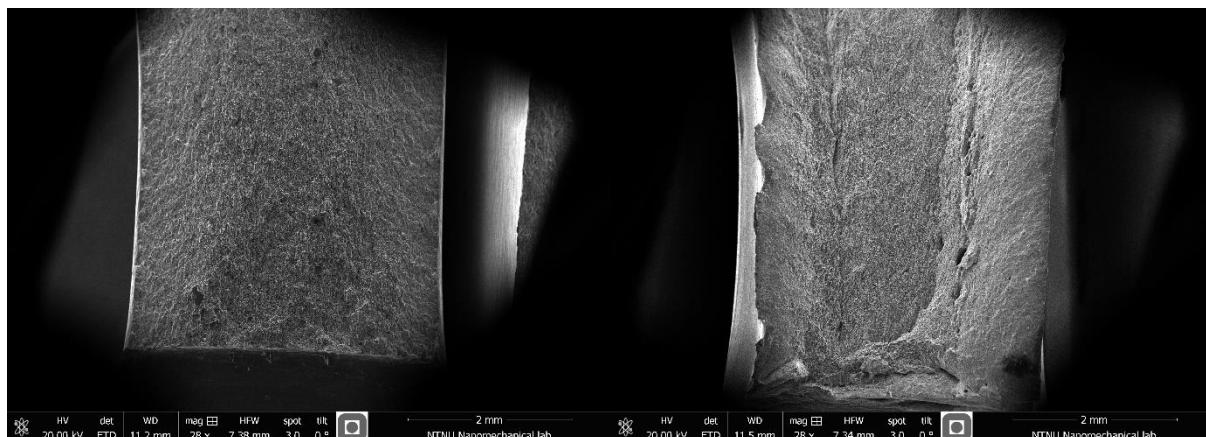
Figure 4.22 Measured energy absorption for selected Charpy V-notch specimens sampling different zones within the HYB joint.

It follows from the above figure that the different weld zones absorb significantly more energy compared to the BM (typically a factor between 2 and 3). Therefore, the impact toughness of the HYB joint is not critical in the sense that it becomes a limiting factor in mechanical design.

4.6 Fractography of Charpy V-notch specimens

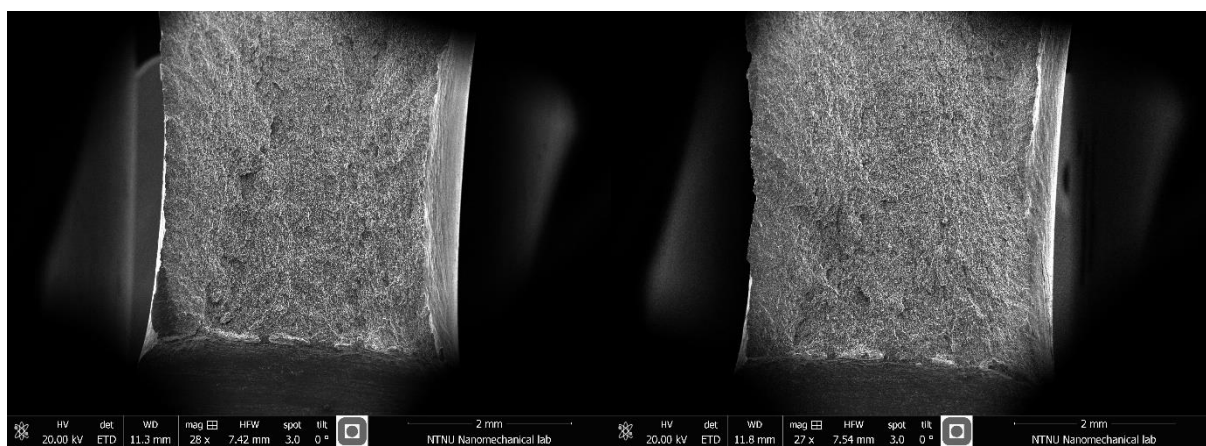
In the following, the main results from the fractographic examination of the broken Charpy specimens will be presented. In this overview, only one side of the fracture surface will be viewed. Additional fractographs of the opposite side can be found in Figure A 11 to Figure A 13 in the Appendix.

Figure 4.23 shows the fracture surface appearance of the broken Charpy V-notch specimens sampling different regions of the joint. In these fractographs, the V-notch is located in the bottom part of the image. Thus, the crack propagates from the bottom to the top.



(a) Base material

(b) Extrusion zone

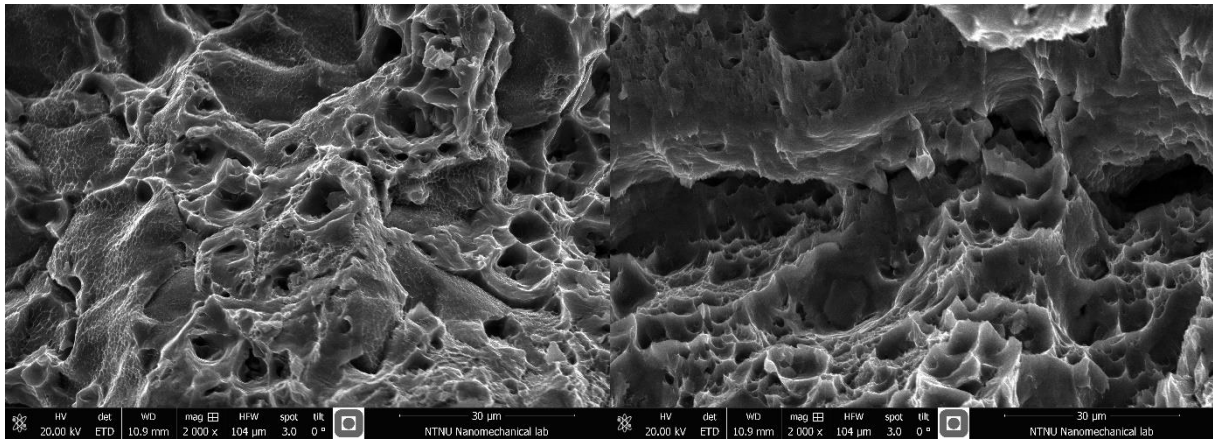


(c) Bond line

(d) HAZ

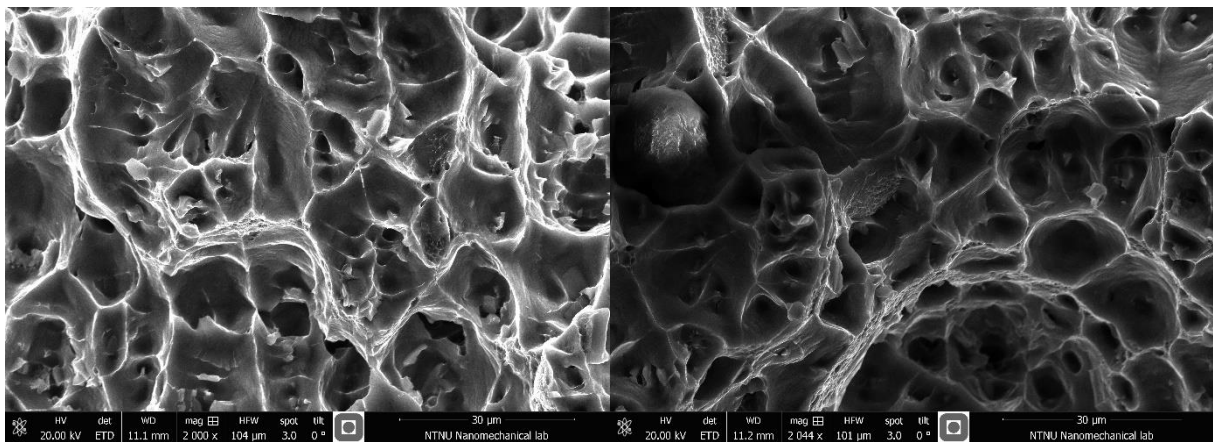
Figure 4.23 SEM micrographs of the fracture surface appearance of broken Charpy V-notch specimens sampling different zones within the HYB joint at low magnification. Crack propagation path - from bottom to top. (The scale bar in lower right corner is 2 mm).

The base material, Figure 4.23(a), shows a fairly smooth fracture surface, with very little evidence of macroscopic plastic deformation. In contrast, the EZ reveals a fracture surface with noticeable change in the topography across the surface, as seen from Figure 4.23(b). In the lower region, where the crack has propagated, some sign of cracking normal to main crack direction is observed. Considering the BL and HAZ specimens, Figure 4.23(c) and Figure 4.23(d), the macroscopic fracture appearance is more similar to that of the base material. Still, the extent of macroscopic deformation is larger compared to that observed for the base material. Micrographs of the fracture surface close to the notch at high magnification are shown in Figure 4.24.



(a) Base material

(b) Extrusion zone



(c) Bond line

(d) HAZ

Figure 4.24 SEM micrographs at high magnification, showing the fracture surface appearance close to the Charpy V-notch at different locations within the HYB joint. (The scale bar in the lower right corner is 30 μm).

It follows from Figure 4.24(a), that the BM fracture surface contains both large and small dimples together with intergranular facets with a high number density of small dimples. In contrast, the EZ fracture surface contains much smaller dimples, as seen from Figure 4.24(b). The BL and HAZ reveal a similar type of fracture behaviour, as the fracture surfaces tend to be covered by relatively large shallow dimples. But, in-between the large dimples, also smaller ones are located, as shown in Figure 4.24(c) and Figure 4.24(d).

Finally, micrographs of the fracture surface in the center of the same Charpy V-notch specimens are shown in Figure 4.25.

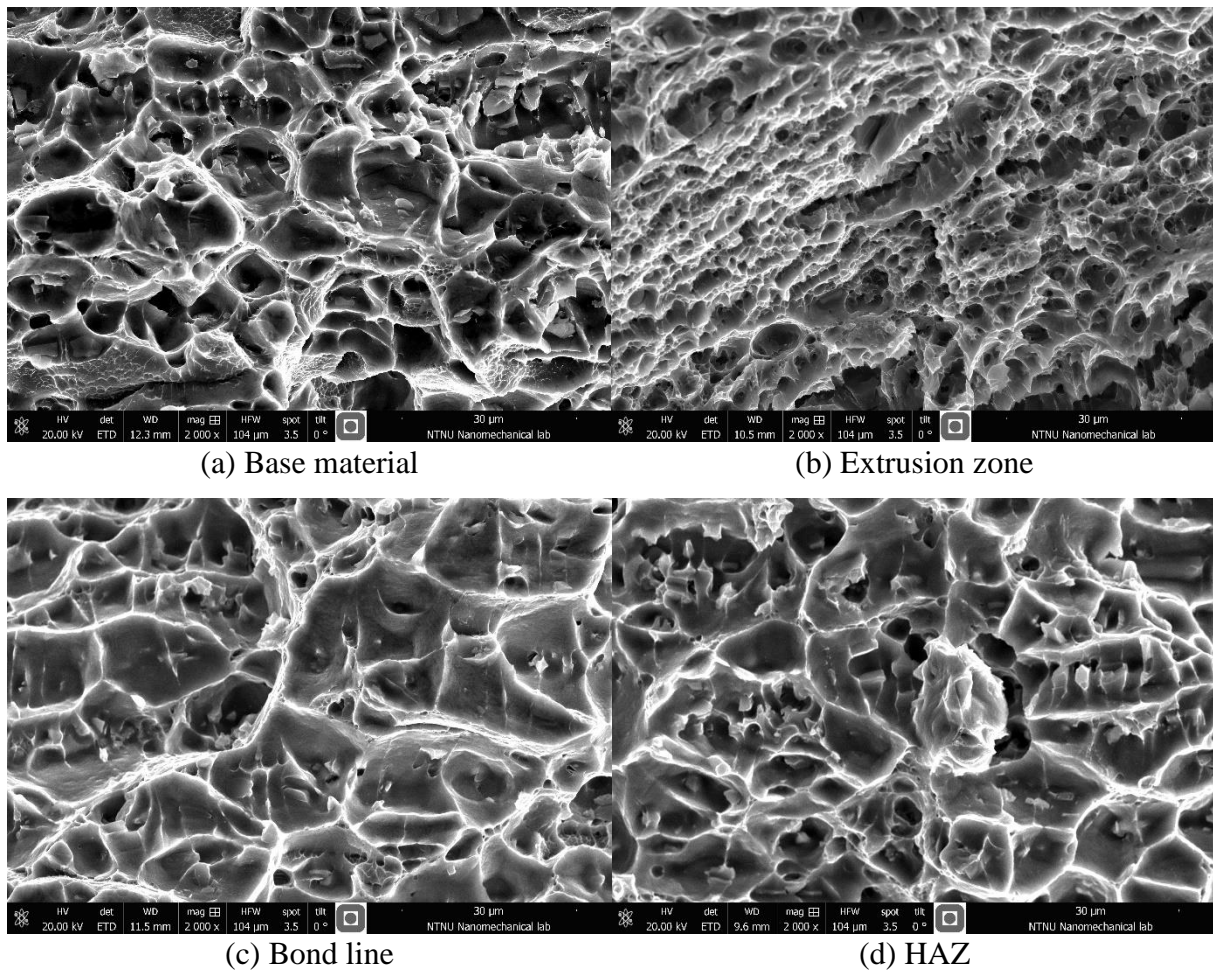


Figure 4.25 SEM micrographs at high magnification, showing the fracture surface appearance in the center the Charpy-V notch specimens at different locations within the HYB joint. (The scale bar in the lower right corner is 30 μm).

Considering the BM specimen, the fracture surface is covered by relatively large dimples, with smaller ones in-between. Some evidence of microvoid coalescence is observed in the lower region. In contrast, the EZ specimen contains a high number density of small dimples with some medium sized dimples in-between. In addition, some microcracks can be observed. Moreover, it follows from Figure 4.25(c) and Figure 4.25(d) that the BL and HAZ Charpy V-notch specimens reveal a similar fracture surface appearance, i.e. large shallow voids with small dimples in-between.

Again, based on the fracture surface appearance of the broken Charpy V-notch specimens it may be concluded that the impact toughness of the HYB joint is not critical from an engineering design point of view in the sense that it reduces the mechanical integrity of the component.

5 Discussion

5.1 Introductory remarks

In the following, a comparison of the mechanical properties of the different GMA, FS and HYB weldments will be performed. Note that all reference data for GMAW and FSW are taken from the master thesis of Breivik [38]. She used 3 mm AA6082-T6 extruded profiles as a basis for her GMA and FS welding trials, whereas 4 mm AA6082-T6 rolled plates were used in the HYB case. This means that the comparison is encumbered with some degree of uncertainty.

5.2 Effect of base material chemical composition and processing conditions

Figure 5.1 shows the difference in the main alloying elements (i.e. Mg and Si) between the two base materials. As can be seen from the figure, the base material used for GMAW and FSW exhibit a slightly higher Si content compared to the base material used for HYB welding. Besides that, their overall chemistry is seen to be quite similar.

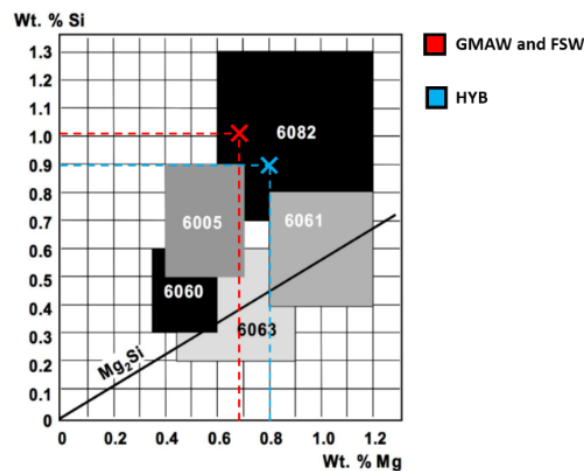


Figure 5.1 Difference in the main alloying elements (i.e. Mg and Si) between the two base materials used for GMA, FS and HYB joining.

Obviously, the pertinent differences in BM processing condition are much more important, as extrusion and rolling may give rise to highly different microstructures and crystallographic textures. Still, it is believed that such differences will not compromise the forthcoming benchmarking of the HYB process against GMAW and FSW.

5.3 Summary of assembled flow curves

Figure 5.2 shows a comparison of the measured stress-strain curves for selected GMAW, FSW and HYB tensile specimens sampling different zones within the weldments.

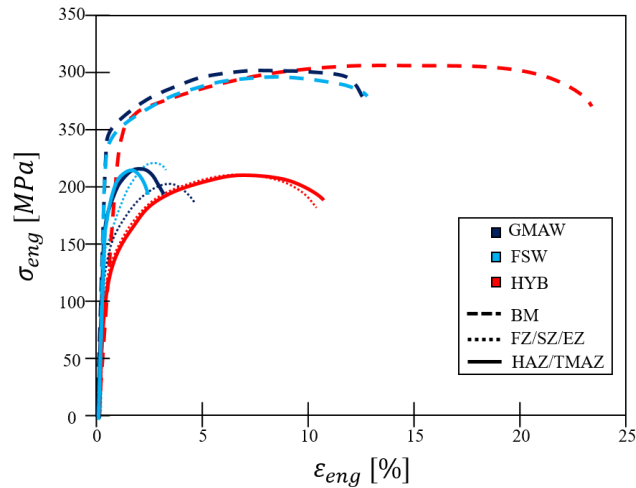


Figure 5.2 Comparison of measured stress-strain curves for selected GMAW, FSW and HYB tensile specimens.

As can be seen from the figure, the base metal flow curves look reasonable similar, indicating that the pertinent differences in the processing and experimental conditions are not that critical after all as far as the tensile properties are concerned. An exception is the fracture strain, which is seen to be much higher for the rolled plates used in the HYB joining trials compared to the extruded profiles. This difference is also reflected upon in the measured stress-strain curves sampling the properties of the local weld zones. Therefore, when it comes to ductility and toughness, there will probably be an additional effect of the base metal microstructure and texture, which will interfere with the contribution from welding on the measured values. As a result, normalizing of the data is necessary before a comparison can be made.

5.4 Comparison of mechanical properties of the different GMA, FS and HYB weldments

5.4.1 Mechanical strength

In the following, both the offset yield and the tensile strengths being achieved for each of the three welding techniques will be compared. Note that all presented values represent the arithmetic means of the reported data for the different weld zones. The error bars in the graph represent the standard deviation of the measurements.

The average yield strengths of different weld regions are shown in Figure 5.3. As can be seen from the figure, a small deviation is found for the BM yield strengths. This may be a result of the pertinent difference in the base material processing conditions, as discussed earlier.

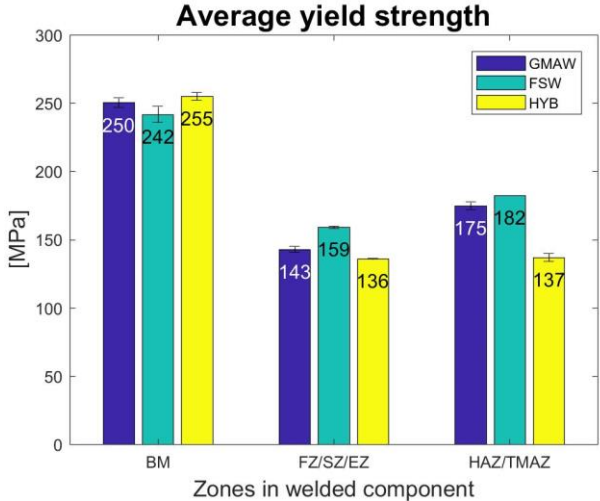


Figure 5.3 Comparison of the average offset yield strengths for the GMAW, FSW and HYB tensile specimens.

When it comes to the different weld zones, a significant reduction in strength is observed for all welding techniques. For the GMA and FS joints, the strength reduction relative to the BM is approximately 43% and 34%, respectively, while in the HYB joint a reduction of 47 % is achieved. Hence, the HYB joint reveals a yield strength which is comparable with that of the GMA weld, but significant lower than the FS weld.

Moreover, the bar chart in Figure 5.4 shows a similar comparison of the average tensile strengths of the GMA, FS and HYB weldments. Also in this case, a significant reduction in the HAZ tensile strength is observed. It follows that the strength reduction is 30 and 24 % in the GMA and FS welds, respectively and 32 % for the HYB joint. Again, this means that the observed HYB tensile strength reduction is comparable to that of the GMA weld.

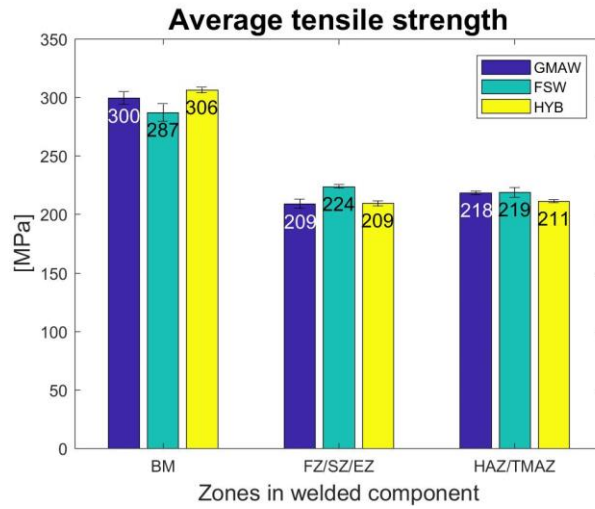


Figure 5.4 Comparison of the average tensile strengths for the GMAW, FSW and HYB tensile specimens.

Based on the yield and tensile strength data presented above, the strain-hardening potential of the different weld regions has been calculated. The strain-hardening potential is defined as the ratio of the tensile strength to the yield strength, and is a measure of the maximum work hardening that the material can undergo during plastic deformation. In other words, it is a measure of the margin of safety against failure by plastic collapse [54, 55].

The strain-hardening potential for the GMAW, FSW and HYB tensile specimens are graphically presented in Figure 5.5. As can be seen from the figure, there is no large difference in strain-hardening potential between the different welding techniques. Still, the HYB joint shows slightly higher values in the two weld regions compared to the GMA and the FS welds.

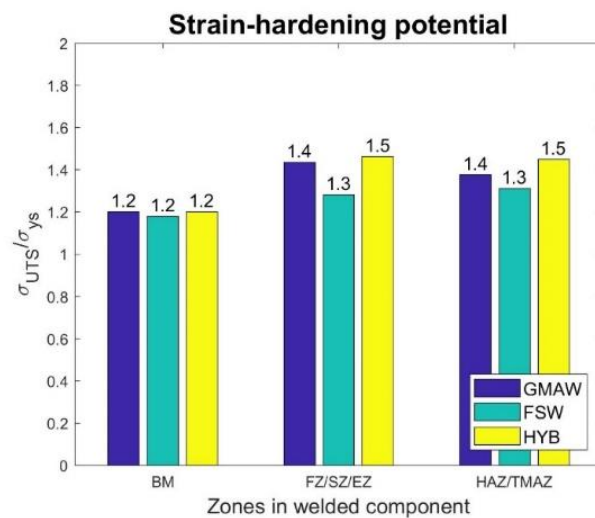


Figure 5.5 Calculated strain-hardening potential for different zones in the GMA, FS and HYB weldments.

5.4.2 Ductility

The ductility of a material is commonly represented by the engineering strain at fracture and the reduced cross-section area of the tensile specimens. In the following, a comparison of the ductility will be presented. Note again that all presented values are the arithmetic mean of the reported data for the different weld zones. The error bars represent the standard deviation of the measurements.

Figure 5.6 shows a comparison of the measured fracture strains for the GMA, FS and HYB joints. Due to the pertinent differences in the BM ductilities, the values are normalized so that they instead show the percentage reduction in fracture strain relative to the BM.

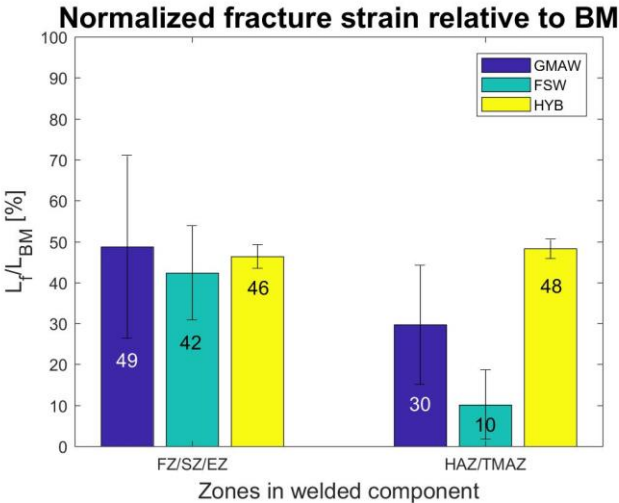


Figure 5.6 Comparison of the percentage reduction in the fracture strain relative to the base material for the GMAW, FSW and HYB tensile specimens.

As can be seen from Figure 5.6, small differences in the local fracture strain are observed for the tensile specimens located close to the weld center (FZ/SZ/EZ). Larger variations are observed for the HAZ specimens. In addition, the GMAW and FSW specimens show a relatively large standard deviation compared to the HYB specimens, indicating that the uncertainty is greater for these values. In general, the fracture strain for the HYB tensile specimens is closer to the value obtained for the base material than that observed for the other two welding techniques.

The average reduction in the cross-sectional area for the different weld zones in the GMA, FS and HYB weldments are graphically presented in Figure 5.7. It follows that the reduction in area is the most accurate measure of ductility, because it considers the material contraction in two directions.

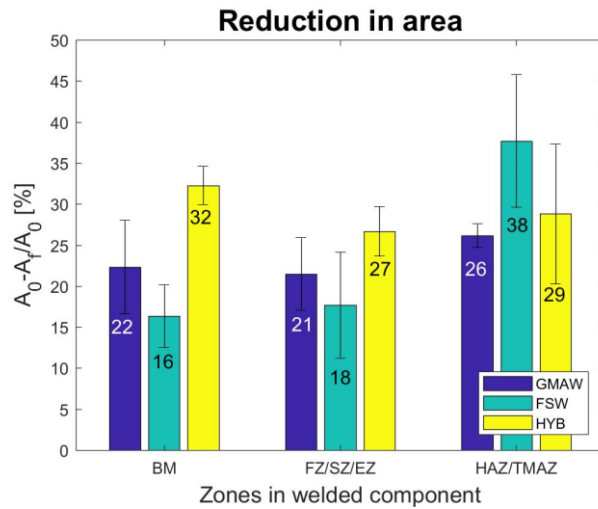


Figure 5.7 Comparison of the average reduction in area for the GMAW, FSW and HYB tensile specimens.

As expected, large differences in the area reduction are observed for all tensile specimens. Also, relatively large standard deviations are observed for the same specimens.

By using the average values from Figure 5.7 as a basis for comparison, the percentage reduction in area relative to the BM for the GMAW, FSW and HYB tensile specimens can be calculated. The results are shown graphically in Figure 5.8. It follows that bars falling on the positive side of the zero base line indicate an increase in the area reduction compared to the base material, while bars falling on the opposite side indicates a reduction. As can be seen from the figure, a significant increase in the area of reduction relative the BM is observed for the FSW specimen located in the HAZ/TMAZ, showing that a low fracture strain, as previously indicated in Figure 5.6 for the same tensile specimens, is not necessarily a sign of low ductility.

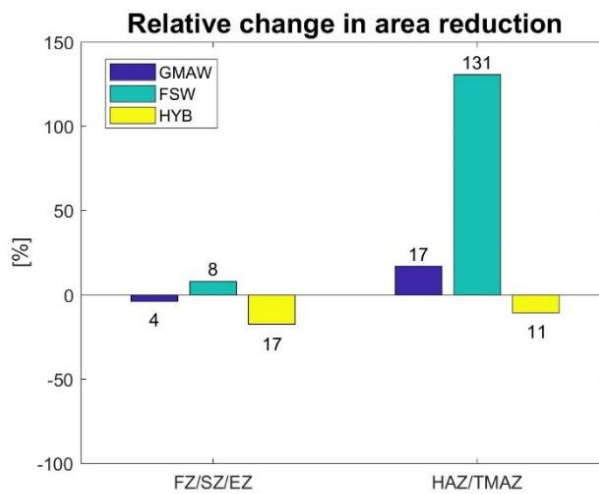


Figure 5.8 Calculated change in the cross-sectional area reduction relative the base material for the same set of tensile specimens included in Figure 5.7.

5.4.3 Impact toughness

In the following, a comparison of the measured energy absorption for different local zones in the GMA, FS and HYB weldments are presented. Due to the pertinent differences in the specimen thickness, the energy absorption per unit thickness is used as a basis for the comparison (designated K_{CV}). In this case the initial cross-sectional area is measured from the edge of the notch in full plate thickness, as illustrated in Figure 5.9.

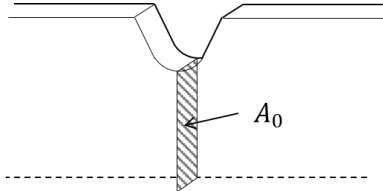


Figure 5.9 Definition of the initial cross-sectional area of a Charpy V-notch specimen used to calculate the normalized energy absorption.

Note that the initial cross-sectional area for the GMAW and FSW Charpy V-notch specimens was not specified by Breivik [38]. Therefore, the nominal cross-sectional area was calculated based on the initial cross-sectional area of the tensile specimens, assuming that machining of the Charpy V-notch specimens was done in a similar way. From this, an effective plate thickness of approximately 2.6 mm was calculated.

The normalized energy absorption of the GMAW, FSW and HYB specimens, sampling the BM and HAZ/TMAZ, are presented by the bar charts in Figure 5.10. In this case the average energy absorption per unit area is seen to be higher for the GMA and FS welds compared to the HYB weld. The reason for this is not obvious, but may reflect the previously noted differences in the base metal ductility and impact toughness.

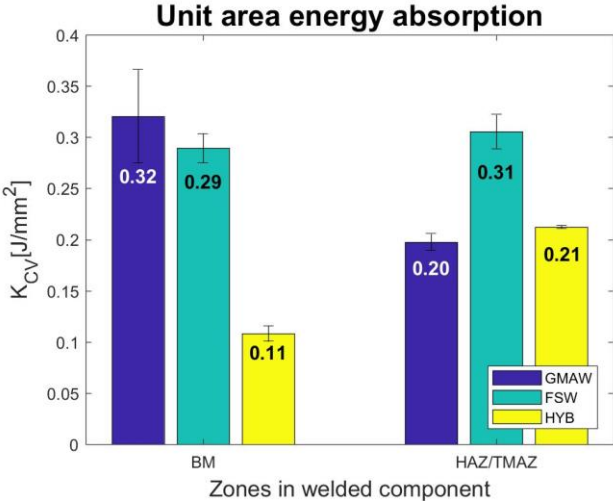


Figure 5.10 Comparison of the average energy absorption per unit area for the GMAW, FSW and HYB Charpy V-notch specimens, sampling different zones in the weldments.

Finally, the average energy absorption for the GMAW, FSW and HYB Charpy specimens relative to the base material is graphically presented in Figure 5.11. It follows that bars falling on the positive side of the zero base line indicate an increase in the energy absorption compared to the base material, while bars falling on the negative side indicate a reduction. From this figure, it is evident that the HYB specimen absorbs significantly more energy compared to the GMAW and FSW specimens when the pertinent differences in the BM impact toughness are properly accounted for.

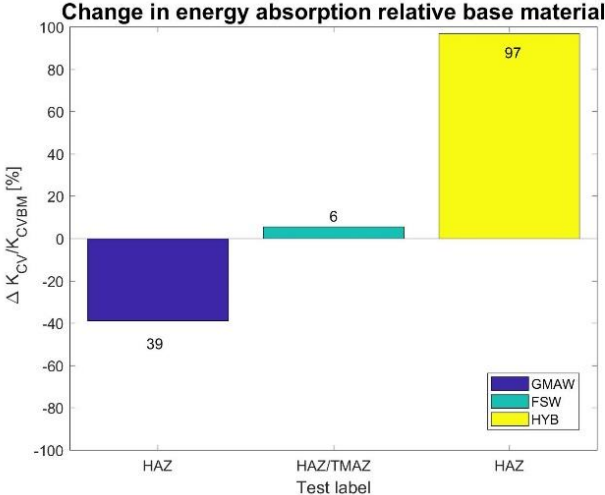


Figure 5.11 Calculated change in energy absorption relative to the base material for the GMAW, FSW and HYB Charpy V-notch specimens included in Figure 5.10.

5.4.4 Overall mechanical performance

The overall mechanical performance of the GMA, FS and HYB joints is summarized in Table 5.1. The presented values consider the increase/reduction in performance of the weakest part of the joints relative to the base material. Note that red values indicate a reduction in performance, while blue values indicate an increase.

Table 5.1 Summary of the reduction/increase in mechanical properties of the different weld samples included in the analysis.

Reduction/increase (%)	Welding technique		
	GMAW	FSW	HYB
Yield strength	43	34	47
Tensile strength	30	24	32
Strain at fracture	49	42	46
Reduction in area	4	8	17
Energy absorption	39	6	97

As can be seen from the above table, the HYB joint performance lies close to that of the GMAW joint. Still, the weld performance is not as good as that of the FS weld, which scores best on nearly all check-points. Therefore, it is a great potential for further optimization of the HYB process in order to bring the method to the forefront of aluminium welding technology.

5.5 Comparison of hardness profiles

A comparison of the measured GMAW, FSW and HYB hardness profiles are shown in Figure 5.12. In the figures, the shaded grey areas indicate the total HAZ width.

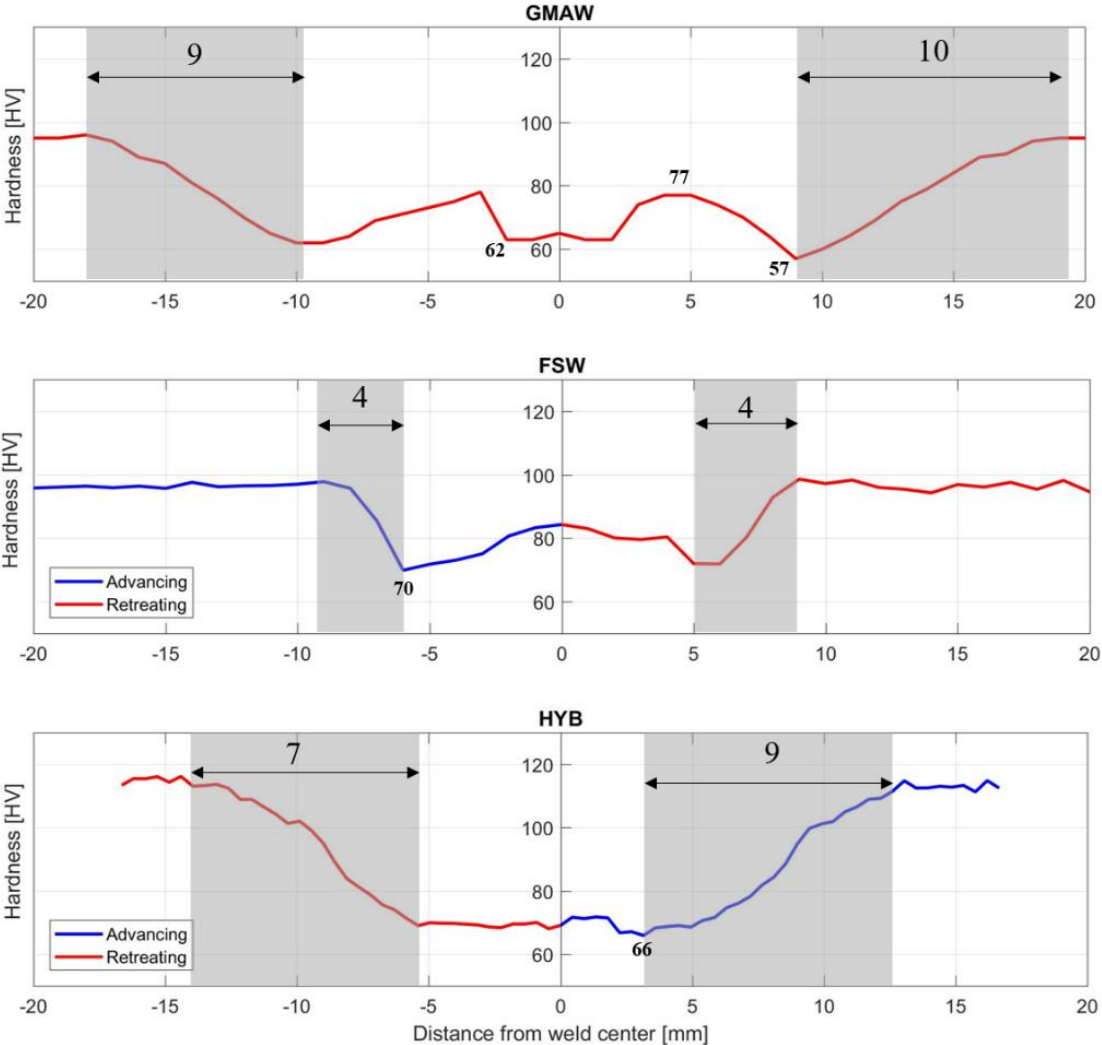


Figure 5.12 Comparison of measured hardness profiles for the GMA, FS and HYB joints.

As can be seen from the above figure, the total width of the reduced strength zone is significantly smaller for the FS joint compared to the GMA and HYB joints. Also, significant differences in the HAZ width can be observed, where FSW provides the smallest zone width.

5.6 Relationship between hardness profile and yield strength

A macro-image of the HYB tensile specimen subsequent to joining is shown in Figure 5.13, where the fracture location relative to the joint center-line is highlighted.

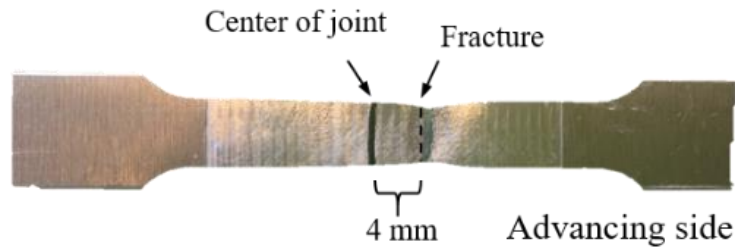


Figure 5.13 Macro-image of a HYB tensile specimen showing the location of the fracture on the advancing side relative to the joint center.

In the HYB case fracture occurs approximately 4 mm from the joint center on the AS. This corresponds well with observations made from the hardness profile, where the minimum hardness is found in HAZ on the AS of the joint. As matter of fact, this is true for all of the tested HYB tensile specimens, regardless of their location within the weld region. Additional images of the fracture location for all HYB tensile specimens can be found in Figure A 10 in the Appendix. Also for the GMA and FS welds examined by Breivik the location of fracture seems to correspond well with the weakest point in the weld HAZ [38].

Because of the correlation between hardness and yield strength, the resulting yield strength profile for the different welding techniques can be calculated based on Equation (2.3) and the previously presented experimental hardness profiles. The results are shown in Figure 5.14. For the benefit of the reader values for the base material yield strength σ_b and minimum HAZ yield strength σ_{min} are included in the figures. Moreover, in the HYB graph the calculated base metal yield strength (based on the individual hardness measurements) are also included and represented by a dotted line. In addition, all calculated values for the HYB yield stress profile can be found in Table A 13 in the Appendix.

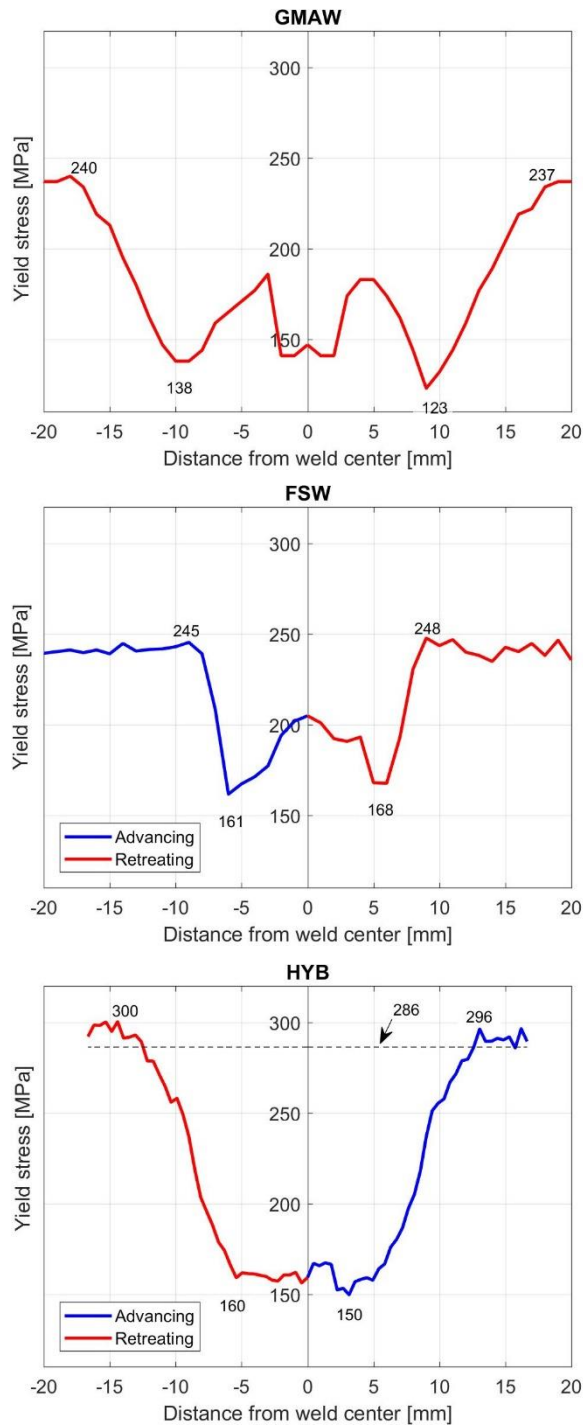


Figure 5.14 Calculated yield strength profiles based on Equation (2.3) and the measured GMAW, FSW and HYB hardness profiles.

The average yield strength values for the base materials σ_b and minimum HAZ yield strength values σ_{min} , as read from the yield strength profiles, are summarized in Table 5.2 and compared with those measurements by tensile testing.

Table 5.2 Summary of key yield strength data for the GMA, FS and HYB joints.

	Yield stress (MPa)			
	From yield stress profile		From tensile testing	
	σ_b	σ_{min}	σ_b	σ_{min}
GMAW	239	131	250	143
FSW	247	165	242	159
HYB	286	155	255	136

As can be seen from the table, the calculated σ_b and σ_{min} values based on the GMAW and FSW hardness profiles correspond well with those measured from tensile testing. In contrast, the calculated σ_b and σ_{min} values based on the HYB hardness profile show significantly larger deviations from the measured ones. The reason for this discrepancy is not known, but it may have to do with the fact that the equation used for calculating the yield strength profiles is originally developed for extruded plates and profiles and not for rolled plates, which have a different microstructure and crystallographic texture.

Still, there is a fair agreement between the calculated and measured strength reduction for all three welding processes, as illustrated by the data presented in Table 5.3.

Table 5.3 Summary of calculated and measured strength reductions based on hardness and tensile testing, respectively.

	Strength reduction (%)	
	From yield stress profile	From tensile testing
GMAW	45	43
FSW	33	34
HYB	46	47

5.7 Load-bearing capacity of the GMA, FS and HYB weldments

5.7.1 General

In the following, the load-bearing capacity of the GMA, FS and HYB joints will be evaluated. As stated in the previous Section 5.4, HAZ softening is observed for all three joining techniques and need to be taken into consideration in engineering design. In this case, both the total width of the reduced strength zone and the corresponding minimum strength level within the HAZ are of importance and must be allowed for, as discussed previously in Section 5.6.

5.7.2 Loading perpendicular to the joint

In the case of a perpendicular loading situation, as shown in Figure 2.35(a), the load-bearing capacity can be calculated on the basis of the minimum HAZ yield strength level σ_{min} , as measured from tensile testing (presented in Table 5.2).

The relative increase in the cross-sectional area ($\Delta A/A$) required to maintain the load-bearing capacity of the joint after HAZ softening can then be calculated from the following equation [50]:

$$\frac{\Delta A}{A} = \frac{\sigma_b}{\sigma_{min}} - 1 \quad (5.1)$$

By inserting the tensile test data for σ_b and σ_{min} from Table 5.2 into Equation (5.1), a necessary increase in the cross-sectional area of 88 % is calculated in the HYB joint. For the GMA and FS welds the corresponding values are 75 and 52 %, respectively.

5.7.3 Loading parallel to the joint

In order to evaluate the load-bearing capacity of the joints under such conditions, the equivalent half width of the reduced strength zone y_{red}^{eq} , of minimum strength σ_{min} must first be calculated by solving the integral in Equation (2.7), using input data from the yield strength profiles in Figure 5.15.

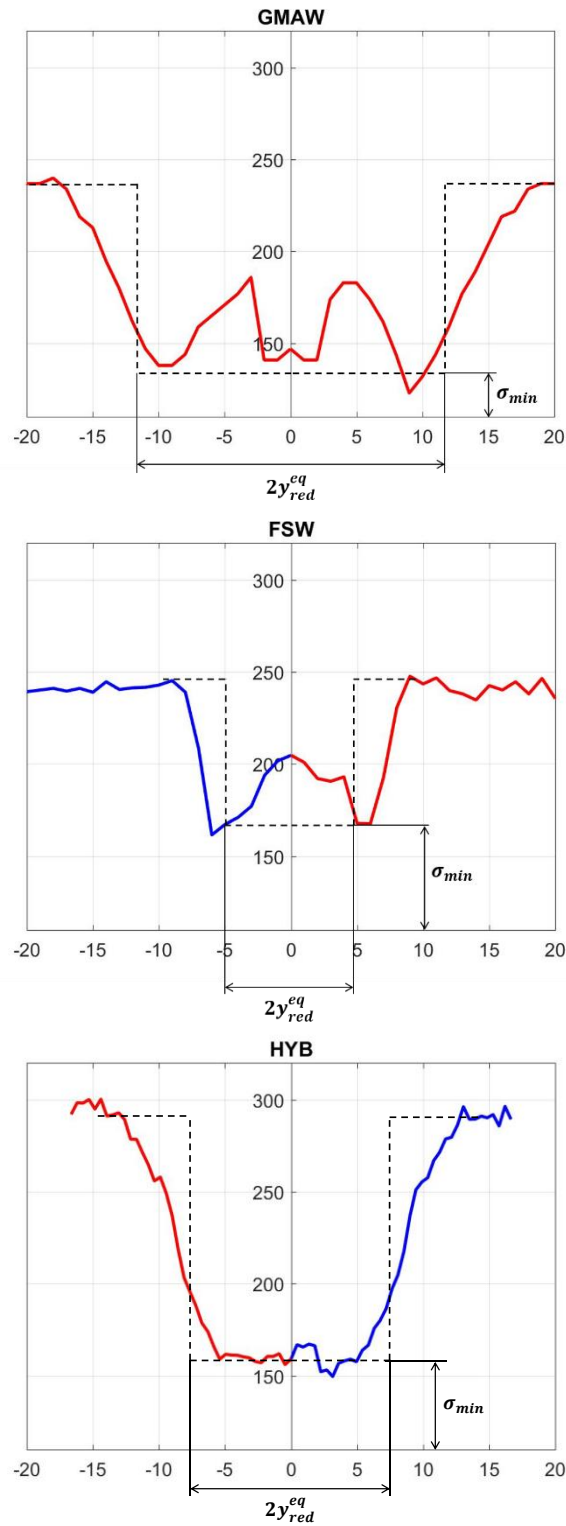


Figure 5.15 Determination of the equivalent half width of the reduced strength zone y_{red}^{eq} of minimum strength σ_{min} based on the calculated yield stress profiles for the GMA, FS and HYB joints.

Then, it follows from the treatment of Myhr and Grong [50] that the relative increase in the cross-section of the component ($\Delta A/A$) to compensate for the associated strength loss is given by the following relationship:

$$\frac{\Delta A}{A} = \frac{2y_{red}^{eq} \left(1 - \frac{\sigma_{min}}{\sigma_b}\right)}{w_0} \quad (5.2)$$

where w_0 is the width of the welded component (in the following assumed constant and equal to 100 mm in all three cases). The necessary input data required to perform the calculations are summarized in Table 5.4.

Table 5.4 Summary of input data used to calculate the relative increase in the cross-sectional area $\Delta A/A$ from Equation (5.2).

	GMAW	FSW	HYB
w_0	100	100	100
σ_b	239	247	286
σ_{min}	131	165	155
y_{red}^{eq}	11.6	7	7.8

By inserting the appropriate input data from Table 5.4 into Equation (5.2), a necessary increase in cross-sectional area of 7.1 % is calculated in the HYB case. For the GMA and FS welds the corresponding values are 10.5 and 4.6 %, respectively.

5.7.4 Summary of calculated joint loading capacities

The results from all loading capacity calculations are summarized in Table 5.5.

Table 5.5 Summary of all results from the load-bearing capacity calculations.

	GMAW	FSW	HYB
Perpendicular			
$\frac{\Delta A}{A}$ (%)	75	52	88
Parallel			
$\frac{\Delta A}{A}$ (%)	10.5	4.6	7.1

As expected, the FS joint always exhibits a higher load-bearing capacity under otherwise similar conditions. However, the load-bearing capacity of the HYB joint is higher than that of the GMA weld when the load is parallel to the weld. This has to do with the fact that the total width of the reduced strength zone is smaller in the HYB case, as shown previously in Figure 5.15, which is a competitive advantage from a mechanical design point of view.

6 Conclusions

The basic conclusions that can be drawn from this investigation can be summarized as follow:

- 1) The new HYB PinPoint extruder is well suited for single pass butt welding of AA6082-T6 rolled plates. The full-penetration weld produced is free from pores and internal cavities, and displays a very nice surface finish on both sides.
- 2) Full metallic bonding is achieved between the filler material and the base metal in the groove, as demonstrated both by tensile testing and Charpy V-notch testing of the bond line. In addition, the subsequent SEM investigation of selected fracture surfaces revealed only evidence of dimple formation, which is compatible with a ductile fracture mode.
- 3) The hardness testing of the HYB joint disclosed evidence of significant HAZ softening. This softening reduces the yield and tensile strength of the joint to values well below these of the base material (i.e. 47 and 32 % reduction compared to the measured BM yield and tensile strength, respectively).
- 4) Also, the strain at fracture and the reduction in area during tensile testing are reduced because of the HAZ softening due to the resulting strain localization. The reduction is 46 and 17 %, respectively compared to the measured values for the BM.
- 5) In contrast, the HAZ softening has apparently a positive effect on the Charpy V-notch impact toughness, which is seen to be 97 % higher than that of the base material. However, this increase in toughness after welding is mainly believed to be a reflection of a very low initial BM toughness, which becomes healed by softening
- 6) The preliminary benchmarking of the HYB process against GMAW and FSW shows that the overall mechanical performance of the joint is slightly better than that of a comparable GMA weld. However, it does not fully match the corresponding load-bearing capacity of a FS weld. This is the next challenge to embrace.

Further work

Over the past six months, optimization of the HYB process has been a major concern. Therefore, a number of actions have already been undertaken by HyBond AS to improve the mechanical performance of the joints. These include optimization of the pin and the steel housing geometry, improvement of the efficiency of the CO₂-cooling system and the use of a more massive steel backing plate with a higher cooling capacity.

When all this upgrading is finished, the plan is to start welding of the new 4 mm AA6082-T6 extruded profiles for the Johan Sverdrup oil field in the North Sea. The HYB benchmarking against GMAW and FSW will then be done on exactly the same type of welded profiles, which previously have been produced and supplied by Apply Lervik and SAPA for the sake of comparison. A significant part of the benchmarking could be done in collaboration with NTNU and NAPIC and included in the new & upcoming PhD study.

7 References

1. United Nations Association of Norway. *Dette er Parisavtalen*. 2017 [cited 2017 15. February]; Available from: <http://www.fn.no/Tema/Klima/Klimaforhandlinger/Dette-er-Paris-avtalen>.
2. R. Lumley, *Fundamentals of Aluminium Metallurgy - Production, Processing and Applications*. Elsevier Science, Burlington, 2010.
3. W. S. Miller, et al., *Recent development in aluminium alloys for the automotive industry*, Materials Science and Engineering A. **280**(1), (2000) 37-49.
4. Ø. Grong, *Metallurgical modelling of welding*, 2nd Ed., The Institute of Materials, London, 1997.
5. J. R. Davis, *Aluminum and aluminum alloys*. ASM International, Materials Park, OH 1993.
6. T. A. Barnes and I. R. Pashby, *Joining techniques for aluminium spaceframes used in automobiles: Part I—solid and liquid phase welding*, Journal of Materials Processing Technology. **99**(1), (2000) 62-71.
7. S. Kou, *Welding Metallurgy*, 2nd Ed., Wiley, Hoboken, New Jersey, 2003.
8. R. Kumar, et al., *Thin sheet welding of Al 6082 alloy by AC pulse-GMA and AC wave pulse-GMA welding*, Materials & Design. **30**(2), (2009) 306-313.
9. Ø. Grong, *Recent advances in solid-state joining of aluminum*, Welding Journal. **91**(1), (2012) 26-33.
10. Ø. Grong, *Method and device for joining of metal components, particularly light metal components*. 2006, Google Patents.
11. U. R. Aakenes, Ø. Grong, and T. Austigard, *Application of the hybrid metal extrusion & bonding (HYB) method for joining of AA6082-T6 base material*, Materials Science Forum. **794**, (2014) 339-344.
12. P. L. Threadgill, et al., *Friction stir welding of aluminium alloys*, International Materials Reviews. **54**(2), (2009) 49-93.
13. N. R. Mandal, *Solid State Welding*, in *Ship Construction and Welding*. Springer: Singapore. p. 221-234, 2017.
14. A. Lilleby. *Experimental and Finite Element Studies of Cold Pressure Welding of Commercial Purity Aluminium by Divergent Extrusion*, PhD Thesis, Norwegian University of Science and Technology, Department of Materials Science and Engineering, Trondheim, Norway, August, 2009.
15. Ø. Frigaard, Ø. Grong, and O. T. Midling, *A process model for friction stir welding of age hardening aluminium alloys*, Metallurgical and Materials Transactions A. **32**(5), (2001) 1189-1200.
16. J. E. Hatch, *Aluminum: Properties and Physical Metallurgy*. ASM International, Materials Park, Ohio, 1984.
17. S. Karabay, M. Zeren, and M. Yilmaz, *Investigation extrusion ratio effect on mechanical behaviour of extruded alloy AA-6063*, Journal of Materials Processing Technology. **135**(1), (2003) 101-108.
18. G. Mathers, *The welding of aluminium and its alloys*. CRC Press, Boca Raton, 2002.

19. Y. Chen, et al., *An experimental study on the dynamic fracture of extruded AA6xxx and AA7xxx aluminium alloys*, Materials Science and Engineering: A. **523**(1), (2009) 253-262.
20. C. Thaulow and H. Valberg, *TMM4140 Plastisk deformasjon og brudd*, 2014, NTNU trykk, Trondheim (Norge).
21. S. K. Fjeldbo, et al., *Through-process sensitivity analysis on the effect of process variables on strength in extruded Al–Mg–Si alloys*, Journal of Materials Processing Technology. **212**(1), (2012) 171-180.
22. O. Reiso. *The effect of microstructure on the extrudability of some aluminium alloys*, PhD Thesis, Norwegian Institute of Technology, Hydro Aluminium, Metallurgical R&D Center, Sundalsøra, Norway, May, 1992.
23. C. Hsu, et al., *Non-equilibrium reactions in 6xxx series Al alloys*, Materials Science and Engineering A. **304–306**, (2001) 119-124.
24. N. C. W. Kuijpers, W. H. Kool, and S. van der Zwaag, *DSC study on Mg-Si phases in as cast AA6xxx*, Materials Science Forum. **396**, (2002) 675-680.
25. S. Zajac, B. Bengtsson, and C. Jönsson, *Influence of cooling after homogenisation and reheating to extrusion on extrudability and final properties of AA 6063 and AA6082 alloys*, Materials Science Forum. **396**, (2002) 399-404.
26. O. R. Myhr, et al., *Modelling of the microstructure and strength evolution in Al–Mg–Si alloys during multistage thermal processing*, Acta Materialia. **52**(17), (2004) 4997-5008.
27. G. E. Dieter, *Mechanical Metallurgy*, SI metric Ed., McGraw-Hill, London, 1988.
28. D. J. Chakrabarti and D. E. Laughlin, *Phase relations and precipitation in Al–Mg–Si alloys with Cu additions*, Progress in Materials Science. **49**(3), (2004) 389-410.
29. J. K. Solberg, *Teknologiske metaller og legeringer 2007*, NTNU trykk, Trondheim (Norge).
30. T. Khaled, *An outsider looks at friction stir welding*, Federal Aviation Administration. **25**, (2005) 27-29.
31. O. R. Myhr, Ø. Grong, and K. O. Pedersen, *A Combined Precipitation, Yield Strength, and Work Hardening Model for Al-Mg-Si Alloys*, Metallurgical and Materials Transactions A. **41**(9), (2010) 2276-2289.
32. O. R. Myhr, Ø. Grong, and S. J. Andersen, *Modelling of the age hardening behaviour of Al–Mg–Si alloys*, Acta Materialia. **49**(1), (2001) 65-75.
33. K. Blommedal. *Corrosion Development in Welded AA6082 Alloys*, MSc Thesis, Norwegian University of Science and Technology, Department of Materials Science and Engineering, Trondheim, Norway, June, 2013.
34. K. O. Pedersen, et al., *Influence of texture and grain structure on strain localisation and formability for AlMgSi alloys*, Journal of Materials Processing Technology. **200**(1–3), (2008) 77-93.
35. T. Kobayashi, *Strength and fracture of aluminum alloys*, Materials Science and Engineering: A. **286**(2), (2000) 333-341.
36. H. Guo, J. Hu, and H. L. Tsai, *Formation of weld crater in GMAW of aluminum alloys*, International Journal of Heat and Mass Transfer. **52**(23–24), (2009) 5533-5546.
37. F. M. Mazzolani, *Aluminium alloy structures*, 2nd Ed., E & FN Spon, London, 1995.

38. C. R. Breivik. *Mechanical properties of gas metal arc and friction stir AA6082-T6 Weldments*, MSc Thesis, Norwegian University of Science and Technology, Department of Materials Science and Engineering, Trondheim, Norway, June, 2013.
39. I. Bhamji, et al., *Solid state joining of metals by linear friction welding: a literature review*, *Materials Science and Technology*. **27**(1), (2011) 2-12.
40. W. M. Thomas, et al. *Friction based welding technology for aluminium*. in *Materials Science Forum*. 2002. Trans Tech Publ.
41. J. F. Lancaster, *Solid-phase welding*, in *Metallurgy of Welding*. George Allen & Unwin: London. p. 74-86, 1980.
42. R. W. Messler, *Principles of welding: processes, physics, chemistry, and metallurgy*. Wiley, Hoboken, 2008.
43. M. Iordachescu, et al., *Material flow and hardening at butt cold welding of aluminium*, *Journal of Materials Processing Technology*. **209**(9), (2009) 4255-4263.
44. G. Liu, et al., *Microstructural aspects of the friction-stir welding of 6061-T6 aluminum*, *Scripta Materialia*. **37**(3), (1997) 355-361.
45. S. W. Kallee, E.D. Nicholas, and W.M. Thomas. *Friction stir welding - invention, innovations and applications*. 2001 [cited 2017 1. July]; Available from: <http://www.twi-global.com/technical-knowledge/published-papers/friction-stir-welding-invention-innovations-and-applications-march-2001/>.
46. C. Gallais, et al., *Multiscale analysis of the strength and ductility of AA 6056 aluminum friction stir welds*, *Metallurgical and Materials Transactions A*. **38**(5), (2007) 964-981.
47. P. M. G. P. Moreira, et al., *Fatigue crack growth in friction stir welds of 6082-T6 and 6061-T6 aluminium alloys: A comparison*, *Theoretical and Applied Fracture Mechanics*. **50**(2), (2008) 81-91.
48. U. R. Aakenes. *Industrialising of the Hybrid Metal Extrusion & Bonding (HYB) Method—from Prototype towards Commercial Process*, PhD Thesis, Norwegian University of Science and Technology, Department of Materials Science and Engineering, Trondheim, Norway, November, 2013.
49. C. Etherington, *CONFORM—a new concept for the continuous extrusion forming of metals*, *Journal of Engineering for Industry*. **96**(3), (1974) 893-900.
50. O. R. Myhr and Ø. Grong, *Novel modelling approach to optimisation of welding conditions and heat treatment schedules for age hardening Al alloys*, *Science and Technology of Welding and Joining*. **14**(4), (2009) 321-332.
51. *Standard Test Methods for Vickers Hardness and Knoop Hardness of Metallic Materials*. 2016, ASTM International.
52. *Standard Test Methods for Tension Testing of Metallic Materials*. 2016, ASTM International.
53. *Standard Test Methods for Notched Bar Impact Testing of Metallic Materials*. 2016, ASTM International.
54. E. J. Pavlina and C. J. Van Tyne, *Correlation of Yield Strength and Tensile Strength with Hardness for Steels*, *Journal of Materials Engineering and Performance*. **17**(6), (2008) 888-893.

55. TWI. *What is the reason for specifying the ratio of yield strength to ultimate tensile strength for linepipe materials?* 2017; Available from: <http://www.twi-global.com/technical-knowledge/faqs/faq-what-is-the-reason-for-specifying-the-ratio-of-yield-strength-to-ultimate-tensile-strength-for-linepipe-materials/>.

Appendix

Task description

THE NORWEGIAN UNIVERSITY
OF SCIENCE AND TECHNOLOGY
DEPARTMENT OF ENGINEERING DESIGN
AND MATERIALS

**MASTER THESIS SPRING 2017
FOR
STUD.TECHN. LISE SANDNES**

Preliminary Benchmarking of the HYB (Hybrid Metal Extrusion & Bonding) Process for Butt Welding of AA6082-T6 Plates Against FSW and GMAW

NTNU Aluminium Product Innovation Center (NAPIC) is a newly established collaboration between three faculties at the Norwegian University of science and Technology (NTNU), Norsk Hydro, Alcoa and SAPA. Department of Mechanical and Industrial Engineering (MTP), is the host of NAPIC.

Its overall aim is to explore new product opportunities in aluminum by employing a research-driven innovation approach. This project is linked to an ongoing search for an industrialization solution for solid state joining technology developed by Hybond AS, Hybrid Metal Extrusion & Bonding (HYB). This project will focus specifically on mechanical properties of the HYB joint.

HYB is a new, patented joining technology for solid state joining of aluminum, allowing joining of aluminum components with improved strength, less cracking and corrosion problems. The technology was initially developed by professor Øystein Grong at NTNU, and is now being industrialized through Hybond AS, a joint venture between NTNU TTO, Langset AS, Statoil and Cardio Partners. The ongoing industrialization activities are based on joining of aluminium profiles and sheet components.

The main objective of this thesis is to determine the mechanical properties of AA6082-T6 Hybrid Metal Extrusion & Bonding (HYB) joints. The work will form the basis for one scientific publication regarding solid state joining of aluminium, as well as further research.

The project will be performed in cooperation with Hybond AS, and should include, but is not limited to, the following tasks:

1. Literature review:
 - Mechanical properties of Al-Mg-Si alloys.
 - Description of the FSW and HYB processes for Al-Mg-Si alloys.
 - Load-bearing capacity of welded components.

2. Experimental work:
 - Material testing of the HYB joint and the base metal (tensile testing, hardness measurements, Charpy V-notch, microstructure, SEM).
 - Analysis and presentation of test results.

3. Verification and benchmarking:
 - Comparison of test results with already existing results for FSW and GMAW.
 - Evaluation of performance.

4. Conclusion and identifying new research challenges for future work/directions

Base material certificate

AA6082 base metal (BM) certificate:

Chemische Zusammensetzung [%] Gewichtsteile / Chemical composition [%] weight proportion (OES)											
Guss Nr. / cast no.	material	Si	Fe	Cu	Mn	Mg	Cr	Zn	Ti	Sonst Einzel	Sonst Summe
01/0069540/5	EN AW 6082										
	spec. min.	0,7	-	-	0,40	0,6	-	-	-	-	-
	spec. max.	1,3	0,50	0,10	1,0	1,2	0,25	0,20	0,10	0,05	0,15
	actual	0,9	0,45	0,06	0,42	0,8	0,02	0,05	0,02	0,02	0,03

Zugprüfung LT / tensile test LT									
BNr/Los	Zustand	Richtung	Tests		Rm	Rp0.2	A50		
Lot/No.	temper	direction			[MPa]	[MPa]	[%]		
				spec.min.	310	260	10		
				spec.max.	-	-	-		
38911/01	T6	LT	2	from	329	273	18		
38911/01	T6	LT		to	335	277	18		

Sonstige Prüfungen / other tests
Maßkontrolle: OK. / Dimensional Check: OK.
Oberfläche: OK. / Surface inspection: OK.

Figure A 1 Material certificate for the base material AA6082-T6 used in HYB joining trials. (Personal communication, Ø. Grong, 2017).

Filler material certificate

AA6082 filler metal (FM):

Chemical composition

Si	Mg	Cu	Mn	Fe	Cr	Zr	Ti	B	Others	Al
1.11	0.61	0.002	0.51	0.20	0.14	0.13	0.043	0.006	0.029	balance

Casting method: DC casting

Homogenizing conditions:

Heating rate: ~200°C/h

Holding time at 540°C: 2h 15min

Cooling rate: ~300°C/h

Figure A 2 Certificate for the filler material used in the HYB joining of trials. (Personal communication, Ø. Grong, 2017).

Hardness measurements of the HYB joint

Table A 1 Location of hardness measurements for the different test series.

	Mid-section horizontal	Mid-section vertical	Displaced
Series 1	x	x	
Series 2	x	x	x
Series 3	x	x	

Table A 2 Individual hardness measurements carried out to establish the hardness of the unaffected base material. These were done randomly on a prepared sample.

Base material hardness	
Indentation number	HV
1	111
2	108.8
3	108.6
4	110.7
5	115.9
6	113.8
7	110
8	112.8
9	110.1
10	112.1
Mean value	111.4

Table A 3 Summary of individual hardness measurements from all series – measured along the horizontal mid-section of the HYB joint. Note that the table extends over two pages.

Hardness measurements along horizontal center-line							
Advancing side				Retreating side			
Distance	Hardness (HV)			Distance	Hardness (HV)		
mm	Series1	Series2	Series3	mm	Series1	Series2	Series3
0	70	68.8	68.5	0	70	68.9	68.5
0.45	72.7	71.6	70.8	-0.45	67.6	67.2	69.5
0.9	69.6	72.1	72.1	-0.9	70.2	69.4	70.6
1.35	71.3	71.6	72.5	-1.35	70	68.7	70
1.8	70.5	72	72	-1.8	69.9	68.4	70.4
2.25	66	67.8	66.6	-2.25	68.6	67	69.7
2.7	66.1	69.1	66.2	-2.7	68.7	68.5	68.67
3.15	64.9	67.9	65	-3.15	69	68.5	70.4
3.6	67.7	69.5	67.8	-3.6	70.3	69	69.2
4.05	67.4	70.7	68.2	-4.05	70.8	69.6	68.9
4.5	67.9	70.2	69.1	-4.5	70.1	68.3	71
4.95	66.8	70.2	68.9	-4.95	68.6	70	71.3
5.4	69.5	73.4	69.2	-5.4	69.6	69.8	67.8
5.85	70.9	73	70.9	-5.85	70.5	71.6	72
6.3	73	76.5	74.5	-6.3	75.9	72.9	73.4
6.75	72.5	77.4	78.4	-6.75	77.2	73.8	75.8
7.2	77.1	79.6	78	-7.2	79.8	78.3	78
7.65	82.4	81.8	81.3	-7.65	80.4	79.7	83.6
8.1	84.2	85.8	83.1	-8.1	85.8	81.7	84
8.55	86.5	90.3	89.1	-8.55	89.5	86.8	90.6
9	96.6	90.9	97.4	-9	95.3	96.2	93.6
9.45	100.7	98	100.5	-9.45	100.8	98.5	100
9.9	101.6	98.5	103.3	-9.9	103.5	100	102.6

10.35	93.5	108.5	103.8	-10.35	103.3	100.4	100.3
10.8	106.9	104	104.1	-10.8	105	102	105.7
11.25	108.9	104.8	105.9	-11.25	107.4	106.1	105.9
11.7	107.9	108.9	110	-11.7	107.9	109.3	109.4
12.15	111	107.4	109.3	-12.15	108.5	109.6	108.6
12.6	111.8	111.2	111.3	-12.6	112.1	112.4	112.8
13.05	117.6	110.2	116.5	-13.05	113.5	115.4	112.1
13.5	115.3	112.6	109.6	-13.5	114.8		111.8
13.95	112.4	112.1	113.1	-13.95	111.8		114.4
14.4	112.8	112.9	113.5	-14.4	116.1		116.2
14.85	112.7	112.9	112.7	-14.85	110.7		118
15.3	112.4		114.3	-15.3	114.2		118
15.75	110.7		111.9	-15.75	117		113.9
16.2	115.2		114.5	-16.2	114.4		116.6
16.65	113.1		111.9	-16.65	117.4		109.4

Table A 4 Summary of individual hardness measurements from all series – measured along the vertical mid-section of the HYB joint.

Hardness measurements along vertical center-line							
Distance	Hardness (HV)			Distance	Hardness (HV)		
mm	Series 1	Series 2	Series 3	mm	Series 1	Series 2	Series 3
0	70.6	68.8	68.5	0	68.8	70.6	68.5
0.45	74.6	74.6	75.1	-0.45	69.5	69.3	71.1
0.9	714.2	69.8	73.1	-0.9	65.6	65.7	66.1
1.35	85.2	84.24	84	-1.35	60.1	59.8	59.9
1.8	93.5	92.5	88.7	-1.8	64.1	61.9	60.8
2.25	93.5	92.9	94.5	-2.25	58	58.9	58.9
2.7		94	94.8	-2.7	73.1	68.7	70.3

Table A 5 Summary of individual hardness measurements for test Series 2 – displaced relative to the horizontal mid-section of the HYB joint. Note that the table extends over two pages.

Displaced horizontal hardness measurements					
Advancing side			Retreating side		
Distance	Hardness (HV)		Distance	Hardness (HV)	
mm	Above centre-line	Below center-line	mm	Above centre-line	Below center-line
0	65.8	69.8	0	65.8	69.8
0.45	66.8	71.7	-0.45	65	71.3
0.9	67.2	70.1	-0.9	65.3	74.8
1.35	66.6	74.6	-1.35	64.8	74.5
1.8	65.4	73.3	-1.8	66.3	74.4
2.25	65.9	73.5	-2.25	68.5	75.5
2.7	68.5	68.4	-2.7	68.5	73.9
3.15	70.4	68.3	-3.15	71.4	75
3.6	74.4	68.3	-3.6	71.4	72.6
4.05	70.2	67.3	-4.05	70.7	71.8
4.5	74.9	65.9	-4.5	72.6	72.2
4.95	75.2	70.8	-4.95	73.9	70.9
5.4	78.2	71.1	-5.4	77.8	71.3
5.85	80.7	74.5	-5.85	79.3	70.8
6.3	79.9	73.6	-6.3	80.7	71.8
6.75	80.9	76.4	-6.75	80.8	74
7.2	84.5	79.2	-7.2	85.7	78.8
7.65	87	83.7	-7.65	89.6	83.4
8.1	93.2	86.9	-8.1	94.6	87.9
8.55	94.5	95.9	-8.55	93.8	90.7
9	102	101.3	-9	98.2	96.3
9.45	105.2	105.2	-9.45	103.3	100.6
9.9	102.7	105.6	-9.9	107.4	103.5

10.35	109.4	105.1	-10.35	106.9	110.2
10.8	110.7	115.1	-10.8	110.1	104.1
11.25	111.8	113.6	-11.25	110.5	109.8
11.7	114.5	110.1	-11.7	112.6	112.2
12.15	113.2	111.7	-12.15	116.7	112.8
12.6	113.9	116.4	-12.6	116.6	114.8
13.05	116.1		-13.05		
13.5	117.1		-13.5		

Table A 6 Summary of individual hardness measurements from test Series 2 – displaced relative to the vertical mid-section of the HYB joint.

Displaced vertical hardness measurements					
Distance	Hardness (HV)		Distance	Hardness	
mm	Left	Right	mm	Left	Right
0	69.4	71.9	0	69.4	71.9
0.45	72.1	75.7	-0.45	69	72.2
0.9	74.8	69.9	-0.9	65.1	66.8
1.35	86.3	80.4	-1.35	60.5	61
1.8	93.5	90.5	-1.8	61.1	67.2
2.25	91.6	92.5	-2.25	59.1	60.7
2.7	94.8	94.3	-2.7	62.3	79.8

Stress-strain curves for the base metal and the HYB joint along with macro-images of tensile specimens

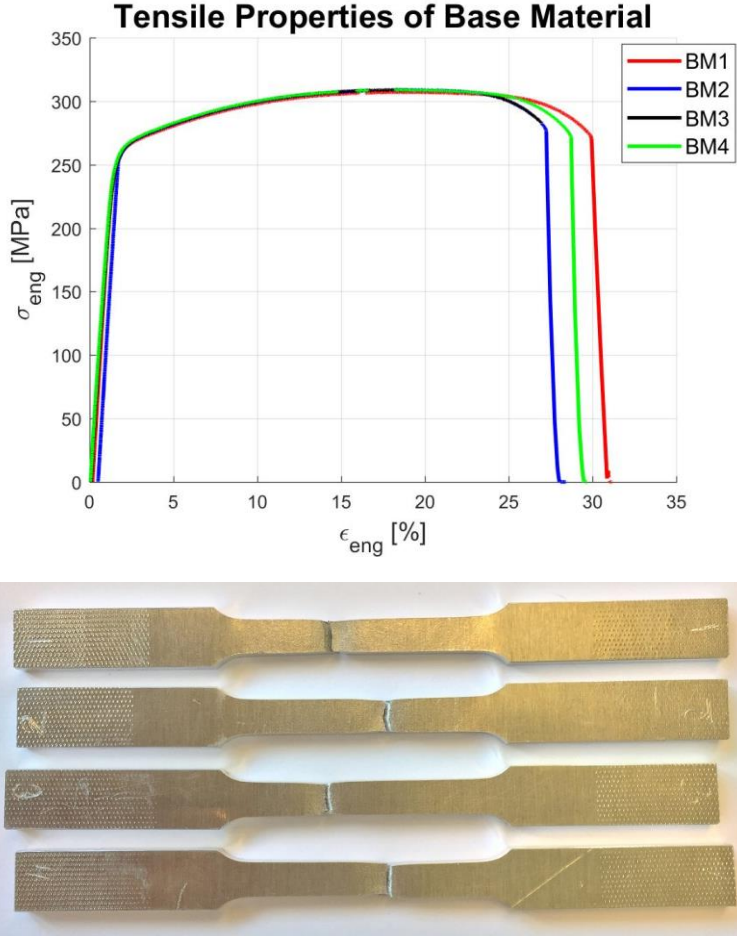


Figure A 3 Measured stress-strain curves for the base material. Included are also macro-images of the tensile specimens subsequent to testing. (Specimen number 1 is presented in the report).

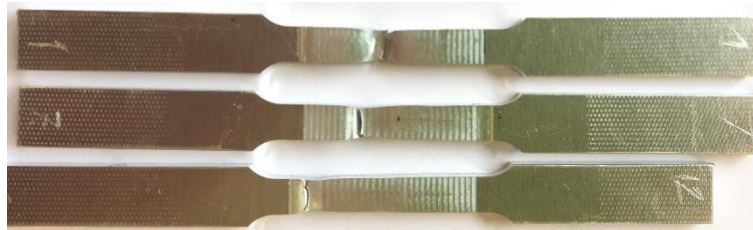
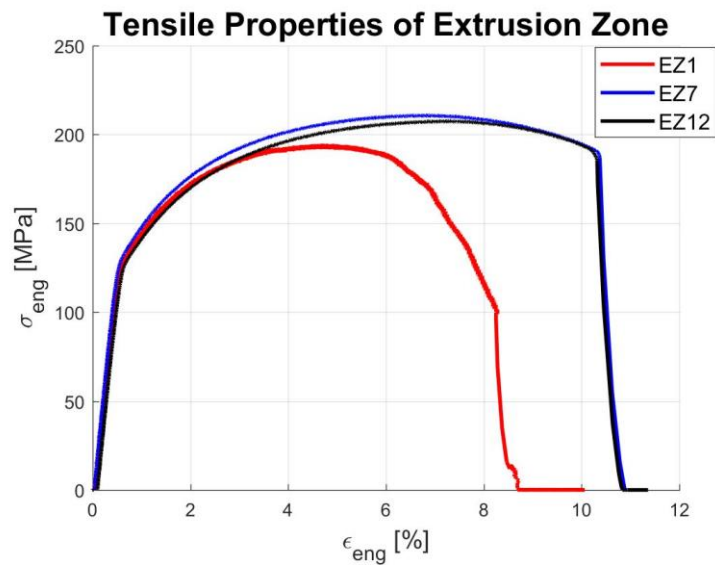


Figure A 4 Measured stress-strain curves for extrusion zone. Included are also macro-image of the tensile specimens subsequent to testing. (Specimen 7 is presented in the report).

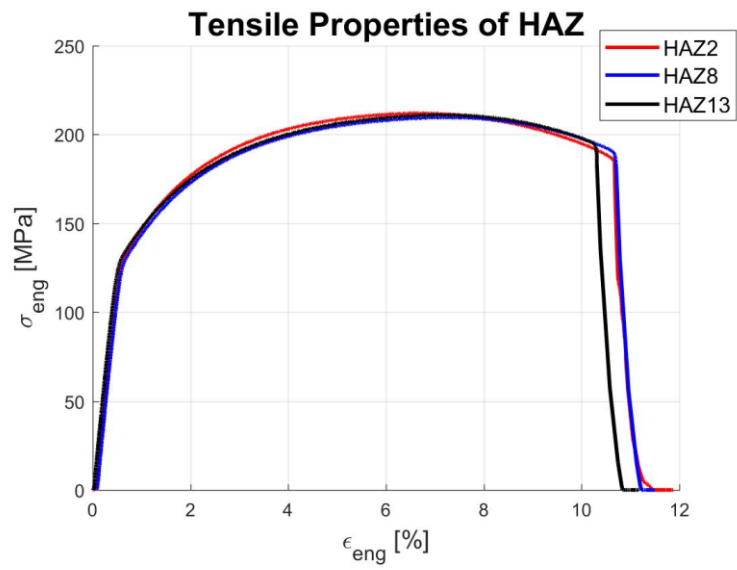


Figure A 5 Measured stress-strain curves for the HAZ. Included are also macro-images of the tensile specimens subsequent to testing. (Specimen 8 is presented in the report).

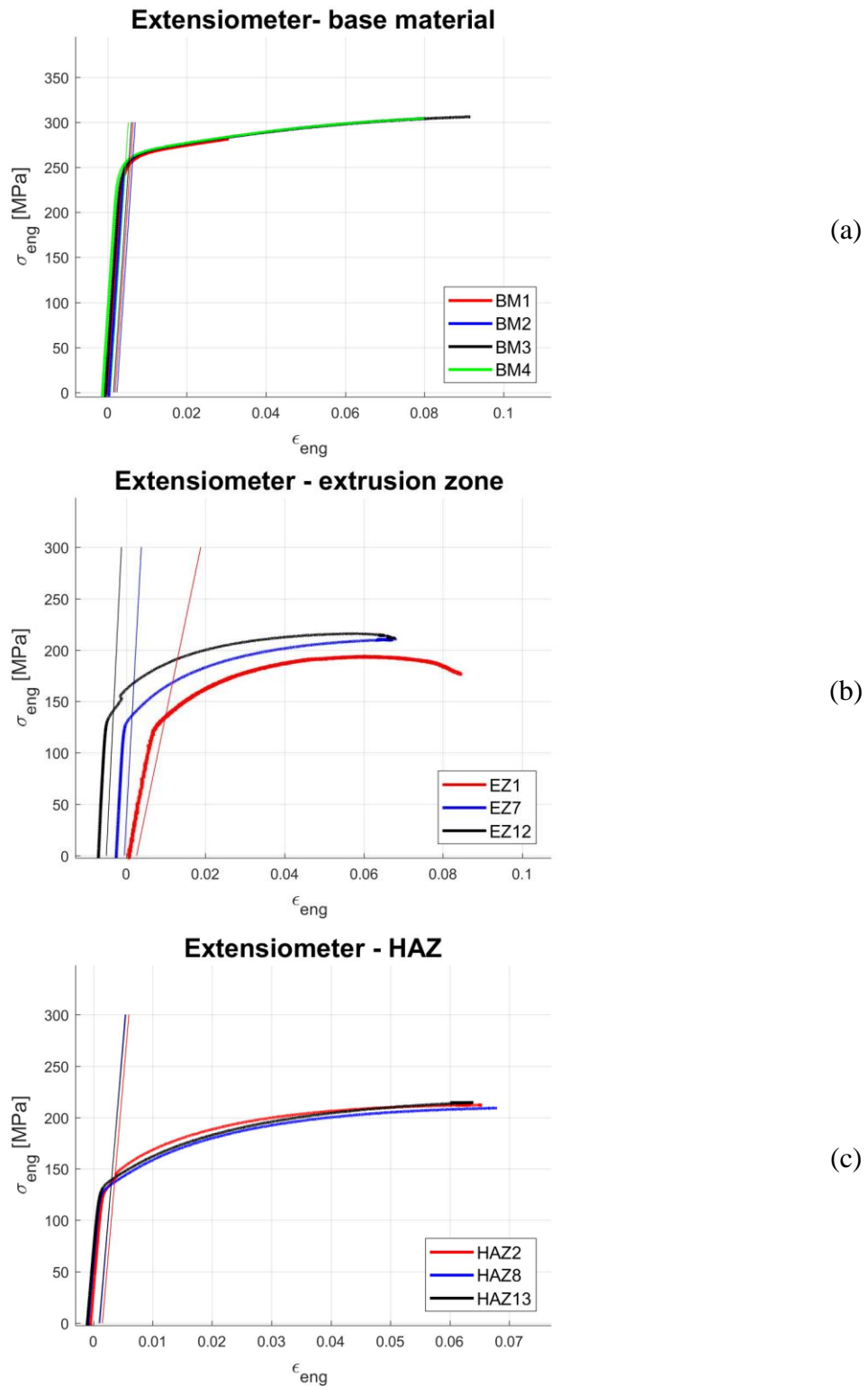


Figure A 6 Stress-strain curves generated by the extensometer. These curves are used to calculate the module of elasticity and offset yield stress for all tensile specimens. (a) Base material. (b) Extrusion zone and (c) HAZ. (Specimens BM1, EZ7 and HAZ8 are presented in the report).

Table A 7 Calculated values for the module of elasticity for all tensile specimens tested. Note that the calculated module of elasticity for the extrusion zone specimen number 1 is treated as a runout (marked red) and is therefore omitted in the calculations of the average module of elasticity.

Module of elasticity		
Location	Specimen number	E (GPa)
Base material	1	64.87
	2	64.33
	3	66.07
	4	66.83
Extrusion zone	1	18.51
	7	70.25
	12	75.72
HAZ	2	67.29
	8	66.93
	13	64.72
Mean value		67.51

Table A 8 Measured tensile properties of the BM and the HYB joint. Note that calculated module of elasticity for the extrusion zone specimen number 1 is treated as a runout (marked red), and is therefore omitted in the calculation of the average offset yield stress and tensile strength.

Location	Tensile properties (MPa)		
	Specimen number	Stress at offset yield	Tensile strength
Base material	1	251.3	303.6
	2	257.9	305.4
	3	255.7	306.3
	4	255.3	309.2
Mean values		255.1	306.1
Extrusion zone	1	133.5	194.12
	7	136.3	210.92
	12	135.8	207.84
Mean values		136.1	209.4
HAZ	2	140.2	212.3
	8	135	210
	13	135.4	211.5
Mean values		136.9	211.3

Table A 9 Calculated values for the strain at fracture for the BM and the HYB joint and percentage reduction in fracture strain (%EL). The original gauge length is 32 mm. Note that calculated module of elasticity for the extrusion zone specimen number 1 is treated as a runout (marked red), and is therefore omitted in the calculation of the average strain at fracture.

Location	Strain at fracture		
	Specimen number	Elongation at fracture (mm)	%EL
Base Material	1	7.49	23.39
	2	6.81	21.28
	3	6.73	21.04
	4	7.18	22.44
Mean values		7.05	22.04
Extrusion zone	1	2.65	8.28
	7	3.32	10.37
	12	3.30	10.32
Mean values		3.31	10.35
HAZ	2	3.41	10.66
	8	3.42	10.68
	13	3.29	10.29
Mean values		3.37	10.54

Table A 10 Calculated values for the reduction in area for the BM and the HYB joint. Included are also data for the cross-sectional area before and after testing (%RA – percent reduction in area).

Location	Cross-sectional area (mm ²)			
	Specimen number	Before A _i	After A _f	%RA
Base material	1	24.3	16.12	33.66
	2	24.3	16.43	32.39
	3	24.3	16.02	34.07
	4	24	17.06	28.92
Mean values		24.23	16.41	32.26
Extrusion zone	1	22.8	16.49	27.68
	7	22.8	17.49	23.29
	12	23.1	16.38	29.09
Mean values		22.9	16.79	26.69
HAZ	2	22.2	13.64	38.56
	8	22.8	16.64	27.02
	13	22.8	17.60	22.81
Mean values		22.6	15.96	29.46

Additional fracture images for the HYB tensile specimens

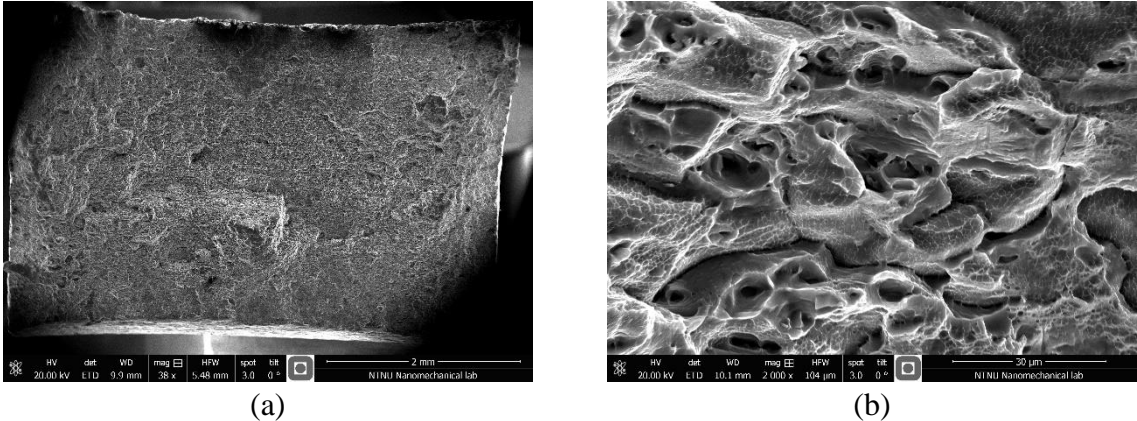


Figure A 7 Additional SEM fracture images of the base material. (a) Overview at low magnification. and (b) Close-up in the center at high magnification.

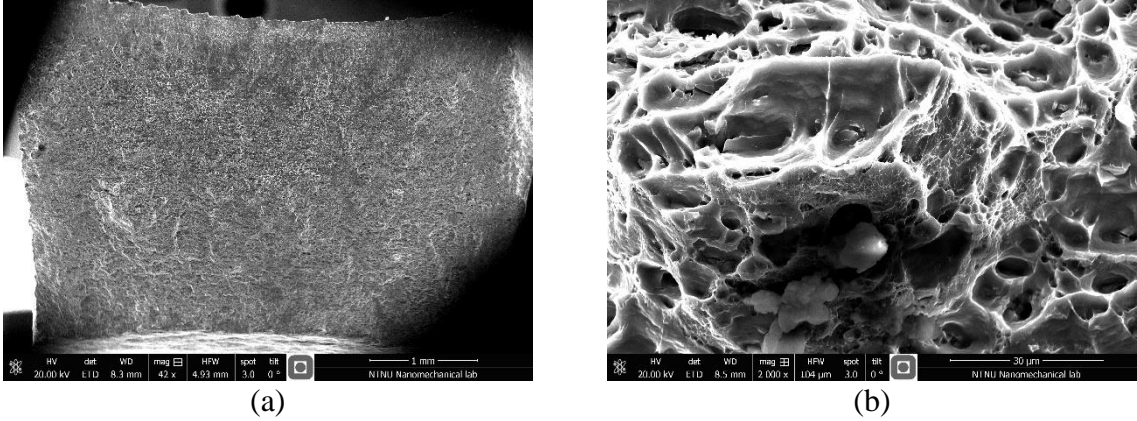


Figure A 8 Additional SEM fracture images of the extrusion zone. (a) Overview at low magnification and (b) Close-up in the center at high magnification.

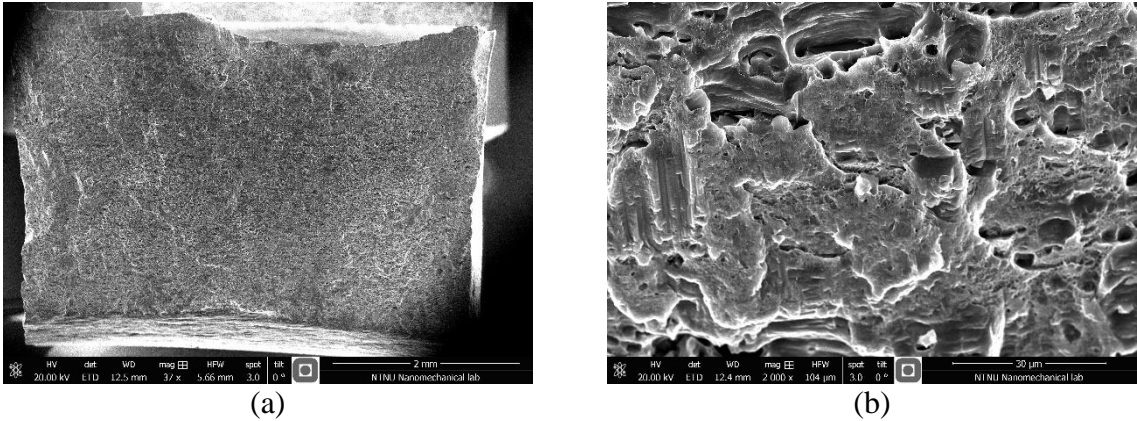
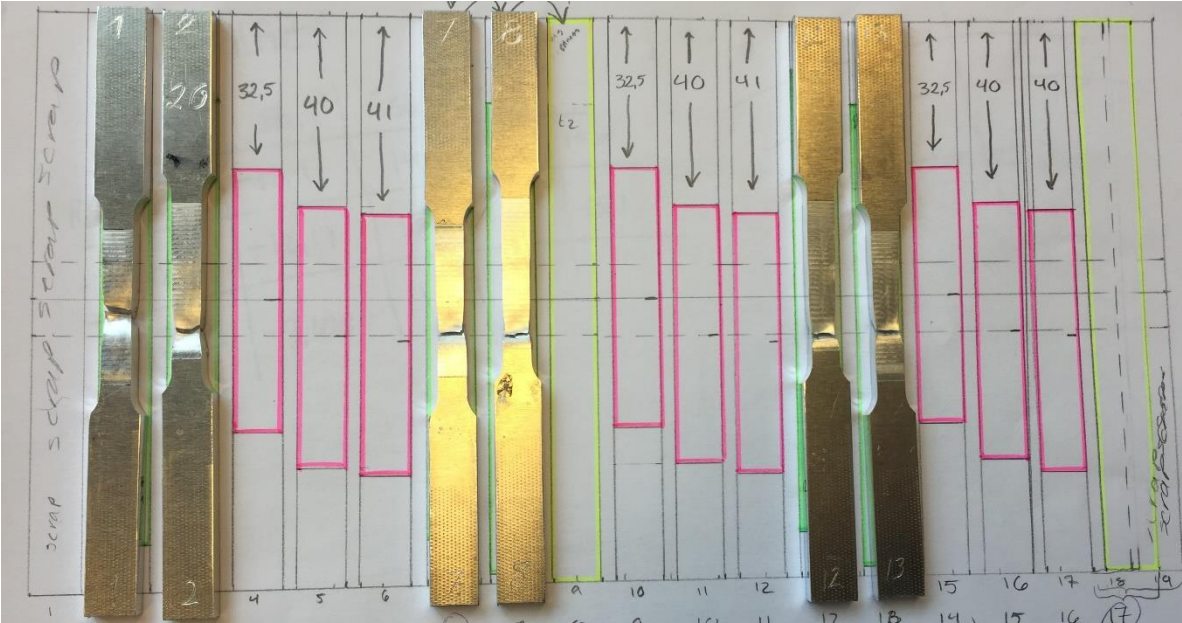


Figure A 9 Additional SEM fracture images of the HAZ. (a) Overview at low magnification and (b) close-up in the center at high magnification.

Additional images of the fracture location in broken tensile specimens



(a)



(b)

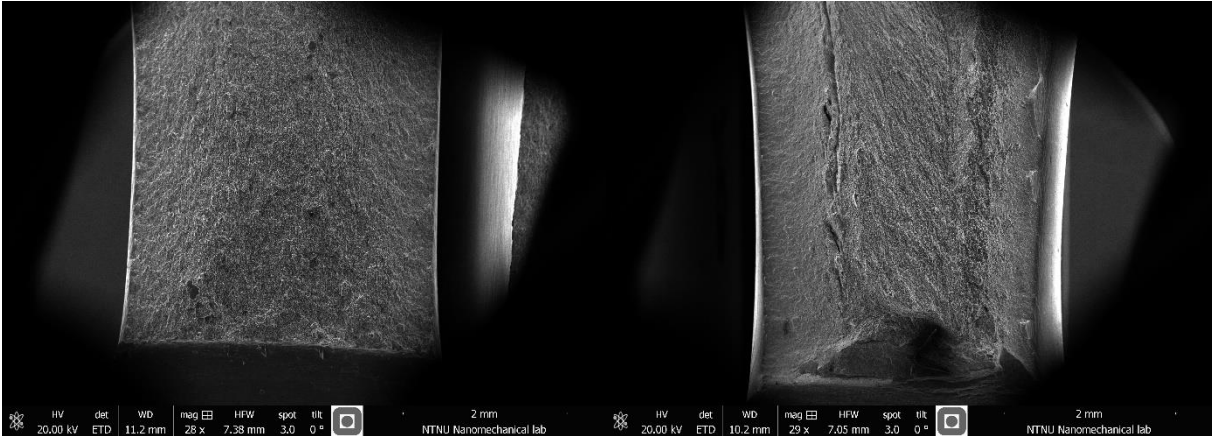
Figure A 10 Additional images of the fracture location in broken tensile specimens. (a) Overview of fracture location related to the original drawing of the sample location. The advancing side of the joint is the lower part. (b) Macro-image of specimen number 1 showing that fracture occurs close to the extrusion zone. The advancing side is to the right in the photograph.

Charpy V-notch testing

Table A 11 Summary of all Charpy V-notch results from the BM and the HYB joint.

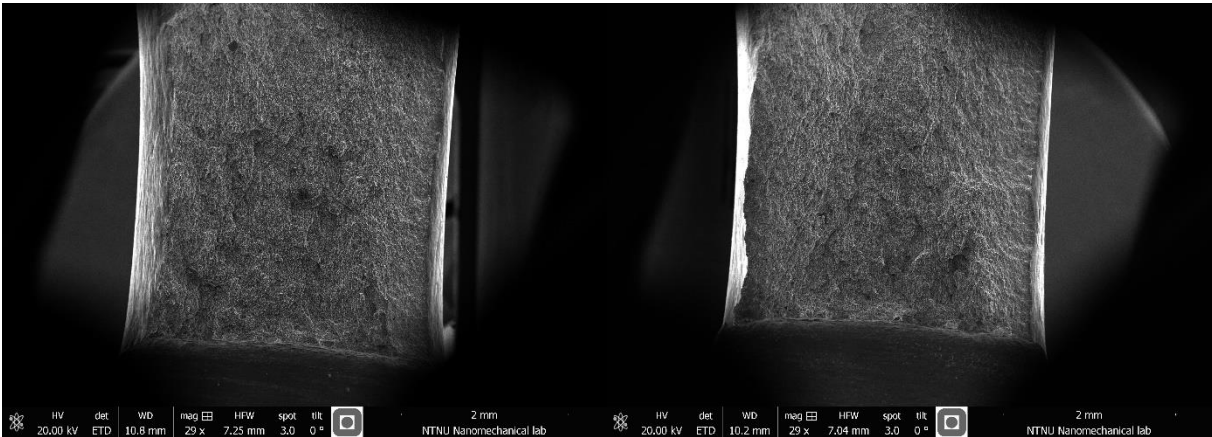
Location of notch	Specimen number	Energy absorption (J)
Base material	5	3.35
	6	3.37
	7	3.81
Mean value		3.51
Extrusion zone	3	8.06
	9	10.49
	14	11.1
Mean value		9.88
Bond line	4	6.88
	10	7.13
	15	7.04
Mean value		7.02
HAZ	5	6.88
	11	6.97
	16	6.96
Mean value		6.94

Additional fractographs of Charpy V-notch fracture surface



(a) Base material

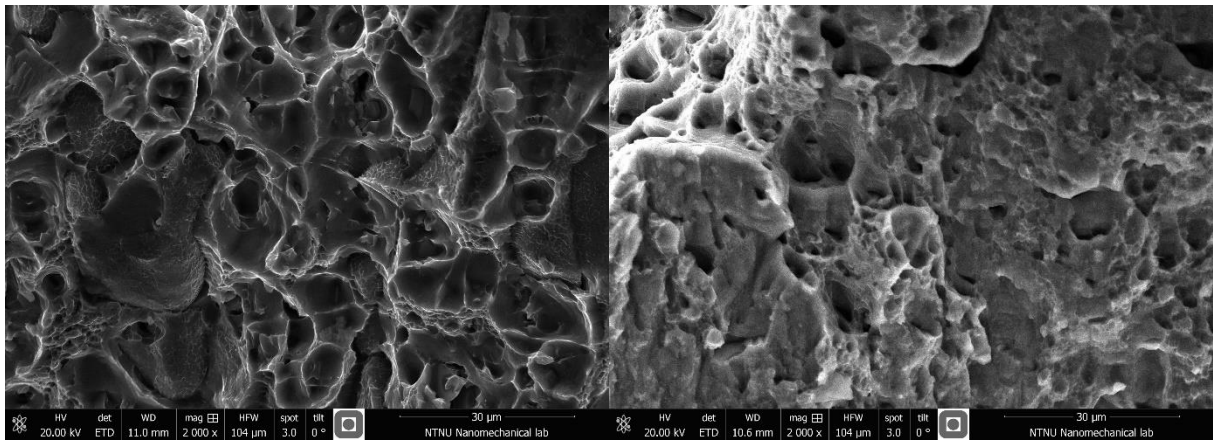
(b) Extrusion zone



(d) Bond line

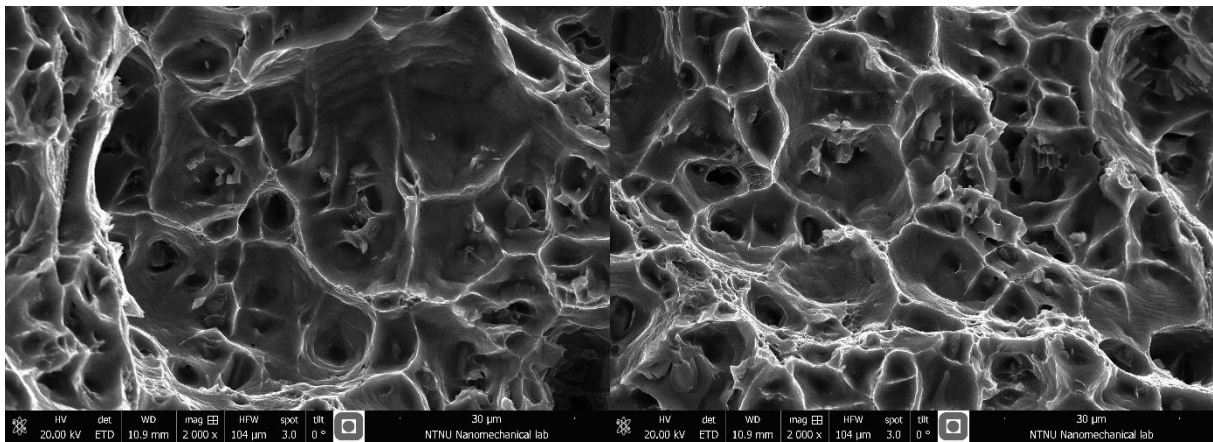
(d) HAZ

Figure A 11 Additional SEM images of the fracture surfaces at low magnification for selected Charpy V-notch specimens. (The scale bar in the lower right corner is 2 mm).



(a) Base material

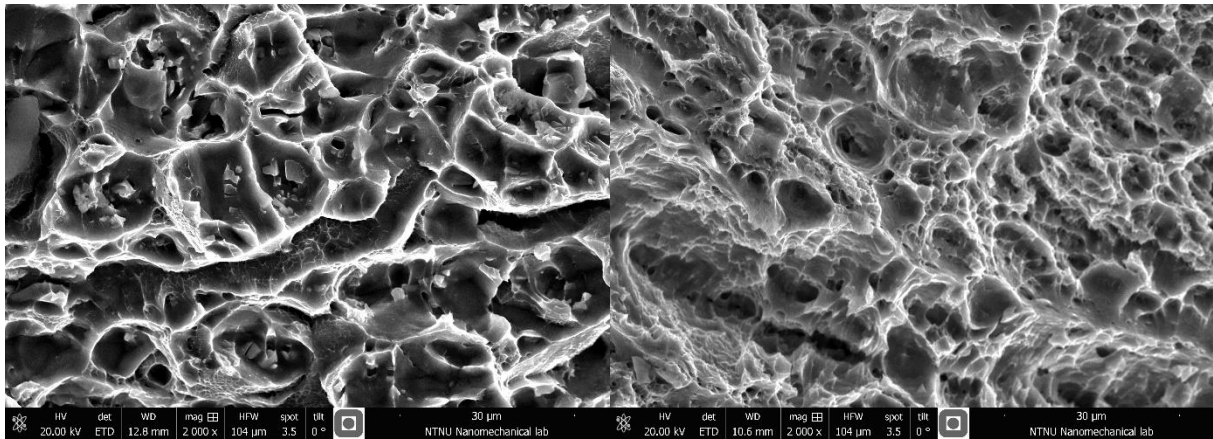
(b) Extrusion zone



(c) Bond line

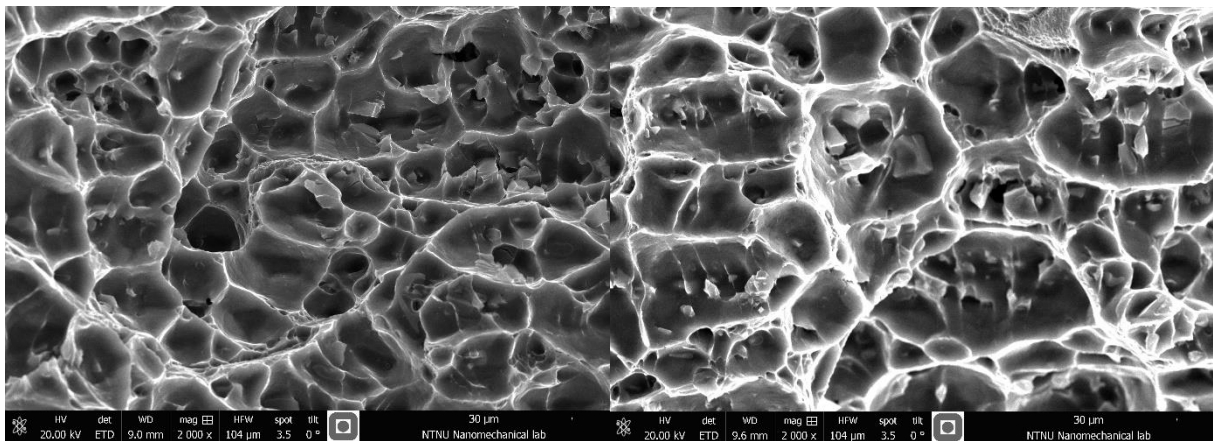
(d) HAZ

Figure A 12 Additional SEM images of the fracture surface at high magnification close to the V-notch for selected Charpy V-notch specimens. (The scale bar in the lower right corner is 30 μm).



(a) Base material

(b) Extrusion zone



(c) Bond line

(d) HAZ

Figure A 13 Additional SEM images of the fracture surface at high magnification in the center of selected Charpy V-notch specimens. (The scale bar in the lower right corner is 30 μm).

Table A 12 Cross-sectional area of the Charpy V-notch specimens, as measured from the edge of the notch.

Location	Cross-sectional area (mm²)	
	Specimen number	A₀
Base material	5	32.2
	6	32.6
	7	32.6
Extrusion zone	3	32.6
	9	32.6
	14	32.6
Bond line	4	32.2
	10	32.4
	15	32.81
HAZ	5	32.6
	11	32.6
	16	32.8

Yield stress calculations

Table A 13 Yield strength values, as calculated from the transverse hardness profile of the HYB joint. Note that the table extends over two pages.

Yield strength form hardness profile			
Advancing side		Retreating side	
Distance	Yield strength	Distance	Yield strength
mm	MPa	mm	MPa
0	160	0	160
0.45	167	-0.45	156.2
0.9	165.7	-0.9	162.1
1.35	167.3	-1.35	160.6
1.8	166.4	-1.8	160.6
2.25	152.3	-2.25	157.2
2.7	149.7	-2.7	157.8
3.15	156.9	-3.15	159.8
3.6	158.2	-3.6	160.4
4.05	156.9	-4.05	161.2
4.5	159.1	-4.5	161.3
4.95	157.7	-4.95	161.8
5.4	164	-5.4	159.1
5.85	166.7	-5.85	166
6.3	175.9	-6.3	174.1
6.75	180.2	-6.75	178.7
7.2	186.6	-7.2	188
7.65	197.4	-7.65	195.6
8.1	205	-8.1	203.4
8.55	217.8	-8.55	218.8
9	236.8	-9	237
9.45	251.1	-9.45	249.2
9.9	255.3	-9.9	258
10.35	257.7	-10.35	255.9
10.8	266.9	-10.8	264.6

11.25	271.5	-11.25	271.3
11.7	278.7	-11.7	278.5
12.15	279.6	-12.15	278.6
12.6	286.2	-12.6	289.2
13.05	296.2	-13.05	292.9
13.5	289.5	-13.5	291.7
13.95	289.5	-13.95	291.1
14.4	291.1	-14.4	300.3
14.85	290.2	-14.85	294.9
15.3	291.9	-15.3	300.1
15.75	285.7	-15.75	298.2
16.2	296.4	-16.2	298.3
16.65	289.3	-16.65	292
